THEORETICAL STUDY OF TOPOLOGICAL SINGULARITIES IN NONRECIPROCAL NON-HERMITIAN METASURFACE

JIANG YIMIN

MPhil

The Hong Kong Polytechnic University

2025

The Hong Kong Polytechnic University

Department of Applied Physics

Theoretical Study of Topological Singularities in Nonreciprocal Non-Hermitian Metasurface

JIANG Yimin

A thesis submitted in partial fulfilment of the requirements for the degree of Master of Philosophy

April 2025

CERTIFICATE OF ORIGINALITY

I hereby declare that this thesis is my own work and that, to the best of my knowledge and belief, it reproduces no material previously published or written, nor material that has been accepted for the award of any other degree or diploma, except where due acknowledgement has been made in the text.

_____ (Signed)

_____JIANG Yimin_____ (Name of student)

Abstract

Since the first experimental realization of photonic topological insulator using nonreciprocal gyromagnets in 2008, optical control systems have emerged as a widely-used platform for topological physics in both theoretical and experimental studies, where gyromagnets are implemented as the origin of nonreciprocity supporting photonic chiral edge states. As the topological classification of Hermitian systems becomes mature, the research focus shifts to non-Hermitian topology, where the system has more degrees of freedom, thus the classification becomes more intricate. Due to the ease of implementing non-Hermiticity via optical gain and loss, optical system has become a key platform for non-Hermitian topology in contrast to quantum system.

Therefore, this project aims at the analytical study of topological properties of a 1D-periodic non-Hermitian nonreciprocal electromagnetic metasurface, which is composed of cylinder arrays of gyromagnetic yttrium iron garnet (YIG) and lossy dielectric materials. Using Mie theory and multiple scattering theory, the rigorous solution of the scattered field under plane wave incidence is obtained, enabling a physical interpretation of the intrinsic mechanism.

The nontrivial topology is identified in the nonreciprocal transmission, characterized by robust polarization singularities in the parameter spaces. The singularities arise from the coupling between the YIG array and the dielectric array; and their robustness is shown to be protected by the strong nonreciprocal magnetic response of the YIG array. The results demonstrate the interplay of nonreciprocity and non-Hermiticity in a topological optical system – as the coupling effect on lossy dielectric array is nonreciprocal, the excitations on the absorption loss are different under opposite incident directions, resulting in the nonreciprocal transmission. The mechanism of robustness induced by nonreciprocal magnets can be generalized to other systems and may offer insights into the implementation of non-Hermitian topological classifications. The results may also inspire the design of optical isolators and polarization modulators, through zero transmission at singularities and associated vortex polarization fields.

Publication arising from the thesis:

[1] Yimin Jiang *et al* 2023 *J. Phys.: Conf. Ser.* 2670 012012. DOI: 10.1088/1742-6596/2670/1/012012.

Acknowledgement

Firstly, I sincerely appreciate my supervisor Prof. YU Siu Fung and Dr. FUNG Kin-Hung for their both academic guidance, supports, and caring for my research progress and emotion. Next, I would thank my groupmates and other friends I met at the university for their supports in all aspects, especially Mr. Wong Wai Chung and Dr. YAU Wang Tat for their help which significantly contributes to my study. I would also express my appreciation to the lecturers Dr. Zhu Ye and Dr. Yang Ming, as I learned a lot from their courses. Finally, thank my family members for their unconditional supports and caring as always.

Table of contents

Basic formulas for Bessel functions

- Bessel functions are solutions to Bessel differential equation:

$$x^2\frac{d^2y(x)}{dx^2}+x\frac{dy(x)}{dx}+(x^2-n^2)\cdot y(x)=0.$$

There are four eigen-solutions: Bessel functions of first kind $J_n(x)=\sum_{k=0}^{\infty}(-1)^k\cdot\frac{1}{k!\Gamma(n+k+1)}\left(\frac{x}{2}\right)^{2k+n}$; Bessel function second kind, also called Neumann function $Y_n(x)=\frac{\cos(n\pi)J_n(x)-J_{-n}(x)}{\sin(n\pi)}$; Bessel functions of third kind, also called Hankel function of first kind $H_n^{(1)}(x)=J_n(x)+iY_n(x)$ and second kind $H_n^{(2)}(x)=J_n(x)-iY_n(x)$. The complete solution is a superposition of any two out of four solutions.

- The generating function of J_n of integer order n: $e^{\frac{1}{2}x\left(\gamma-\frac{1}{\gamma}\right)}=\sum_{n=-\infty}^{\infty}J_n(x)\gamma^n$.
- The transform between positive and negative integer orders n of $B_n(x)$, where $B_n(x)$ stands for $J_n(x)$, $Y_n(x)$, $H_n^{(1)}(x)$, and $H_n^{(2)}(x)$: $B_{-n}(x)=(-1)^nB_n(x)$.
- The differentiation of Bessel functions $B_n(x)$ with respect to x, where $B_n(x)$ stands for $J_n(x)$, $Y_n(x)$, $H_n^{(1)}(x)$, and $H_n^{(2)}(x)$:

$$B_n'(x)=\frac{\partial B_n(x)}{\partial x}=\frac{1}{2}[B_{n-1}(x)-B_{n+1}(x)].$$

- The Graf's and Gegenbauer's addition theorem of Bessel functions $B_n(x)$:

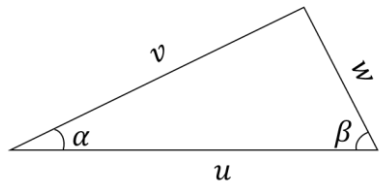

Addition theorem: when $|ve^{\pm i\alpha}|<|u|$, any Bessel function $B_n(x)$ satisfy:

$$\begin{cases}B_n(w)\cos(n\beta)=\sum_{m=-\infty}^{\infty}B_{n+m}(u)J_m(v)\cos(m\alpha)\\ B_n(w)\sin(n\beta)=\sum_{m=-\infty}^{\infty}B_{n+m}(u)J_m(v)\sin(m\alpha)\end{cases},$$

where J is the Bessel function of first kind; n and m are orders of Bessel functions; u, v, w, α, and β are geometric parameters as illustrated in the figure at left. The requirement $|ve^{\pm i\alpha}|<|u|$ can be waived when $B_n(x)$ stands for $J_n(x)$.

Combing addition theorem with Euler's formula $e^{i\theta}=\cos\theta+i\cdot\sin\theta$, it can be deduced that: $B_n(w)e^{in\beta}=\sum_{m=-\infty}^{\infty}B_{n+m}(u)J_m(v)e^{im\alpha}$.

Chapter 1. Introduction

1.1 Light control by optical systems

People have a longstanding interest in the control of light. On the one hand, the control of light propagation can be the control of energy flux or so-called light intensity. From an early stage, convex opaque objects were found capable to focalize sunlight. On the other hand, light is also the medium carrying information through its frequency, which is represented by color in visible frequency range. Reflective mirrors are used in periscopes to change the light path; convex/concave lenses are used to magnify images in microscopes and telescopes, or to adjust the visual focal length in shortsighted or farsighted glasses.

With the development of electromagnetic theory, the wave nature of light was discovered and the research interest transitioned from ray optics to wave optics, where more degrees of freedom of light were explored as information carrier, such as polarization and phase.

According to Maxwell's equations, the electric field and magnetic field are induced by charges and currents, leading to the light-matter interaction, and their mutual dependence enables wave propagation in vacuum. Moreover, the linearity of solutions to Maxwell's equations enables distinguishable electromagnetic signals from different channels.

The mechanism of light-matter interaction is: as atoms are constituted by charged particles such as ions and electrons, under electromagnetic wave incidence, the charged particles are forced to oscillate and emit secondary radiation. The light-matter interaction explains the origin of permittivity and permeability, thus reflection, refraction, dispersion, and scattering. According to this mechanism, light control can be more precise by the delicate design of structure and composition of optical systems.

In crystals, the periodic structure results in the periodic electron wave function, according to Bloch's theorem. Inspired by the formal equivalence between one-body electron wave function and electromagnetic waves, a design of optical controllers with periodic refractive index was proposed to mimic the periodic electric potential in crystals [1, 2]. This is called the photonic crystals, where exotic phenomena with counterparts in electron crystals are found, such as photonic band gaps [1-4].

Initially in photonic crystals, the structural sizes are comparable to the wavelength

(dominated by Bloch scattering [5]). Later, a new type of periodic optical systems called metamaterials emerged, which manipulate the light-matter interaction mainly by subwavelength scatterer units (dominated by Mie scattering [5]). Therefore, for the same target frequency range, metamaterials are miniaturized compared to photonic crystals [5]. As every wave medium consists of particles embedded in vacuum (except for vacuum itself) and is intrinsically inhomogeneous, its permittivity and permeability are spatially averaged. Following this paradigm, if the structural sizes are small enough compared to the wavelength, the permittivity and permeability of metamaterial can also be computed by effective medium theory [6, 7]. This methodology is theoretically and intrinsically beyond the traditional mechanisms of light control in bulk materials, such as refraction and dispersion.

Based on this, metamaterials can have abnormal constitutive parameters, such as negative refractive index or negative permeability in microwave range using arrays of metallic rods or metallic rings [6, 8, 9]. With the broadened range of effective constitutive parameters, it is possible to achieve invisible metamaterials, where the rays are guided around an object and its surroundings are optical “Black Holes” [10, 11]. Moreover, some metamaterials may not be strictly periodic, as unit cells may vary regularly along the array to achieve specific control objectives, such as metallic lenses [12]. For example, the directions of dielectric rods can be manipulated to modulate the phase of the wave front [13] according to the generalized Snell’s law. Metamaterials have utilized every degree of freedom of vectorial electromagnetic waves. Up to now, the nomenclature of metamaterials conceptually includes photonic crystals. There is no clear boundary to distinguish these two concepts. Since the scattered field in all structure can be computed by Mie solution, the transition between photonic crystals and periodic metamaterials can be studied [5].

Metasurfaces are planar versions of bulk metamaterials. They are composed of monolayer or several layers of units, and usually have subwavelength thicknesses, thus being more compact in size. The compact metasurfaces still perform effective subwavelength control of the polarization, phase and amplitude of light, by the delicate design of the geometry and constitution of scatterers [14, 15], where the use of gyromagnetic materials is important in all aspects such as in negative index material and robust control of nonreciprocal transmission. Therefore, metasurfaces are effective and extremely compact optical control systems. These

advantages also make metasurfaces as popular platforms for the study of topological optics [16], such as the design of topological optical isolator [17], the non-Hermitian sensitive detector, and the optical phase modulator around an exceptional point [18].

1.2 Topological optics and the use of nonreciprocal gyromagnets

Topology in condensed matters

Since the first discovery of the quantum Hall effect (QHE) in 1980s [19, 20], topology in physics has aroused significant interest for both theoretical study and application purposes. In a semiconductor heterojunction under extremely low temperature and strong magnetic field, the 2D electron gas behaves unusually that the Hall conductance of the system can only be an integer v_H times a constant $\frac{{e_c}^2}{2\pi\hbar}$, where e_c is the elementary charge and $\hbar$ is the reduced Planck's constant; and the Hall conductance is independent of the material's species and purity [20], which is significantly different from the classical Hall effect where conductance is proportional to the strength of the magnetic field.

Later in the 1980s, Thouless and his coworkers [21] named the quantized integer v_H as TKNN number and first demonstrated that the integer is a topological invariant depending on nonlocal properties of the entire system, thus is robust under local defects and small disturbances. Mathematically, a topological invariant of a function or a field embedded in a manifold stays still under any continuous deformation. The condition of this robustness is two-fold: Firstly, the manifold or space in which the field is embedded must be closed. For example, the phase space is a closed space, where 0 and 2π coincide. Secondly, the function or the field should be continuous. This continuity makes topological property of the field nonlocal. An example of topological invariant is the Euler characteristic of 3D polyhedron, which is always 2 regardless of the geometrical details.

The TKNN topological invariant of electron's band is intrinsically the Chern number of band in insulating 2D-periodic material. For a periodic 2D system, its Brillouin zone in momentum space is a closed manifold and is equivalent to a torus by connecting its opposite boundaries. The electron's wave function is embedded in the torus, and the Berry curvature and Chern number of the function can be defined, which is similar to the Gauss curvature and Euler characteristics defined for a closed surface in 3D space. The Chern number of electron's band is calculated by the integral of Berry flux of the band over the first Brillouin zone [21]. Different wave functions result in different Chern numbers of band and different topological classifications which the band belong to. For each separate band, the unique value of its integer

Chern number implies the band topology, which is trivial if the Chern number is zero and nontrivial otherwise. At the interface of two bulk materials, robust edge states crossing the band gap are formed. The number of possible edge states is equal to the difference of the sum of the Chern numbers of bands under the Fermi level between two bulk materials, according to the bulk-edge correspondence [22]. The robustness of edge states is guaranteed by the robustness of the Chern number. Therefore, the 2D materials, which are insulating in bulk but have nontrivial band topology, allow electrons to flow along edges at the interface between a nontrivial bulk insulator and a trivial environment, thus are named as topological insulators (TIs) [22]. TIs have advantages over normal insulators: Firstly, the electrons' edge flow avoids random electron scattering through the bulk, thus significantly reducing the energy loss such as heat dissipation. Secondly, the topological edge state is robust against local defects and disorders, therefore the pathway of electrons is highly controllable and applicable to network design [23]. By adding perpendicular magnetic field to the material, the reversibility is broken thus the electrons can unidirectionally transmit along the edge in topological insulator TI, which is called the chiral edge state [22].

The theory of topological physics also reveals a new identification of phase by topological excitation and a new mechanism of topological phase transition [22] beyond Landau's symmetry breaking theory, according to which the phase transition must associate with the breaking or recovering of symmetry. In quantum Hall states, the topological excitation is the robust quantized Hall conductance resulting from the strong Anderson localization for electrons; and the quantum Hall transitions are associated with abrupt changes of Hall conductance. Besides, in superfluid and superconductors, the unconventional phase transitions without symmetry breaking are successfully explained by Berezinskii-Kosterlitz-Thouless (BKT) phase transition, where the discrete change happens for an integer topological invariant associated with the topological vortex excitation which cannot be eliminated under continuous deformation in a compact phase space [21, 22]. So far, the study of topological physics in condensed matter has included not only the integer quantum Hall effect introduced above [20], but also fractional Hall effect, spin Hall effect, and anomalous Hall effect.

Topological optics

Although there is no photonic conductor or insulator due to the absence of Fermi level in photonic band, the photonic TIs are realizable. In 2005, Haldane and Raghu first theoretically predicted the photonic topological insulator, where photonic chiral edge states can be achieved by a photonic crystal consisting of Faraday-effect media, which is nonreciprocal and breaks the time-reversal symmetry [24, 25]. The photonic analogue to electronic chiral edge states in the QHE is based on the mathematical equivalence that Maxwell's equations can be rewritten in the form of a Hamiltonian matrix as mentioned above, where the Berry curvature in a photonic system is analogous to the magnetic field in QHE [4, 24, 26].

Later in 2008, this conjecture was first numerically and experimentally verified by an experiment [27] on a quasi-2D square-lattice photonic crystal composed of vanadium-doped calcium-iron-garnet gyromagnetic cylinders under an external magnetic field along cylinder axial direction and sandwiched between upper and lower metal plates. This experiment demonstrated topologically protected backscattering-immune transmission of light, which is supported by the magneto-optical Faraday effect – the non-diagonal elements of gyromagnetic permeability tensor break the system's time-reversal symmetry, thus breaking the reciprocity of electromagnetic wave transmission to support one-way transmission along the edge of the photonic crystal, which is similar to how a magnetic field supports electronic unidirectional edge state in a topological insulator [27]. Similar to electron TIs, the number of possible photonic edge states equals the difference of the sum of the Chern numbers of photonic bands below the band gap between two materials [28], while photonic band is defined as the optical dispersion band in reciprocal lattice. In this experiment of [27], the photonic one-way edge state is observed along the boundary of photonic lattice under the transverse magnetic (TM) mode, where the photonic bands are topologically nontrivial with non-zero Chern numbers.

The study of topological optics has been generalized from photonic crystals to metamaterials and metasurfaces [16, 29, 30], from the analogous of quantum Hall states to the analogous of quantum spin hall effect and quantum valley hall effect [31], and from 1D, 2D to higher dimensions [28]. As the analogue between photonic systems and electronic systems is mathematically rigorous, the conclusions of topological optics also apply to condensed matters. The advantages of optical systems over electronic systems leads to a rapidly increasing interest

in topological optics for both theoretical and applied studies. Firstly, for the theoretical studies on the condition and characteristics of nontrivial topologies, the optical systems have higher degrees of freedom and more controllable parameters compared to quantum systems. Therefore, some topological states hardly exhibited in quantum systems can be easily achieved in optics. Secondly, regarding the neutral charge of photons, they have quicker transmission speed and lower heat dissipation than electrons, which benefit the robust control of carriers' path [27]. Besides, the extremely low temperature requirement in quantum topological states is eliminated in optics. Because photons are spinless and non-interactive in linear regime, they wave irrelevantly to temperature.

Non-Hermitian optics and its topology

Another advantage of topological optics is that the non-Hermiticity can be easily implemented into the optical platform by adding gain and loss. The Hermitian symmetry of Hamiltonian, i.e., $H = H^{\dagger}$, is an elementary assumption in quantum mechanics. Hermitian conjugate $H^{\dagger}$ of matrix H is the simultaneous operations of matrix transpose and complex conjugate, i.e., if $H = \begin{bmatrix} a & b \\ c & d \end{bmatrix}$, $H^{\dagger} = \begin{bmatrix} a^* & c^* \\ b^* & d^* \end{bmatrix}$. It can be easily deduced that, if $H = H^{\dagger}$, the Hamiltonian matrix has orthonormal eigenvectors and real eigenvalues, of which the physical meanings are the energy conservation of isolated system (no particle exchange) and the real value of physical observables. While for non-Hermitian system where $H \neq H^{\dagger}$, the Hamiltonian has non-orthonormal eigenvectors and complex eigenvalues in general, representing the non-conserved energy and the complex observables, except for some PT symmetric systems. Therefore, non-Hermiticity is suitable for non-ideal open systems having energy transfer with environments.

As for the topology in non-Hermitian systems, due to the exemption of $H = H^{\dagger}$ requirement, non-Hermitian systems have more degrees of freedom, resulting in more diverse topological classifications and phenomena. All these similar or distinct properties of Hermitian and non-Hermitian topologies can be understood from the similarities or distinctions of Hamiltonian matrix under two cases. For example, when energy conservation is broken, all kinds of symmetries – such as parity, time reversal, particle-hole symmetries – combine with non-Hermiticity and lead to unique topologies [32] and spectral singularities [33, 34]. Some of

which can be regarded as derivatives of Hermitian topology, such as generalized Brillion zone and non-Hermitian bulk-edge correspondence based on non-Bloch complex band theory [32, 35], while others don't have Hermitian counterparts, such as skin effect, non-Hermitian PT symmetry, exceptional point, and point gaps [36-38].

Due to the ability to describe open system and the higher degrees of freedom, the studies of non-Hermitian topology have become popular, of which many are conducted in optical systems because of the rigorous equivalence between the optical system and condensed matter. In quantum mechanics, non-Hermitian originally refers to the non-unitary time-evolution, which appears in nuclear decay process [33, 39]. Generalized to optical systems, the non-Hermiticity can be formulated in two ways [39]:

One is the formal equivalence between one-body Schrodinger equation ($i\hbar\frac{\partial\psi}{\partial t} = -\frac{\hbar^2}{2m}\frac{\partial^2\psi}{\partial x^2} + V(x)\cdot\psi$) and solution of Maxwell's equation of paraxial wave propagating along z-direction in a z-independent system ($-i\frac{\partial E}{\partial z} = \frac{1}{2k}\frac{\partial^2 E}{\partial x^2} + k_0\cdot n(x)\cdot E$). The corresponding term of electron's potential $V(x)$ in wave equation is the refractive index $n(x)$. The values of $V(x)$ and $n(x)$ are complex for non-Hermitian system in quantum and optics, respectively, where the imaginary part of $n(x)$ stands for optical gain/loss. Another is the scattering matrix of linear complex media, where the gain or loss may break the unitarity of scattering matrix $\overleftrightarrow{S}$, that is, $\overleftrightarrow{S}^{\dagger}\overleftrightarrow{S} \neq \overleftrightarrow{I}$ may happen for non-Hermitian system. Meanwhile, another conservation generalized from unitarity is preserved in PT-symmetric non-Hermitian system [39].

From this perspective of wave, non-Hermiticity can be easily implemented in the optical system by complex refractive index. And from the view of quantum, photons as bosons don't need to perceive real energy and conservation of particle number, which are necessary for electrons as fermions. Therefore, it's more convenient to study non-Hermiticity in optics.

1.3 Research gap and research aim

The critical issue of theoretical study is to figure out how non-Hermiticity affects the topological order of the system, and the possible emergence of novel topological phases in energy non-conserved systems [40]. It is easy to understand that the reason for higher degrees of freedom in non-Hermitian topology is the absence of Hermitian symmetry. However, as non-Hermiticity interplays with other various symmetries and environments, the cases become complicated. As a result, the classification of non-Hermitian band topology is still incomplete. Compared to the Altland-Zirnbauer classification [41] – which classifies Hermitian topology according to the preservation or elimination of time-reversal symmetry, particle-hole symmetry, and chiral symmetry, currently the theoretical study on the effect of various symmetries on non-Hermitian topology is not unified and incomplete [40].

The combination of non-Hermitian topology and optics opens a new window for theoretical exploration, and offers opportunities for multiple applications in optics. So far, numerous studies and results have been achieved in non-Hermitian topological optics [28, 40, 42, 43], where the nontrivial topology can often be characterized by optical singularities. The singularities can be polarization singularities [44, 45], phase singularities and so on, and they can be in parameter space [46] or real space [47, 48]. The singularities can be applied to modulation of amplitude, polarization, and phase (using the vortex field surrounding the singularity) [18, 49], as well as optical isolators in a nonreciprocal system (using the zero amplitude at singularity).

To aid in developing a unified theory, the quantized topological invariant and the conditions for the existence of non-Hermitian optical singularities need to be studied in specifically designed system. There are previous experimental or numerical studies of non-Hermitian topology by adding optical gain [43] or loss to Hermitian topological system, and the application of singularities in specific models, such as the optical phase modulation by singular points in 2D non-Hermitian dielectric and metallic metasurface [18].

Compared to experiments or numerical simulations, analytical studies starting from the electromagnetic first principle could demonstrate quantitative relations between physical observables, thus enabling accurate physical interpretation. For example, the analytical study

of loss-induced phase singularities in a 1D sandwich-structure photonic crystal [50], and proof of the robust existence of transmission singularities in the parameter space of any quasi-1D system [51]. The topological robustness of nonreciprocal gyromagnetic materials with loss is also studied and proven by Green's function method [52]. However, the nonreciprocal non-Hermitian periodic photonic system where the nonreciprocity and loss are separated in different material compositions is seldom studied.

Therefore, this project aims at analytically studying the interplay of nonreciprocity and non-Hermiticity by a non-Hermitian nonreciprocal metasurface model, where the scattered field is computed by the rigorous Mie scattering and multiple scattering theories. The model is 2D but composed of units periodic along one dimension, where each unit contains a gyromagnetic YIG cylinder and a lossy dielectric cylinder. This model can also be regarded as a hybrid of two equal-spacing cylinder arrays. The detailed configuration will be illustrated in Chapter 3.

The reasons for this design are four-fold: Firstly, the cylindrical geometry allows a rigorous solution of the electromagnetic field via Mie theory. Secondly, the material selection targets the study of nonreciprocity and non-Hermiticity: the loss in the dielectric cylinder is the origin of non-Hermiticity, and the gyromagnetic material magnetized by external field supports robust nonreciprocal light transmission. The first successful experiment in photonic TI [27] has aroused a trend of exploring nonreciprocal topological optics using gyromagnetic material to break the Lorentz reciprocity. The use of single-crystal YIG as ferromagnets is suggested in [27], because theoretically this material in single-crystal exhibits low absorption loss [53]. YIG shows strong resonance response in the microwave frequency regime (see it's Mie coefficients in Chapter 2); therefore, with a proper radius comparable to microwave wavelength, YIG cylinder can exhibit a strong resonance peak under periodic plane wave incidence. The non-diagonal elements of the gyromagnetic permeability tensor break time-reversal symmetry and enable nonreciprocal light transmission. Nonreciprocity allows the system to exhibit different optical responses under opposite directions of wave incidences. The topological states in a nonreciprocal system with broken time reversal symmetry are more robust compared to those in reciprocal systems, so nonreciprocal systems are useful for developing robust optical isolators.

Thirdly, this dimer-unit configuration is inspired by 1D Su-Schrieffer-Heeger (SSH) model [54],

which is the simplest quantum system supporting topologically nontrivial states [55]. SSH model is also 1D-periodic composed of array of identical units, where each unit contains two atoms. The tight-binding approximation is considered for the theoretical study of the SSH model, where only nearest neighbor interactions are included. Meanwhile, in this metasurface model – which is a hybrid of two arrays – the interactions between the dielectric array and the YIG array are considered in the form of relative lattice sums (see Chapter 2), referring to some non-local effects from other unit cells. The final reason to study the simple dimer-unit model is its structural flexibility. It can be adapted to generate more complex configurations, such as trimer-unit PT-symmetric system and hexagonal honey-comb or square-lattice 2D structures, by deforming the unit cell or stacking monolayers.

Based on the analytical computation of the field, the study aims to: 1. provide the analytical equation of scattering identities, such as the scattering amplitudes and transmission or reflection coefficients; 2. analyze the dependence of polarization singularities on parameters, and interpret the reason for its existence and robustness; 3. relate the physical observables obtained by classical electromagnetic theory to the identities in non-Hermitian topological optics. The corresponding results imply the interplay of broken time-reversal symmetry and broken chiral symmetry with non-Hermiticity, potentially inspiring the establishment of a non-Hermitian topological theory.

1.4 Conclusion

In Chapter 1, I introduced the development of periodic optical systems and topological optics. Then I established the research aim according to research gap in nonreciprocal non-Hermitian model, and demonstrated the expected methodology by analytical scattering theories and model design. In the subsequent Chapter 2, I will provide the detailed derivation of Mie scattering and multiple scattering theories, from which the rigorous solutions of scattered field of single cylinders and periodic cylinder arrays are obtained. Chapter 3 contains the configuration of the metasurface model, the numerical results of nonreciprocal transmission singularities calculated from Chapter 2 and visualized by Wolfram Mathematica, and the analytical study of the effect of model parameters on singularities. Chapter 4 concludes the study and suggests future works.

Chapter 2. Theoretical methodology

As introduced in Chapter 1, the model to be studied in this project is a 1D-periodic metasurface model, which is a hybrid of multiple cylinder-arrays. In this chapter, I will derive the rigorous analytical solution of the scattered field of plane wave incidence on 1D-periodic structure of cylinder arrays, which is obtained by the classical electrodynamic approach. Specifically, Mie scattering theory and multiple scattering theory are applied with some approximations such as non-dispersive dielectrics. The analytical solution can be flexibly applied to a series of periodic photonic systems of cylinder arrays. As the solution is derived from Maxwell's equations with some additional approximations, it's first-principle and theoretically rigorous, and the only deviation comes from the approximations.

This chapter starts from a glance at the general situation of single-body scattering in Section 2.1. Next, it explains the special case of single cylinder scattering solved by Mie theory, where the behaviors of YIG cylinder (as the origin of nonreciprocity) and dielectric cylinder (as the origin of non-Hermiticity) are studied. Then, Section 2.2 shows the multiple scattering of single array composed of equal-spacing identical cylinders and the hybrid of multiple arrays, where the fields are restricted by Bloch's theorem along the periodic direction.

The scattering theories solve the electromagnetic fields of cylinders under plane wave incidence, according to which the transmitted and reflected fields and coefficients can be computed and the results are given in Section 2.2.2. By comparing the transmitted and reflected fields at opposite incident directions, the nonreciprocity of the model can be analyzed and the analysis will be put in Chapter 3.

2.1 Mie scattering of single cylinder

General scattering theory for particle, scalar wave, and polarized wave

Consider an elastic scattering process of particles or waves on a single scatterer of finite size. As the scattering interaction is localized, the outgoing particles or waves have straight trajectories beyond a certain effective range. Therefore, the information about scattered entities is included in the angular dependence on scattering angles θ and φ (in 3D spherical coordinate) at the far-field, which can be quantified by the differential scattering cross section $c_{sca}(\theta, \varphi)$.

For the radial dependence, the scattered intensity $I_{sca}(\theta, \varphi, r)$ is proportional to r^{-2} in 3D space due to energy conservation; hence, the scattered wave is a spherical wave at the far-field. The above description is general for all substances being scattered, while for electromagnetic waves as polarized vector waves, one additional degree of freedom to be considered is the polarizations of both incident wave and scattered wave. Stokes vector can fully describe the status of a polarized vector wave. A Stokes vector has 4 dimensions, so the Mueller matrix $\overleftrightarrow{M}$ relating the Stokes vector of the polarized scattered wave to that of the incident wave is a 4×4 matrix, and it fully describes the scattering process. Symmetry restrictions can reduce the number of independent elements in $\overleftrightarrow{M}$ matrix [56].

Single cylinder scattering by Mie theory

The scattering process of electromagnetic plane waves on an infinite-length circular cylinder can be described by Mie theory. At its first establishment, Mie theory gave the solution of the scattered field of a plane wave incidence on a homogenous sphere of arbitrary radius. The solution is rigorously derived from Maxwell's equations and boundary continuity requirements, and it approaches Rayleigh scattering – when the sphere is much smaller than the wavelength; or geometric optics – when the sphere is much larger. The geometry of the scatterer can be generalized to any shape for which the separation of variable is applicable under spherical or cylindrical coordinates, such as an infinite-length circular cylinder [56] or concentrically coated cylinder or sphere [57]. The medium can be isotropic, i.e., dielectric, or anisotropic, i.e., gyromagnetic material [58]. Next, I will show and analyze the rigorous solution of scattered field obtained by Mie theory for YIG cylinder and dielectric cylinder, where the derivation is put in Appendix A.

Scattering fields represented by Mie coefficients

Consider the scattering problem of plane wave incidence on an infinite-length circular cylinder embedded in vacuum (Figure A.1), where the incident wave vector is normal to cylinder axis and the incident wave is in transverse electric (TE) mode with E_z polarization, because the system in transverse magnetic (TM) incidence with B_z polarization has no nonreciprocal effect and the reason will be discussed later. The system has chiral symmetry. The rigorous

solution (see Appendix A) of the scattered field in cylindrical coordinate (s, ϕ, z) is expressed in cylindrical harmonics after separation of variables s, ϕ, and z:

Assume the incident wave vector $\overrightarrow{k^i}$ forms an angle θ with respect to $+\hat{x}$ (Figure A.1), with the harmonic time dependence $e^{-i\omega t}$, the $\hat{z}$ component of the incident electric field E_z^i can be expressed in the form of cylindrical harmonics as:

$$E_z^i = e^{-i\omega t}\sum_{n=-\infty}^{\infty} J_n(k^0 s)e^{in\left(\frac{\pi}{2}+\phi-\theta\right)},$$

where ω is the angular frequency, $k^0 = \frac{\omega}{c}$ is the angular wave number in vacuum and c is the light speed in vacuum. And according to the derivation in Appendix A, the corresponding scattered field E_z^s in cylindrical harmonics is:

$$E_z^s = e^{-i\omega t}\sum_{n=-\infty}^{\infty} b_n H_n^{(1)}(k^0 s)e^{in\left(\frac{\pi}{2}+\phi-\theta\right)},$$

where b_n is the dimensionless Mie scattering coefficient of order n.

For a dielectric cylinder of radius r_d and refractive index ndi, its Mie coefficient is:

$$b_n^d = -\frac{ndi\cdot J_n(k^0 r_d)\cdot J_n'(ndi\cdot k^0 r_d) - J_n'(k^0 r_d)\cdot J_n(ndi\cdot k^0 r_d)}{ndi\cdot H_n^{(1)}(k^0 r_d)\cdot J_n'(ndi\cdot k^0 r_d) - H_n^{(1)\prime}(k^0 r_d)\cdot J_n(ndi\cdot k^0 r_d)}.$$

For the gyromagnetic YIG material, its permittivity is $\varepsilon^Y = 15\varepsilon_0$, and its anisotropic magnetic permeability is $\overleftrightarrow{\mu^Y} = \begin{pmatrix} \mu_a & i\mu_p & 0 \\ -i\mu_p & \mu_a & 0 \\ 0 & 0 & 1 \end{pmatrix}\mu_0$ [58] under external magnetic field $\overrightarrow{H_0}$ along $-\hat{z}$.

Therefore, the Mie coefficient of a YIG cylinder of radius r_Y is:

$$b_n^Y = -\frac{J_n(k^0 r_Y)\left[\frac{\mu_a}{{\mu_a}^2-{\mu_p}^2}k^m r_Y J_n'(k^m r_Y)+\frac{\mu_p}{{\mu_a}^2-{\mu_p}^2}nJ_n(k^m r_Y)\right]-k^0 r_Y J_n'(k^0 r_Y)J_n(k^m r_Y)}{H_n^{(1)}(k^0 r_Y)\left[\frac{\mu_a}{{\mu_a}^2-{\mu_p}^2}k^m r_Y J_n'(k^m r_Y)+\frac{\mu_p}{{\mu_a}^2-{\mu_p}^2}nJ_n(k^m r_Y)\right]-k^0 r_Y H_n^{(1)\prime}(k^0 r_Y)J_n(k^m r_Y)},$$

where $k^m = \sqrt{\frac{\varepsilon^Y({\mu_a}^2-{\mu_p}^2)}{\varepsilon_0\mu_a}}k^0$, $\mu_p = \frac{\omega_m\omega}{{\omega_0}^2-\omega^2}$ and $\mu_a = 1+\frac{\omega_m\omega_0}{{\omega_0}^2-\omega^2}$, with $\omega_m = \gamma M_s$ and $\omega_0 = \gamma H_0$, where the gyromagnetic ratio is $\gamma = 2\pi\cdot 2.8\times 10^6\ \frac{rad\cdot Hz}{Oe}$ and saturation magnetization is $M_s = 1750\ Oe$ [17].

According to the expression of E_z^s, each order of the cylindrical harmonic is separated into the radial dependence $b_n H_n^{(1)}(k^0 s)$ and the angular dependence $e^{in\left(\frac{\pi}{2}+\phi-\theta\right)}$. For the radial dependence, Mie coefficient b_n is the ratio of the amplitude of n-th order scattered wave (in Hankel function) to the amplitude of n-th order incident wave (in Bessel function). The norm of b_n is the absolute value of n-th order scattering amplitude under normalized plane wave

incidence, and the normalized scattering cross section is $N_{sca} = \sum_{n=-\infty}^{\infty} |b_n|^2$ [59]. For the angular dependance included in term $e^{in\left(\frac{\pi}{2}+\phi-\theta\right)}$, the value of n represents the angular periodicity. For example, when $n = 0$, E_z^s is independent of ϕ, which implies the concentric scattered field pattern; when $n = 1$, the increasement of phase of E_z^s is synchronized with ϕ as ϕ swipes from 0 to 2π.

The dominant orders

Figure 2.1(a)(b) show the values of b_n^d and b_n^Y of different orders. It can be observed that b_0^d and b_{-1}^Y are dominant at the interested frequency range, and coefficients of other orders are comparatively small. This can be physically interpreted as follows:

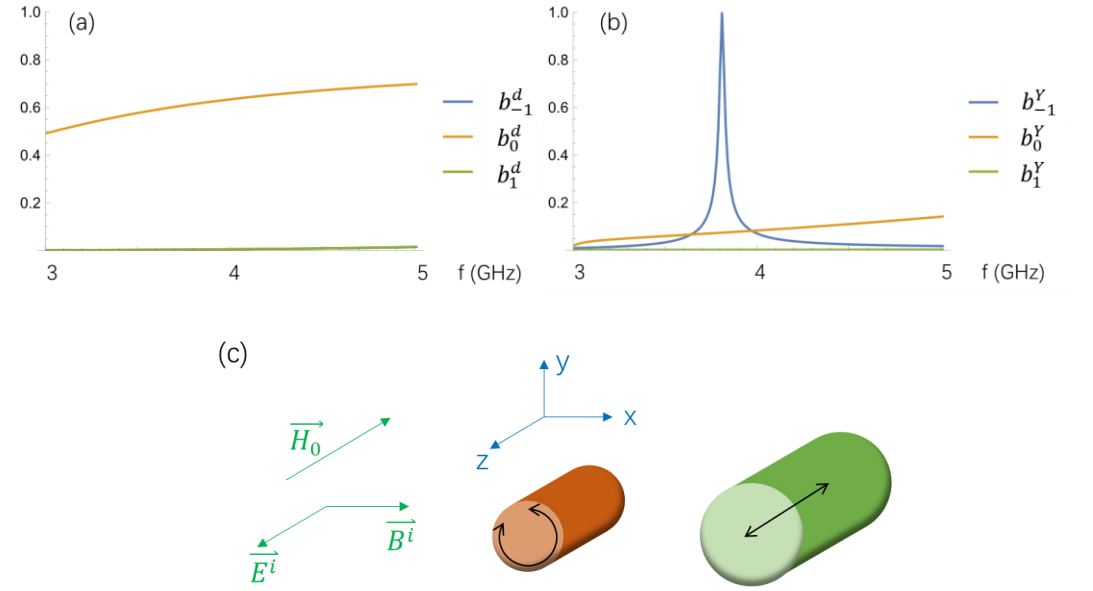

Figure 2.1. The norm of single cylinder Mie scattering coefficients (a) b_n^d and (b) b_n^Y, at $r_d = 2.5\,mm$ and $r_Y = 1\,mm$, $ndi = (23.04 + 12 \times i)^{\frac{1}{2}}$. The incident frequency $f = \frac{\omega}{2\pi} \times 10^{-9}\,GHz$ is between 3 to 5 GHz, the external magnetic field is $H_0 = 500\,Oe$. From Figure 2.1(a), there is $b_n^d = b_{-n}^d$, and this can be algebraically deduced according to the transformation between Bessel functions of positive and negative orders. (c) The induced electric dipole in dielectric cylinder (in green) and the induced magnetic dipole in YIG cylinder (in orange).

Since the incident plane wave has a wave vector normal to cylinder axis ($\hat{z}$ axis) and it's in TE

mode with E_z polarization, the incident electric field $\overrightarrow{E^i}$ is along $\pm\hat{z}$ and the incident magnetic field $\overrightarrow{B^i}$ is in the $\hat{x}-\hat{y}$ plane. Therefore, for the dielectric cylinder, the oscillating $\overrightarrow{E^i}$ induces mainly the electric dipole along $\pm\hat{z}$, whose 0th order scattered field is concentric around $\hat{z}$ axis; for the YIG cylinder, $\overrightarrow{B^i}$ in $\hat{x}-\hat{y}$ plane excites the oscillation of the magnetic dipole (or equivalently the bound current circling in $\hat{x}-\hat{y}$ plane) induced by the external magnetic field $\overrightarrow{H_0}$, whose -1 order scattered field has an angular phase change inversely synchronized with polar angle ϕ. Figure 2.1(c) demonstrates the electric dipole in dielectric cylinder and the magnetic dipole in YIG cylinder.

YIG's nonreciprocity

Lorentz reciprocity says if electromagnetic radiation source and receiver swap positions, the field obtained by receiver stays unchanged, which is one of the default properties of electromagnetic field and can be deduced from Maxwell's equations and constitutive relations [60]. Lorentz reciprocity can be broken in 4 ways [60], one of which is the anisotropic medium with asymmetric permittivity or permeability tensor. In the thesis, the gyromagnetic YIG cylinder magnetized by external magnetic field $\overrightarrow{H_0}$ constitutes a Faraday system, which is a typical nonreciprocal system where time-reversal symmetry is broken due to the time-reversal invariance of $\overrightarrow{H_0}$ [60].

The dominant -1 order scattered field from magnetic dipole in YIG cylinder also explains the nonreciprocity under opposite incidences. When θ becomes θ+π under reversed incidence, the phase of -1 order scattered field has an increase of π according to its angular dependence $e^{i(-1)\left(\frac{\pi}{2}+\phi-\theta\right)}$. This nonreciprocity cannot be observed under TM mode incidence, where the incident magnetic field $\overrightarrow{B^i}$ is along $\pm\hat{z}$ and barely interplays with the magnetic dipole induced by $\overrightarrow{H_0}$.

Algebraic properties of Mie coefficients

It can also be observed from Figure 2.1(b) that a strong resonance peak of YIG's magnetic dipole appears at around $f \approx 3.8\,GHz$ with the maximum value of 1. This can be interpreted by the algebraic properties of Mie coefficients. Since Hankel functions are linear combinations

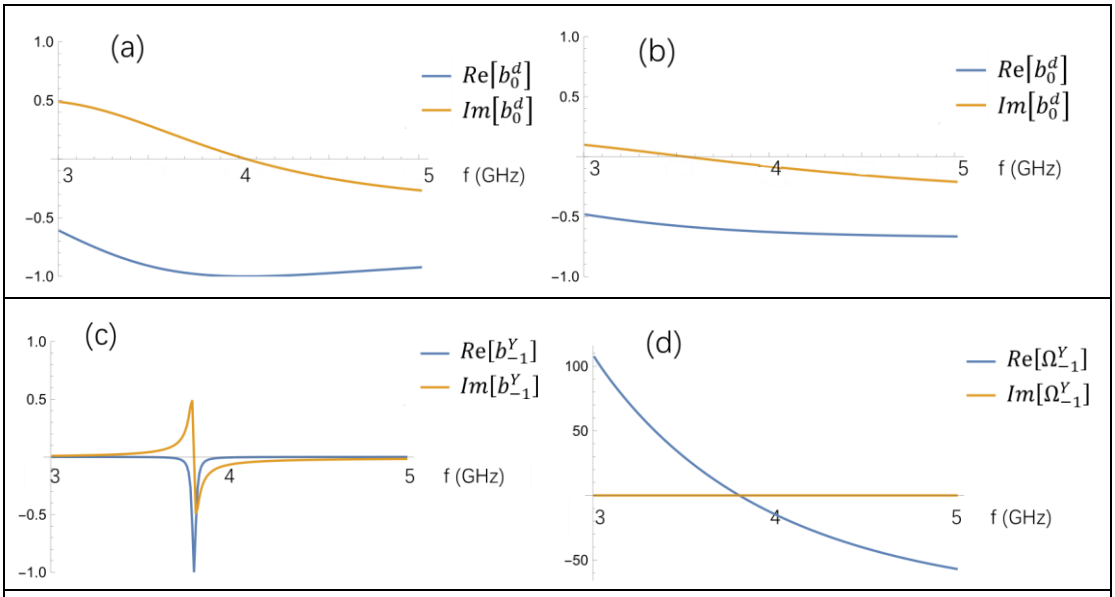

Figure 2.2. Single cylinder Mie scattering coefficients at $r_d = 2.5\,mm$, $r_Y = 1\,mm$, external magnetic field $H_0 = 500\,Oe$. (a) The real and imaginary parts of b_0^d for lossless dielectric, $ndi = \sqrt{23.04}$. b_0^d reaches its maximum value 1 at 4 GHz. (b) The real and imaginary parts of b_0^d for lossy dielectric, $ndi = (23.04 + 12 \times i)^{\frac{1}{2}}$. (c) The real and imaginary parts of b_{-1}^Y. b_{-1}^Y has anabrupt phase change at resonant frequency. (d) The real and imaginary parts of Ω_{-1}^Y. Ω_{-1}^Y has purely zero imaginary part within the frequency range.

of the first and second Bessel functions $H_n^{(1)} = J_n + iY_n$, b_n^d and b_n^Y can be rewritten as $b_n = \frac{1}{1+i\Omega}$ [61]:

$$b_n^d = \frac{-1}{1+i\frac{ndi\cdot Y_n(k^0 r_d)\cdot J_n'(ndi\cdot k^0 r_d) - Y_n'(k^0 r_d)\cdot J_n(ndi\cdot k^0 r_d)}{ndi\cdot J_n(k^0 r_d)\cdot J_n'(ndi\cdot k^0 r_d) - J_n'(k^0 r_d)\cdot J_n(ndi\cdot k^0 r_d)}} = \frac{-1}{1+i\Omega_n^d};$$

$$b_n^Y = \frac{-1}{1+i\frac{Y_n(k^0 r_Y)\left[\frac{\mu_a}{{\mu_a}^2-{\mu_p}^2}k^m r_Y J_n'(k^m r_Y) + \frac{\mu_p}{{\mu_a}^2-{\mu_p}^2} n J_n(k^m r_Y)\right] - Y_n'(k^0 r_Y)k^0 r_Y J_n(k^m r_Y)}{J_n(k^0 r_Y)\left[\frac{\mu_a}{{\mu_a}^2-{\mu_p}^2}k^m r_Y J_n'(k^m r_Y) + \frac{\mu_p}{{\mu_a}^2-{\mu_p}^2} n J_n(k^m r_Y)\right] - J_n'(k^0 r_Y)k^0 r_Y J_n(k^m r_Y)}} = \frac{-1}{1+i\Omega_n^Y}.$$

When $\Omega_n = 0$, Mie coefficient b_n has its maximum value 1 with zero imaginary part. As Ω_n increases to infinity, b_n gradually decreases to its minimum value 0.

The effect of loss on b_0^d

As the total field is $E_z^\beta(s,\phi) = e^{-i\omega t}\sum_{n=-\infty}^{\infty}[J_n(k^0 s) + b_n H_n^{(1)}(k^0 s)]e^{in(\frac{\pi}{2}+\phi-\theta)}$, the phase difference between incident field and scattered field only depends on the argument of b_n and

the phase difference between outputs of J_n and $H_n^{(1)}$. Therefore, argument of b_n influences the interference between the incident E_z^i and scattered field E_z^s thus the value of total field E_z^β. As proved by numerical results in Figure 2.2(a)(b), the loss in dielectric will both decrease the absolute value of b_0^d and induce a phase difference on b_0^d, resulting in the decreased intensity and altered phase of the total field.

The imaginary part of b_n^d comes from the Hankel function and its derivative and the imaginary part of ndi. If ndi is complex due to gain or loss of dielectric medium, it leads to the phase lag in scattered field compared to incident field, which is similar to the phase lag of damped harmonic oscillator compared to the driving force. When ndi becomes its complex conjugate ndi^* (which means a transition from optical loss to gain), Ω_n^d also becomes it complex conjugate Ω_n^{d*} [61], and b_n^d becomes b_n^{d*}. This can be deduced from properties of Bessel functions.

The resonance peak of b_{-1}^Y

For gyromagnetic cylinder, the scattering interaction is more complicated. The external magnetic field H_0 is applied to induce the Larmor precession whose effect is similar to a bound current, resulting in the magnetic moment and the anisotropic magnetic permeability [60]. The damping of the magnetic moment generates -1 order scattered field. The strength of the magnetic moment is determined by the strength of H_0, i.e., μ_a and μ_p are large when ω approaches ω_0. However, the resonant frequency of YIG cylinder is also affected by its radius. From Figure 2.1 and 2.2, when $r_Y = 1\ mm$ and $H_0 = 500\ Oe$, the scattering coefficient b_{-1}^Y has a resonance peak at around 3.8 GHz, which is due to the zero-value of Ω_{-1}^Y.

From the perspective of Ω_{-1}^Y, since ${\mu_a}^2 - {\mu_p}^2 < 0$ at around 3.8 GHz, k^m is imaginary, the numerator and denominator of Ω_{-1}^Y are pure imaginary, so Ω_{-1}^Y has a real value, and $i\Omega_{-1}^Y$ induces b_{-1}^Y's imaginary part. When $\Omega_{-1}^Y = 0$ and $b_{-1}^Y = 1$ at resonance peak around 3.8 GHz, it satisfies:

$$N_n(k^0 r_Y)\left[\frac{\mu_a}{{\mu_a}^2-{\mu_p}^2}k^m r_Y J_n'(k^m r_Y) + \frac{\mu_p}{{\mu_a}^2-{\mu_p}^2}nJ_n(k^m r_Y)\right] = N_n'(k^0 r_Y)k^0 r_Y J_n(k^m r_Y),$$

of which the physical meaning is $E_z^s \cdot H_\phi^\alpha = H_\phi^s \cdot E_z^\alpha$ according to Appendix A, where E_z^s, E_z^α, H_ϕ^α, and H_ϕ^s are electromagnetic field components in cylindrical coordinates.

The matrix formalism

The above solution of scattered field: $E_z^s = e^{-i\omega t}\sum_{n=-\infty}^{\infty} b_n H_n^{(1)}(k^0 s)e^{in(\frac{\pi}{2}+\phi-\theta)}$ can be formulated in matrix form:

$$E_z^s = e^{-i\omega t}\vec{H}\cdot\overleftrightarrow{T}\cdot\overrightarrow{p^{in}},$$

where the plane wave incidence $\overrightarrow{p^{in}} = \left[e^{im\left(\frac{\pi}{2}-\theta\right)}\right]$, Hankel term $\vec{H} = \left[H_n^{(1)}(k^0 s)e^{in\phi}\right]^T$, transition matrix $\overleftrightarrow{T}$ has element $T_{nm} = b_n \cdot \delta_{nm}$. The advantage of the matrix form is that every part has distinguishable physical meaning, and it's easier to separate the effect of different parameters on the scattered field. For example, $\overleftrightarrow{T}$ composed of Mie coefficients only depends on the independent scattering process of each single cylinder; $\overrightarrow{p^{in}}$ only depends on the incident angle. In computer calculation by Wolfram Mathematica, the orders n can only be summed in a finite range from -v to v, which is the truncated order approximation.

2.2 Multiple scattering of cylinders in periodic arrays

2.2.1 Scattering amplitudes

Firstly, consider the scattered field of multiple parallel infinite-length circular cylinders (Figure 2.3(a)) for the general case. In multiple scattering problem, the incident field faced by each scatterer is the vector sum of the external-sourced incident plane wave and the secondary scattered fields from all other scatterers. This expression implies the independent scattering assumption, where the intrinsic scattering process of a cylinder will not be influenced by other cylinders, only the incident field faced by it will be influenced by scattering waves from other cylinders. To analyze the collective effect, consider the mutual influence among cylinders as follows:

For the cross section of a system of M parallel cylinders (Figure 2.3(a)), construct a polar coordinate $\vec{r} = (s, \phi)$ whose origin is at the center of j-th cylinder. The incident field faced by the j-th cylinder $E_z^{i(j)}$ can be written as the sum of plane wave incidence and the scattered fields from all the other cylinders:

$$E_z^{i(j)} = e^{-i\omega t} \sum_{n=-\infty}^{\infty} \left[J_n(k^0 s) e^{in\left(\frac{\pi}{2}+\phi-\theta\right)} + \sum_{l=1, l\neq j}^{M} a_n^l H_n^{(1)}\left(k^0 s^l\right) e^{in\left(\frac{\pi}{2}+\phi^l-\theta\right)} \right],$$

where the secondary radiation is from the l-th cylinder counted from 1 to M, except for the j-th cylinder. a_n^l is the n-th order scattering coefficient (scattering amplitude under normalized incident amplitude) of l-th cylinder in the multiple scattering system, $\overrightarrow{r_{lj}} = (s^l, \phi^l)$ is the displacement vector from the center of l-th cylinder to the center of j-th cylinder. By the way, this expression implies the ignorance of the difference among secondary scattered fields at different locations (s, ϕ) in the j-th cylinder. In the multiple scatterer system, the scattered field from the j-th cylinder can be written as:

$$E_z^{s(j)} = e^{-i\omega t} \sum_{n=-\infty}^{\infty} a_n^j H_n^{(1)}(k^0 s) e^{in\left(\frac{\pi}{2}+\phi-\theta\right)},$$

where a_n^j is the n-th order scattering coefficient of j-th cylinder. Summing up scattered fields from all cylinders and expressing them in the polar coordinate origin at j-th cylinder (see Figure 2.3(a)), the total scattered field can be written as:

$$E_z^s = e^{-i\omega t} \sum_{l=1}^{M} \sum_{n=-\infty}^{\infty} a_n^l H_n^{(1)}\left(k^0 |\vec{r} + \overrightarrow{r_{lj}}|\right) e^{in\left[\frac{\pi}{2}+\arg\left(\vec{r}+\overrightarrow{r_{lj}}\right)-\theta\right]}.$$

In this equation, the axial and angular dependences of cylindrical harmonics can be transformed

among different polar coordinates using addition theorem, which will be deduced later.

It should be noted that the scattered field of l-th cylinder is related to the incident field faced by it as described in Mie solution. a_n^l is similar to b_n^l, where b_n^l is the scattered amplitude under normalized plane wave incidence, a_n^l is scattered amplitude under the sum of normalized plane wave incidence and the corresponding secondary radiation from all non-l-th cylinders. So a_n^l depends on intrinsic properties of all cylinders (dominantly depends on l-th cylinder) and their relative locations. Due to this mutual dependence, the rigorous solution of multiple scattering is hard to be found. Meanwhile, a generally-adapted numerical solution can be obtained according to the independent transition matrix of each scatterer and relative locations among scatterers, where the transition matrix can only be obtained by recursive algorithm through integral equations [62] or translational matrix method [63].

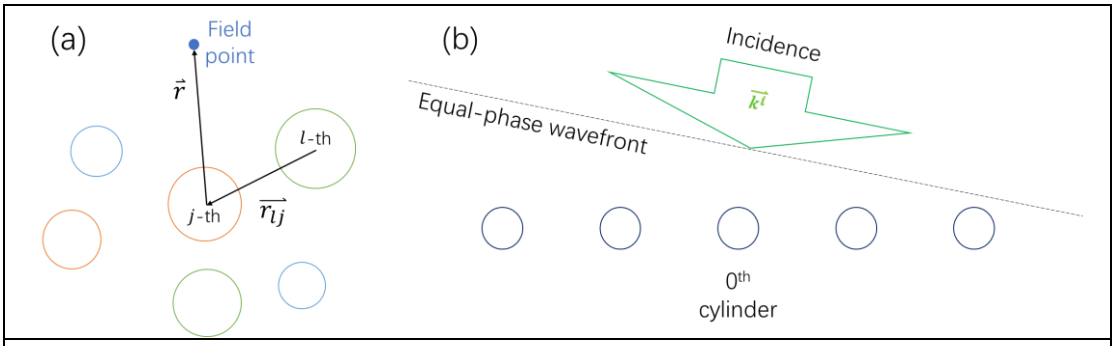

Figure 2.3. (a) M parallel infinite circular cylinders. (b) periodic array of identical cylinders.

Periodic array: one cylinder in unit cell:

Fortunately, some special allocations have additional restrictions on the solutions of fields, thus the scattering fields can be rigorously solved. For example, this project studies the 1D-periodic cylindrical arrays (Figure 2.3 (b)), which follow 1D Bloch's theorem, giving the rigorous solution [64]. Firstly, because all cylinders are identical, their intrinsic scattering properties are the same. Further on, the parallel identical cylinders form an infinite array of periodicity h along $\hat{x}$ direction (Figure 2.3(b)).

Take the j-th cylinder as the 0th cylinder whose center is at the origin, then l is counted from -∞ at -x to ∞ at x. Under $e^{i(\overrightarrow{k^i}\cdot\vec{r}-\omega t)}$ plane wave incidence, at any time, the phase difference of incident plane wave between two neighboring cylinders along $\hat{x}$ is $e^{i(k_x\cdot h)}$ as illustrated in Figure 2.3(b). Two neighboring cylinders respond to incident field identically with the phase

difference $e^{i(k_x \cdot h)}$ according to Bloch's theorem [64]. Correspondingly, the scattered fields from and the secondary radiations received by identical neighboring cylinders follow this phase difference.

As discussed above, the scattered field from the 0th cylinder (whose center is at origin) can be written as:

$$E_z^{s(0)} = e^{-i\omega t} \sum_{n=-\infty}^{\infty} a_n^0 H_n^{(1)}(k^0 s) e^{in\left(\frac{\pi}{2}+\phi-\theta\right)}.$$

The scattered field from the l-th cylinder can be written as:

$$E_z^{s(l)} = e^{-i\omega t} \sum_{n=-\infty}^{\infty} a_n^l H_n^{(1)}(k^0 |\vec{r} + \overrightarrow{r_{l0}}|) e^{in\left(\frac{\pi}{2}+\arg(\vec{r}+\overrightarrow{r_{l0}})-\theta\right)},$$

where $\vec{r} = (s, \phi)$ is the position vector from the center of 0th cylinder to the field point, $\overrightarrow{r_{l0}}$ is the displacement vector from the center of l-th cylinder to the center of 0th cylinder, the argument of any vector is the angle between the vector and $\hat{x}$ direction. Viewed from any field point, the scattered fields $E_z^{s(0)}$ and $E_z^{s(l)}$ from parallel cylinders should be identical except for the phase delay $e^{i(k_x \cdot lh)}$ required by Bloch's theorem. This phase delay and identical responses of parallel cylinders require the relation between their scattering amplitudes as $a_n^l = e^{i(k_x \cdot lh)} \cdot a_n^0$. Therefore, in the space-time scale of the 0th cylinder, the total scattered field from all cylinders reduces to:

$$E_z^s = e^{-i\omega t} \sum_{l=-\infty}^{\infty} \sum_{n=-\infty}^{\infty} e^{i(k_x \cdot lh)} a_n^0 H_n^{(1)}(k^0 |\vec{r} + \overrightarrow{r_{l0}}|) e^{in \cdot \arg(\vec{r}+\overrightarrow{r_{l0}})} e^{in\left(\frac{\pi}{2}-\theta\right)}.$$

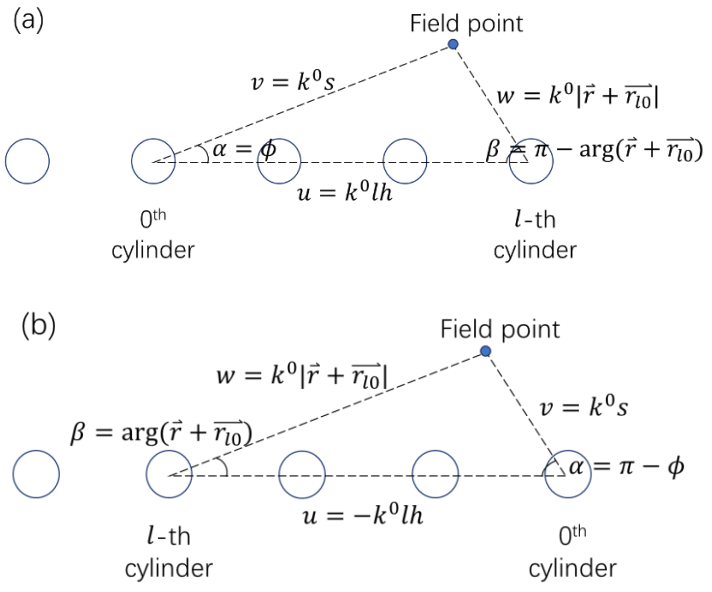

Figure 2.4. Addition theorem applied to 1D-periodic cylinder array, for (a) $l > 0$ case; (b)

$l<0$ case. Any distance is magnified by k^0.

From the well-known Graf's and Gegenbauer's addition theorem of Bessel functions, when $s<|l|h$, the coordinate transform of Hankel function satisfies (Figure 2.4):

$$\begin{cases} H_n^{(1)}(k^0|\vec{r}+\overrightarrow{r_{l0}}|)e^{in\cdot\arg(\vec{r}+\overrightarrow{r_{l0}})}=\sum_{m=-\infty}^{\infty}J_m(k^0s)e^{im(\pi-\phi)}H_{m+n}^{(1)}(k^0|l|h), & for\ l<0 \\ H_n^{(1)}(k^0|\vec{r}+\overrightarrow{r_{l0}}|)e^{in\cdot\arg(\vec{r}+\overrightarrow{r_{l0}})}=e^{in\phi}\cdot H_n^{(1)}(k^0s), & for\ l=0 \\ H_n^{(1)}(k^0|\vec{r}+\overrightarrow{r_{l0}}|)e^{in\cdot[\pi-\arg(\vec{r}+\overrightarrow{r_{l0}})]}=\sum_{m=-\infty}^{\infty}J_m(k^0s)e^{im\phi}H_{m+n}^{(1)}(k^0lh), & for\ l>0 \end{cases}.$$

Replace m by -m for $l<0$ case, and replace n by -n for $l>0$ case. The above equations become:

$$\begin{cases} H_n^{(1)}(k^0|\vec{r}+\overrightarrow{r_{l0}}|)e^{in\cdot\arg(\vec{r}+\overrightarrow{r_{l0}})}=\sum_{m=-\infty}^{\infty}J_{-m}(k^0s)e^{im(\phi-\pi)}H_{n-m}^{(1)}(k^0|l|h), & for\ l<0 \\ H_{-n}^{(1)}(k^0|\vec{r}+\overrightarrow{r_{l0}}|)e^{in\cdot[\arg(\vec{r}+\overrightarrow{r_{l0}})-\pi]}=\sum_{m=-\infty}^{\infty}J_m(k^0s)e^{im\phi}H_{m-n}^{(1)}(k^0lh), & for\ l>0 \end{cases}.$$

Since $J_{-n}(x)=(-1)^nJ_n(x)$ for integer n, with $Y_n(x)=\frac{\cos(n\pi)J_n(x)-J_{-n}(x)}{\sin(n\pi)}$ and $H_n^{(1)}(x)=J_n(x)+iY_n(x)$, it can be deduced that $H_{-n}^{(1)}(x)=(-1)^nH_n^{(1)}(x)$ for integer n. Use this relation to transform $J_{-m}(k^0s)$ term in $l<0$ equation, and $H_{-n}^{(1)}(k^0|\vec{r}+\overrightarrow{r_{l0}}|)$ and $H_{m-n}^{(1)}(k^0lh)$ terms in $l>0$ equation to further reduce above equations:

$$H_n^{(1)}(k^0|\vec{r}+\overrightarrow{r_{l0}}|)e^{in\cdot\arg(\vec{r}+\overrightarrow{r_{l0}})}=\begin{cases}\sum_{m=-\infty}^{\infty}J_m(k^0s)e^{im\phi}H_{n-m}^{(1)}(k^0|l|h), & for\ l<0 \\ e^{in\phi}\cdot H_n^{(1)}(k^0s), & for\ l=0 \\ \sum_{m=-\infty}^{\infty}J_m(k^0s)e^{im\phi}H_{n-m}^{(1)}(k^0lh)(-1)^{n-m}, & for\ l>0\end{cases}.$$

Since the Hankel term $H_{n-m}^{(1)}(k^0lh)$ can be transformed to $(-1)^{m-n}H_{m-n}^{(1)}(k^0lh)$, the above equations are also equivalent to:

$$H_n^{(1)}(k^0|\vec{r}+\overrightarrow{r_{l0}}|)e^{in\cdot\arg(\vec{r}+\overrightarrow{r_{l0}})}=\begin{cases}\sum_{m=-\infty}^{\infty}J_m(k^0s)e^{im\phi}H_{m-n}^{(1)}(k^0|l|h)(-1)^{m-n}, & for\ l<0 \\ e^{in\phi}\cdot H_n^{(1)}(k^0s), & for\ l=0 \\ \sum_{m=-\infty}^{\infty}J_m(k^0s)e^{im\phi}H_{m-n}^{(1)}(k^0lh), & for\ l>0\end{cases}.$$

Now the Hankel terms in the expression of total scattered field E_z^s can be rewritten according to the above coordinate transform rules. Separate the summation of l to three sections: $(-\infty,-1]$, 0, and $[1,\infty)$; then rewrite Hankel terms by transform rules for each range of l; and replace l by positive integer $-l$ for $l<0$ case to combine all Hankel terms where $l\neq 0$; then E_z^s becomes:

$$E_z^s=e^{-i\omega t}\sum_{n=-\infty}^{\infty}a_n^0e^{in\left(\frac{\pi}{2}-\theta\right)}\left\{\sum_{l=1}^{\infty}\sum_{m=-\infty}^{\infty}J_m(k^0s)e^{im\phi}H_{n-m}^{(1)}(k^0lh)\left[e^{-i(k_x\cdot lh)}+\right.\right.$$

$$(-1)^{n-m}e^{i(k_x\cdot lh)}\Big] + e^{in\phi}\cdot H_n^{(1)}(k^0 s)\Big\}.$$

The total field E_z as the sum of plane wave incidence E_z^i (see Section 2.1, here n is replaced by m. This requires m = n, which implies the correspondence of incident order to scattered order) and total scattered field E_z^s equals to:

$$E_z = e^{-i\omega t}\sum_{m=-\infty}^{\infty} J_m(k^0 s)e^{im\phi}\Big\{e^{im\left(\frac{\pi}{2}-\theta\right)} + \sum_{l=1}^{\infty}\sum_{n=-\infty}^{\infty} a_n^0 e^{in\left(\frac{\pi}{2}-\theta\right)} H_{n-m}^{(1)}(k^0 lh)\cdot$$
$$\left[e^{-i(k_x\cdot lh)} + (-1)^{n-m}e^{i(k_x\cdot lh)}\right]\Big\} + e^{-i\omega t}\sum_{n=-\infty}^{\infty} a_n^0 e^{in\left(\frac{\pi}{2}+\phi-\theta\right)}\cdot H_n^{(1)}(k^0 s).$$

Rewrite the above equation of E_z in matrix form:

$$E_z = e^{-i\omega t}\cdot\left[\vec{J}\cdot\left(\overrightarrow{p^{in}} + \overleftrightarrow{LS}\cdot\overrightarrow{a^0}\right) + \vec{H}\cdot\overrightarrow{a^0}\right],$$

where the plane wave incidence is $\overrightarrow{p^{in}} = \left[e^{im\left(\frac{\pi}{2}-\theta\right)}\right]_m$; Bessel term $\vec{J} = \left[J_m(k^0 s)e^{im\phi}\right]_m^T$; Hankel term $\vec{H} = \left[H_n^{(1)}(k^0 s)e^{in\phi}\right]_n^T$; scattering amplitude $\overrightarrow{a^0} = \left[a_n^0 e^{in\left(\frac{\pi}{2}-\theta\right)}\right]_n$, where its n-th element includes the angular dependence; lattice sum $\overleftrightarrow{LS}$ is an infinite-dimensional square matrix with dimensionless element $LS_{mn} = \sum_{l=1}^{\infty} H_{n-m}^{(1)}(k^0 lh)\cdot\left[e^{-i(k_x\cdot lh)} + (-1)^{n-m}\cdot e^{i(k_x\cdot lh)}\right]$, or equivalently $LS_{mn} = \sum_{l=1}^{\infty} H_{m-n}^{(1)}(k^0 lh)\cdot\left[e^{i(k_x\cdot lh)} + (-1)^{m-n}\cdot e^{-i(k_x\cdot lh)}\right]$. Here the square bracket represents a column vector; each component of the vector varies with its subscript; and the superscript T means transposing the column vector to a row vector.

The advantage of the matrix form of E_z is that the incident field and the scattered field of 0th cylinder are distinct from each other, as pure Hankel terms represent outgoing waves whose n-th order amplitude is the n-th element of $\overrightarrow{a^0}$, and the terms including Bessel functions represent incident waves faced by the 0th cylinder whose m-th order amplitude is the m-th element of $\left(\overrightarrow{p^{in}} + \overleftrightarrow{LS}\cdot\overrightarrow{a^0}\right)$. Following Mie solution of the 0th cylinder scattering, the ratio of the n-th order scattered amplitude to the m-th order incident amplitude is b_n, which in matrix form is:

$$\overrightarrow{a^0} = \overleftrightarrow{T}\cdot\left(\overrightarrow{p^{in}} + \overleftrightarrow{LS}\cdot\overrightarrow{a^0}\right),$$

where $\overleftrightarrow{T}$ with element $T_{nm} = b_n\cdot\delta_{nm}$ is the transition matrix of the 0th cylinder as introduced in Section 2.1. The above equation can be rewritten to obtain the dependence of the scattered amplitude $\overrightarrow{a^0}$ on the plane wave incidence amplitude $\overrightarrow{p^{in}}$:

$$\overrightarrow{a^0} = \left(\vec{\vec{I}} - \vec{\vec{T}} \cdot \vec{\vec{LS}}\right)^{-1} \cdot \vec{\vec{T}} \cdot \overrightarrow{p^{in}}.$$

According to the translational symmetry along $\hat{x}$, every cylinder can be defined as the 0th cylinder. Thus, $\overrightarrow{a^0} = \left[a_n^0 e^{in\left(\frac{\pi}{2}-\theta\right)}\right]_n$ is equivalent for all cylinders in array thus can be renamed as $\vec{a}=\left[a_n e^{in\left(\frac{\pi}{2}-\theta\right)}\right]_n$.

Periodic array: more than one cylinders in unit cell:

For the case that each unit contains N cylinders instead of one cylinder, assume the array is still periodic along $\hat{x}$ with the same lattice parameter h, then the scattering amplitudes are still solvable with additional consideration on the intercell and intracell effects.

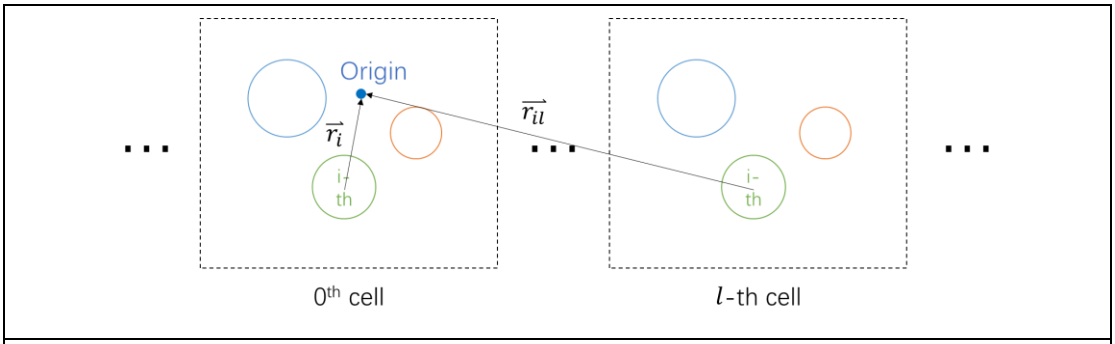

Figure 2.5. Periodic array when a unit cell includes N cylinders.

In this case, we can define the polar coordinate $\vec{r} = (s, \phi)$ whose origin is at some point in the 0th unit cell (Figure 2.5), then the total scattered field E_z^s from all cylinders at any field point $\vec{r}$ can be written as:

$$E_z^s = e^{-i\omega t} \sum_{l=-\infty}^{\infty} \sum_{i=1}^{N} \sum_{n=-\infty}^{\infty} H_n^{(1)}(k^0|\vec{r} + \overrightarrow{r_{il}}|) e^{in\left[\frac{\pi}{2}+\arg(\vec{r}+\overrightarrow{r_{il}})-\theta\right]} \cdot a_n^{il},$$

where a_n^{il} is the n-th order scattering amplitude of the i-th cylinder in the l-th unit cell, $\overrightarrow{r_{il}}$ is the displacement vector from the i-th cylinder in the l-th unit cell to the origin, so $\overrightarrow{r_{il}} = \vec{r_i} - lh\hat{x}$, where $\vec{r_i}$ is the displacement vector from the i-th cylinder in the 0th unit cell to the origin. This yields:

$$E_z^s = e^{-i\omega t} \sum_{i=1}^{N} \sum_{l=-\infty}^{\infty} \sum_{n=-\infty}^{\infty} H_n^{(1)}(k^0|\vec{r} + \vec{r_i} - lh\hat{x}|) e^{in\left[\frac{\pi}{2}+\arg(\vec{r}+\vec{r_i}-lh\hat{x})-\theta\right]} \cdot a_n^{il}.$$

Now consider the scattered field $E_z^{s(i)}$ from all the i-th cylinders in all units:

$$E_z^{s(i)} = e^{-i\omega t} \sum_{l=-\infty}^{\infty} \sum_{n=-\infty}^{\infty} H_n^{(1)}(k^0|\vec{r} + \vec{r_i} - lh\hat{x}|) e^{in\left[\frac{\pi}{2}+\arg(\vec{r}+\vec{r_i}-lh\hat{x})-\theta\right]} \cdot a_n^{il}.$$

Since the expression of $E_z^{s(i)}$ shares the same form with the total scattered field E_z^s when a

unit cell contains only one cylinder after replacing $\vec{r}$ by $\vec{r}+\vec{r_i}$, the Bloch's theorem requires $a_n^{il} = a_n^{i0} \cdot e^{i(k_x \cdot lh)}$, where a_n^{i0} is the n-th order scattering amplitude of the i-th cylinder in the 0th unit cell. This gives:

$$E_z^{s(i)} = e^{-i\omega t} \sum_{n=-\infty}^{\infty} a_n^{i0} e^{in\left(\frac{\pi}{2}-\theta\right)} \sum_{l=-\infty}^{\infty} e^{i(k_x \cdot lh)} H_n^{(1)}(k^0|\vec{r}+\vec{r_l}-lh\hat{x}|) e^{in \cdot \arg(\vec{r}+\vec{r_l}-lh\hat{x})}.$$

Then addition theorem gives:

$$E_z^{s(i)} = e^{-i\omega t} \sum_{n=-\infty}^{\infty} a_n^{i0} e^{in\left(\frac{\pi}{2}-\theta\right)} \cdot \left\{ \sum_{m=-\infty}^{\infty} J_m(k^0|\vec{r}+\vec{r_l}|) e^{im \arg(\vec{r}+\vec{r_l})} \sum_{l=1}^{\infty} H_{n-m}^{(1)}(k^0 lh) \cdot \right.$$
$$\left. \left[e^{-i(k_x \cdot lh)} + (-1)^{n-m} e^{i(k_x \cdot lh)} \right] + H_n^{(1)}(k^0|\vec{r}+\vec{r_l}|) e^{in \cdot \arg(\vec{r}+\vec{r_l})} \right\}.$$

Rewrite $E_z^{s(i)}$ in matrix form:

$$E_z^{s(i)} = e^{-i\omega t} \left(\overrightarrow{J^i} \cdot \overleftarrow{LS} \cdot \overrightarrow{a^{i0}} + \overrightarrow{H^i} \cdot \overrightarrow{a^{i0}} \right),$$

where $\overrightarrow{J^i} = \left[J_m(k^0|\vec{r}+\vec{r_l}|) e^{im \arg(\vec{r}+\vec{r_l})} \right]_m^T$, $\overrightarrow{H^i} = \left[H_n^{(1)}(k^0|\vec{r}+\vec{r_l}|) e^{in \arg(\vec{r}+\vec{r_l})} \right]_n^T$, $\overrightarrow{a^{i0}} = \left[a_n^{i0} \cdot e^{in\left(\frac{\pi}{2}-\theta\right)} \right]_n$. Then the total scattered field E_z^s as a sum of $E_z^{s(i)}$ is:

$$E_z^s = e^{-i\omega t} \sum_{i=1}^{N} \left(\overrightarrow{J^i} \cdot \overleftarrow{LS} \cdot \overrightarrow{a^{i0}} + \overrightarrow{H^i} \cdot \overrightarrow{a^{i0}} \right).$$

And the total field E_z becomes:

$$E_z = e^{-i\omega t} \cdot \vec{J} \cdot \overrightarrow{p^{in}} + e^{-i\omega t} \sum_{i=1}^{N} \left(\overrightarrow{J^i} \cdot \overleftarrow{LS} \cdot \overrightarrow{a^{i0}} + \overrightarrow{H^i} \cdot \overrightarrow{a^{i0}} \right).$$

According to [64] and Section 8.6 of [63], the plane wave incidence can be expressed with respect to local coordinates of all cylinders as:

$$\vec{J} \cdot \overrightarrow{p^{in}} = \sum_{i=1}^{N} \overrightarrow{J^i} \cdot \left[\overleftarrow{\alpha^{i0}} \cdot \overrightarrow{p^{in}} + \sum_{j=1, j\neq i}^{N} \overleftarrow{\xi^{ij}} \cdot \overrightarrow{a^{j0}} \right],$$

where the relative lattice sum is $\overleftarrow{\xi^{ij}} = \overleftarrow{\beta^{ij}} + \overleftarrow{\alpha^{ij}} \cdot \overleftarrow{LS}$, the translation matrix $\overleftarrow{\alpha^{ij}}$ has element $\alpha_{mn}^{ij} = J_{n-m}\left(k^0 \cdot r_{ji}\right) e^{i(n-m)\phi_{ji}}$, and the translation matrix $\overleftarrow{\beta^{ij}}$ has element $\beta_{mn}^{ij} = H_{n-m}^{(1)}\left(k^0 \cdot r_{ji}\right) e^{i(n-m)\phi_{ji}}$, where $\overrightarrow{r_{jl}}$ is defined as the displacement vector from the centre of j-th cylinder to the centre of i-th cylinder, whose absolute value is r_{ji} and polar angle is ϕ_{ji}. Therefore, matrix $\overleftarrow{\alpha^{i0}}$ has element $\alpha_{nm}^{i0} = J_{m-n}(k^0 \cdot r_{0i}) e^{i(m-n)\phi_{0i}}$, where $\overrightarrow{r_{0i}}$ is the displacement vector from the 0th point to the centre of i-th cylinder, where the 0th point is the origin in the 0th unit cell.

The dimensionless element of relative lattice sum is $\xi_{mn}^{ij} = \beta_{mn}^{ij} + \sum_{p=-\infty}^{\infty} \alpha_{mp}^{ij} \cdot LS_{pn} =$

$H_{n-m}^{(1)}\left(k^0 r_{ji}\right)e^{i(n-m)\phi_{ji}} + \sum_{p=-\infty}^{\infty} J_{p-m}\left(k^0 r_{ji}\right)e^{i(p-m)\phi_{ji}} \cdot \sum_{l=1}^{\infty} H_{n-p}^{(1)}(k^0 lh) \cdot \left[e^{-i(k_x \cdot lh)} + (-1)^{n-p} \cdot e^{i(k_x \cdot lh)}\right]$. According to addition theorem, through a process similar to the deduction of lattice sum, the relative lattice sum is equivalent to $\xi_{mn}^{ij} = \sum_{l=1}^{\infty} H_{n-m}^{(1)}\left(k^0 \left| lh\hat{x} + \overrightarrow{r_{jl}} \right|\right) \cdot e^{i(k_x \cdot lh)} \cdot e^{i(n-m)\arg\left(lh\hat{x} + \overrightarrow{r_{jl}}\right)}$ [17, 61, 65], where the physical meaning of $lh\hat{x} + \overrightarrow{r_{jl}}$ is the displacement vector from the j-th cylinder in the 0th unit cell to the i-th cylinder in the l-th unit cell.

Then the total field can be rewritten as:

$$E_z = e^{-i\omega t} \sum_{i=1}^{N} \overrightarrow{J^i} \cdot \left(\overleftrightarrow{\alpha^{i0}} \cdot \overrightarrow{p^{in}} + \overleftrightarrow{LS} \cdot \overrightarrow{a^{i0}} + \sum_{j=1, j\neq i}^{N} \overleftrightarrow{\xi^{ij}} \cdot \overrightarrow{a^{j0}}\right) + e^{-i\omega t} \sum_{i=1}^{N} \overrightarrow{H^i} \cdot \overrightarrow{a^{i0}}.$$

For the i-th cylinder, its incident amplitudes (represented by Bessel terms) and scattered amplitudes (represented by Hankel terms) are associated by Mie solution as:

$$\overrightarrow{a^{i0}} = \overleftrightarrow{T^i} \cdot \left(\overleftrightarrow{\alpha^{i0}} \cdot \overrightarrow{p^{in}} + \overleftrightarrow{LS} \cdot \overrightarrow{a^{i0}} + \sum_{j=1, j\neq i}^{N} \overleftrightarrow{\xi^{ij}} \cdot \overrightarrow{a^{j0}}\right),$$

where $\overleftrightarrow{T^i}$ is the transition matrix of i-th cylinder with element $T_{nm}^i = b_n^i \cdot \delta_{nm}$, from which the dependence of $\overrightarrow{a^{i0}}$ on plane wave incidence $\overrightarrow{p^{in}}$ is:

$$\left(\overleftrightarrow{I} - \overleftrightarrow{T^i} \cdot \overleftrightarrow{LS}\right) \cdot \overrightarrow{a^{i0}} - \overleftrightarrow{T^i} \cdot \sum_{j=1, j\neq i}^{N} \overleftrightarrow{\xi^{ij}} \cdot \overrightarrow{a^{j0}} = \overleftrightarrow{T^i} \cdot \overleftrightarrow{\alpha^{i0}} \cdot \overrightarrow{p^{in}},$$

where $\overrightarrow{p^{in}}$ is associated with both $\overrightarrow{a^{i0}}$ and $\overrightarrow{a^{j0}}$. According to the generating function of Bessel function, the right-hand-side of the above equation can be simplified as $\overleftrightarrow{T^i} \cdot \overleftrightarrow{\alpha^{i0}} \cdot \overrightarrow{p^{in}} = \left[b_n^i \cdot \sum_{m=-\infty}^{\infty} J_{m-n}(k^0 \cdot r_{0i}) e^{i(m-n)\phi_{0i}} e^{im\left(\frac{\pi}{2}-\theta\right)}\right]_n = \left[b_n^i \cdot e^{in\left(\frac{\pi}{2}-\theta\right)} \cdot \sum_{m-n=-\infty}^{\infty} J_{m-n}(k^0 \cdot r_{0i}) \cdot e^{i(m-n)\left(\frac{\pi}{2}-\theta+\phi_{0i}\right)}\right]_n = \left[b_n^i \cdot e^{in\left(\frac{\pi}{2}-\theta\right)} e^{ik^0 \cdot r_{0i} \cdot \sin\left(\frac{\pi}{2}-\theta+\phi_{0i}\right)}\right]_n = \left[b_n^i \cdot e^{in\left(\frac{\pi}{2}-\theta\right)} e^{ik^0 \cdot r_{0i} \cdot \cos(\theta-\phi_{0i})}\right]_n = \left[b_n^i \cdot e^{in\left(\frac{\pi}{2}-\theta\right)} e^{i\overrightarrow{k^i} \cdot \overrightarrow{r_{0i}}}\right]_n$. Here the "i" symbols in the subscript of r and ϕ and superscript of b represent the i-th cylinder, the "i" symbol in $\overrightarrow{k^i}$ represent the incidence, other "i" symbols represent the imaginary unit. This form of $\overleftrightarrow{T^i} \cdot \overleftrightarrow{\alpha^{i0}} \cdot \overrightarrow{p^{in}}$ avoids the inaccuracy of value calculated by computer program, where the sum is up to finite orders of m. With this simplification, the mutual dependence between the i-th and j-th cylinders can be reformulated as the nested matrix form:

$$\begin{bmatrix} \overleftrightarrow{I} - \overleftrightarrow{T^1} \cdot \overleftrightarrow{LS} & \dots & -\overleftrightarrow{T^1} \cdot \overleftrightarrow{\xi^{1N}} \\ \vdots & \ddots & \vdots \\ -\overleftrightarrow{T^N} \cdot \overleftrightarrow{\xi^{N1}} & \dots & \overleftrightarrow{I} - \overleftrightarrow{T^N} \cdot \overleftrightarrow{LS} \end{bmatrix} \begin{bmatrix} \overrightarrow{a^{10}} \\ \vdots \\ \overrightarrow{a^{N0}} \end{bmatrix} = \begin{bmatrix} \left[b_n^1 \cdot e^{in\left(\frac{\pi}{2}-\theta\right)} e^{i\overrightarrow{k^0} \cdot \overrightarrow{r_{01}}} \right]_n \\ \vdots \\ \left[b_n^N \cdot e^{in\left(\frac{\pi}{2}-\theta\right)} e^{i\overrightarrow{k^0} \cdot \overrightarrow{r_{0N}}} \right]_n \end{bmatrix}.$$

This gives the solution of scattering amplitudes of all cylinders in one unit cell. According to the translational symmetry along $\hat{x}$, $\overrightarrow{a^{i0}} = \left[a_n^{i0} \cdot e^{in\left(\frac{\pi}{2}-\theta\right)} \right]_n$ is equivalent for all the i-th cylinders in any unit cell thus can be rewritten as $\overrightarrow{a^i} = \left[a_n^i \cdot e^{in\left(\frac{\pi}{2}-\theta\right)} \right]_n$.

As mentioned above, the advantage of matrix form is that every part has a distinguishable physical meaning, so it's easier to separate the effect of different parameters on the scattering amplitudes and total field. Beside transition matrix $\overleftrightarrow{T}$ and incident wave $\overrightarrow{p^{in}}$, the new terms called lattice sum $\overleftrightarrow{LS}$ and relative lattice sum $\overleftrightarrow{\xi^{ij}}$ are geometric terms, where the lattice sum only depends on k_x and lattice parameter h, and relative lattice sum only depends on the lattice sum and relative locations of cylinders in one unit cell.

In the programme computation of LS_{mn}, similar to cylindrical harmonic order n, the sum of l cannot be counted to infinity thus can only be truncated, i.e. from 1 to lm. While as the series converges slow as l increases, the inaccuracy due to truncation is prominent. In order to save the computation power as well as to reduce inaccuracy, the lattice sum in the programme is defined alternatively according to Appendix A of [66] and supplemental material of [65].

2.2.2 Transmission coefficient and reflection coefficient

For the single cylinder scattering, the scattered field at far-field is still ϕ-dependent. While for cylinder gratings under plane wave incidence, due to the space translational symmetry, the scattered field at far-field is periodic along $\hat{x}$. The scattered field can be expressed in the form of space harmonics, which is the superposition of plane waves toward different directions along different scattering channels sequenced by space harmonic order d, where d can be any integer [64]. The plane wave along the d-th transmitted channel or the reflected channel is the d-th order transmitted wave or reflected wave. Since the incident direction is the 0^{th} order space harmonic, the ratio of d-th order transmitted wave or reflected wave to the incident wave can be denoted by the transmission coefficient t_{d0} or the reflection coefficient r_{d0}. These coefficients contain all information of the scattered field.

For the general case where one unit cell contains multiple cylinders, the expression of total field is stated in Section 2.2.1. The expression of the total field can be transferred from cylindrical harmonics in (s, ϕ) coordinate to space harmonics in (x, y) coordinate following the coordinate transformation rule $\phi = \arctan\frac{y}{x}$ and $s = \sqrt{x^2 + y^2}$. If the incidence $\overrightarrow{k^\iota}$ is downward (i.e. $-\pi < \theta < 0$), then the transmitted field is in the $y < 0$ region and the reflected field is in the $y > 0$ region. After coordinate transform, the d-th order scattered fields when $y < 0$ and $y > 0$ can be expressed in space harmonics as [64]:

$$E_{zd}^{y>0} = r_{d0}^{y>0} e^{i(k_{xd}x + k_{yd}y)};\ E_{zd}^{y<0} = t_{d0}^{y<0} e^{i(k_{xd}x - k_{yd}y)},$$

where $k_{xd} = k_x + \frac{2\pi d}{h}$ and $k_{yd} = \sqrt{(k^0)^2 - {k_{xd}}^2}$ are wave numbers of d-th order waves, $t_{d0}^{y<0}$ and $r_{d0}^{y>0}$ are the d-th order transmission and reflection coefficients. Since the incident 0th order plane wave is along $\overrightarrow{k^\iota}$, the 0th order transmitted wave is along $\overrightarrow{k^\iota} = (k_x, k_y)$ and the 0th order reflected wave is along $\overrightarrow{k^r} = (k_x, -k_y)$. The subscript $d0$ of $t_{d0}^{y<0}$ and $r_{d0}^{y>0}$ represents that the coefficient is the ratio of the d-th order transmitted or reflected wave amplitude to the 0th order incident plane wave amplitude.

According to the definition of k_{yd}, k_{yd} becomes imaginary if $k^0 < \left|k_x + 2\pi\frac{d}{h}\right|$, thus, d-th order space harmonic is evanescent and disappears at far-field. Since the 0th order diffraction always exists at far-field, we can firstly focus on its corresponding transmission and reflection coefficients. For the above assumption of downward incidence $\overrightarrow{k^\iota}$ with $-\pi < \theta < 0$, the 0th order coefficients t_{00}^- and r_{00}^- are [61, 64]:

$$t_{00}^- = 1 + \frac{2}{h(-k_y)}\sum_{j=1}^{N}\sum_{n=-\infty}^{\infty} e^{i\cdot\overrightarrow{k^\iota}\cdot\overrightarrow{r_{j0}}} \cdot a_n^j,$$

$$r_{00}^- = \frac{2}{h(-k_y)}\sum_{j=1}^{N}\sum_{n=-\infty}^{\infty} e^{i\cdot\overrightarrow{k^r}\cdot\overrightarrow{r_{j0}}} \cdot a_n^j \cdot e^{in(-2\theta)},$$

where the term 1 in t_{00}^- represents the transmitted 0th order incident wave, a_n^j is the θ-independent n-th order scattering amplitude in $\overrightarrow{a^j} = \left[a_n^j \cdot e^{in\left(\frac{\pi}{2}-\theta\right)}\right]_n$. To avoid confusion of symbol "i", here any cylinder in unit cell is represented by the j-th cylinder instead of the i-th cylinder. For upward incidence $\overrightarrow{k^\iota}$ with $0 < \theta < \pi$, the 0th order coefficients t_{00}^+ and r_{00}^+ share the similar form with coefficients under downward incidence, the only change is the

replacement of $-k_y$ by k_y:

$$t_{00}^{+} = 1 + \frac{2}{hk_y}\sum_{j=1}^{N}\sum_{n=-\infty}^{\infty} e^{i\cdot\overrightarrow{k^{i}}\cdot\overrightarrow{r_{j0}}}\cdot a_n^j,$$

$$r_{00}^{+} = \frac{2}{hk_y}\sum_{j=1}^{N}\sum_{n=-\infty}^{\infty} e^{i\cdot\overrightarrow{k^{r}}\cdot\overrightarrow{r_{j0}}}\cdot a_n^j\cdot e^{in(-2\theta)}.$$

Chapter 3. Results & discussion

3.1 Model

As introduced in Chapter 1, the system to be studied is a non-Hermitian nonreciprocal metasurface. Specifically, it is a 1D-periodic system composed of dimer units under external static magnetic field $\overrightarrow{H_0}$ along $-\vec{z}$. The incident electromagnetic wave is time-harmonic with frequency f in GHz, and follows E_z polarization in TE mode. The wave vectors are $\pm\overrightarrow{k^i}$ for upward and downward incidences.

Each dimer unit includes one magnetized YIG cylinder and one lossy-dielectric cylinder (Figure 3.1). The relative permittivity and relative permeability of YIG are as discussed in Chapter 2. The relative permeability of dielectric is approximately μ_d = 1 for weak magnetic materials, and the relative permittivity is $\epsilon_d = 23.04 + \epsilon_{Im} \times i$, thus the dielectric refraction index is $ndi = \sqrt{\epsilon_d \mu_d} = \sqrt{23.04 + \epsilon_{Im} \times i}$.

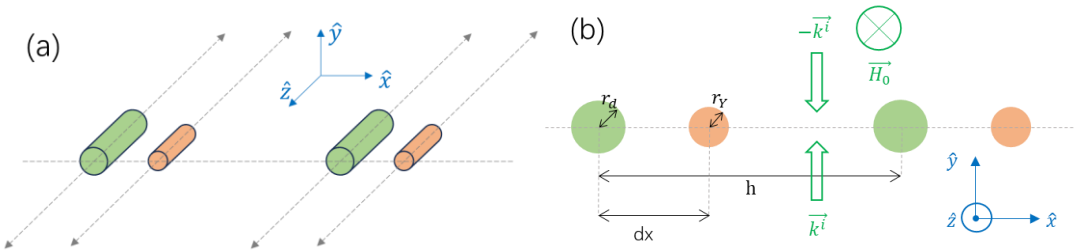

Figure 3.1. The (a) schematic view and (b) cross-sectional view of two neighbouring dimer units in the periodic metasurface. The cylinders are circular and infinite along $\hat{z}$ direction. Each unit cell contains a YIG cylinder (in orange) of radius r_Y = 1 mm and a dielectric cylinder (in green) of radius r_d, all embedded in a vacuum background. H_0 = 500 Oe. The units are periodic along the $\hat{x}$ axis. Lattice parameter h = 50 mm. Centre-to-centre displacement vector from YIG cylinder to dielectric cylinder in the same unit is labelled by $\overrightarrow{r_{Yd}} = (dx, dy)$, whose horizontal projection is dx = –17 mm and vertical projection is dy = 0 mm.

3.2 Topological transmission singularities

The nonreciprocal transmission is studied by comparing the transmissions under upward incidence and downward incidence. The prominence of nonreciprocity can be revealed by taking the ratio of transmission coefficients under opposite incident directions, where the expressions of transmission coefficients can be obtained from Section 2.2.2. Since in our interested cases, the higher-order waves mostly decay (the strict condition will be discussed later), we can consider only the transmitted and reflected waves of 0^{th} space harmonic order, then the ratios can be defined based on the 0^{th} order coefficients:

$$IR = \frac{|t^+|^2}{|t^-|^2};\ CIR = \frac{t^+}{t^-},$$

where t^+ and t^- stand for t_{00}^+ and t_{00}^-. IR represents the isolation ratio, whose physical meaning is the ratio of transmitted energy under opposite incidences; and CIR represents the complex isolation ratio, which retains phase information of transmitted waves.

We can study the dependence of IR and CIR on model parameters which influences the scattered field, to reveal the effect of these parameters on nonreciprocity. From this perspective, IR and CIR can be regarded as functions in parameter spaces. These functions can be visualized by plotting the numerical results computed by Wolfram Mathematica according to the analytical solution provided in the last chapter.

Transmission singularity pair in $f - \epsilon_{Im}$ parameter space

For simplicity, we first consider the case of normal upward and downward incidences. Firstly, due to the resonance of YIG around 3.8GHz, f is expected to have strong effect on nonreciprocal transmission. Secondly, because non-Hermiticity is brought by optical loss, the effect of ϵ_{Im} on transmission is worthy to study. Therefore, IR and CIR in the parameter space of incident frequency f and dielectric loss ϵ_{Im} are plotted in Figure 3.2(a)(b), where a pair of opposite polarization singularities (S_+ and S_-) are found in both functions. The emergence of singularity pair in IR and CIR is due to the singularities in the plot of t^+ and t^- in Figure 3.2(c)(d). In the plot of IR, S_+ and S_- correspond to transmission zeros under downward incidence and upward incidence. In the plot of CIR, t^+, and t^-, the holistic vortex field around the singularities implies they are topologically robust polarization singularities.

For any complex function F such as CIR, t^+, and t^-, its value can be regarded as a 2D vector by taking the real part as the $\hat{x}$ component and the imaginary part as the $\hat{y}$ component. In the

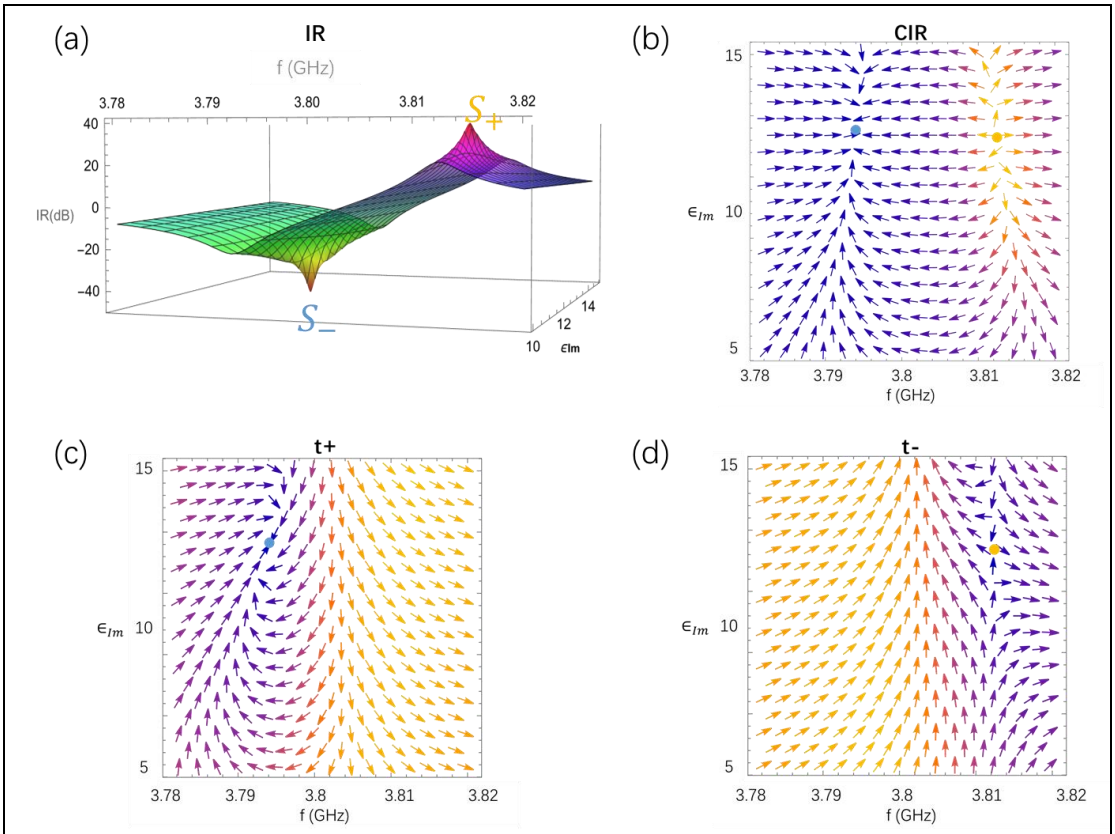

Figure 3.2. (a) IR (in unit decibels) in parameter space $f - \epsilon_{Im}$. At r_d = 2.5 mm. Two opposite singularities S_+ (in orange) and S_- (in blue) emerge in the spectrum of IR. Near the positive singularity S_+, f = 3.811 GHz and ϵ_{Im} = 11.995. Near the negative singularity S_-, f = 3.793 GHz and ϵ_{Im} = 12.382. (b)(c)(d) The vector field of CIR, t^+, and t^-. The magnitude of the vector decreases as color changes from light yellow to dark violet. The locations of S_+ and S_- stay still among (a)(b)(c)(d).

2D parameter space $f - \epsilon_{Im}$, the function can be illustrated as a vector field: $\vec{F}(f, \epsilon_{Im}) = (Re[F(f, \epsilon_{Im})], Im[F(f, \epsilon_{Im})])$, whose polar angle ϕ_p (ranges from 0 to 2π) is equal to the argument of F:

$$\phi_p = arctan \frac{Im[F(f,\epsilon_{Im})]}{Re[F(f,\epsilon_{Im})]}.$$

A topological invariant W called winding number [34, 67] can be used to quantify the nontrivial topology of singularities:

$$W = \frac{1}{2\pi} \oint_l d\phi_p,$$

where l is any arbitrary anticlockwise closed loop on $f-\epsilon_{Im}$ plane around the singularity. Winding number counts how many circles that $\vec{F}$ winds around the point. It can only be an integer due to the compactness of phase space and the continuity of function $\vec{F}$. A nonzero integer winding number indicates the nontrivial topology by identifying the surrounding vortex vector field. Although the parameters $f-\epsilon_{Im}$ aren't periodic thus the boundaries aren't strictly closed, the global vortex field still reflect non-locality of the singularities thus it's robust against small perturbations.

In the vector field of CIR, S_- is a sink and S_+ is a source, both have winding number 1. For the vectorial function F having the same dimension as the manifold (parameter space), the winding number is the Euler characteristic of the manifold. So the vector field of CIR has a total Euler characteristic of 2, which is topologically nontrivial. In the plot of t^+, S_- is a centre with winding number 1. In the plot of t^-, S_+ is a saddle with winding number -1, which is different from the winding number 1 in CIR field because CIR is inversely proportional to t^-.

Evolution of singularities as r_d changes

To study the correlation of S_+ and S_-, the effect of other parameters on function CIR is introduced. Due to the topological robustness, parameters having minor effect are expected to only influence the position of singularities in parameter space but not threaten their existence. To verify this conjecture, I tune the radius of dielectric cylinders r_d to investigate the evolution of two singularities, and the result is illustrated in Figure 3.3. As expected, the singularities S_+ and S_- are found to exist robustly within a continuous range of r_d from 0.4 mm to 2.8 mm (Figure 3.3(a)) with unchanged winding number (Figure 3.3(b)(c)(d)(e)), where S_+ disappears at around r_d = 3 mm.

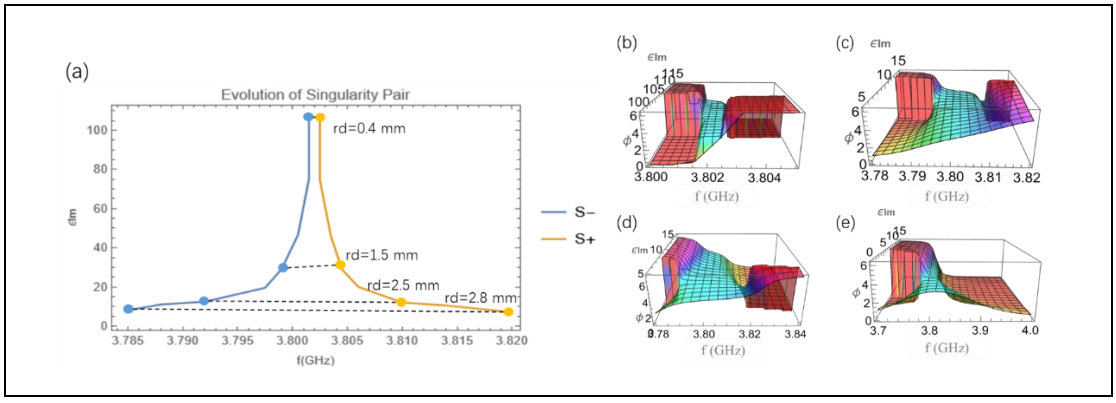

Figure 3.3. (a) Evolution of singularity pair's position in $f-\epsilon_{Im}$ plane as r_d changes. (b)(c)(d)(e) ϕ_p of CIR (represented by the vertical axis, in radian) at r_d = (b) 0.4 mm, (c) 2.5 mm, (d) 2.8 mm, (e) 3 mm. The magnitude of ϕ_p from 0 to 2π is represented by the vertical axis and color. The domain of function ϕ_p varies from (b) to (e).

According to the evolution path of S_+ and S_-, they tend to separate as r_d increases and to merge as r_d decreases. As the Euler characteristic of CIR is 2, the vector field cannot continuously transform to a topologically trivial field with Euler characteristic 0. Therefore, S_+ and S_- are expected to merge into a new singularity with winding number 2 instead of annihilation when they meet. The merging of opposite singularities almost happens at r_d = 0.4 mm. The test of smaller r_d shows S_+ and S_- are hard to coincidence, whose reason will be discussed later. While other parameters, such as h, dx, dy, and r_Y, may influence the locations of singularities, so the merging of S_+ and S_- is possible if the model setting is further adjusted.

Transmission singularities in $f-\theta$ parameter space

The above results are studied under normal upward and downward incidences where $\theta=\pm\frac{\pi}{2}$. However, because the adjustment of incident angle θ is easy to conduct in experiment compared to the adjustment of material parameters, and the incident angle is a key factor of the photonic band, the effect of incidence angle is worth studying. Figure 3.4 shows that the existence of S_+ and S_- in $f-\theta$ parameter space is vague when ϵ_{Im} = 12 and within a range of ϵ_{Im}. In addition, another singularity pair $S_+^{\theta 1}$ and $S_-^{\theta 1}$ in plots of t^+ and t^- at around $\theta_1=\frac{\pi}{4}$ and its counterpart pair $S_+^{\theta 2}$ and $S_-^{\theta 2}$ at around $\theta_2=\frac{3\pi}{4}$ are found (Figure 3.4(b)(c)). The counterpart pair is due to the parity symmetry of model, and opposite singularities already annihilate in CIR (Figure 3.4(a)). These two pairs of transmission singularities at oblique incidence steadily exist within a range of ϵ_{Im} from 11 to 13.

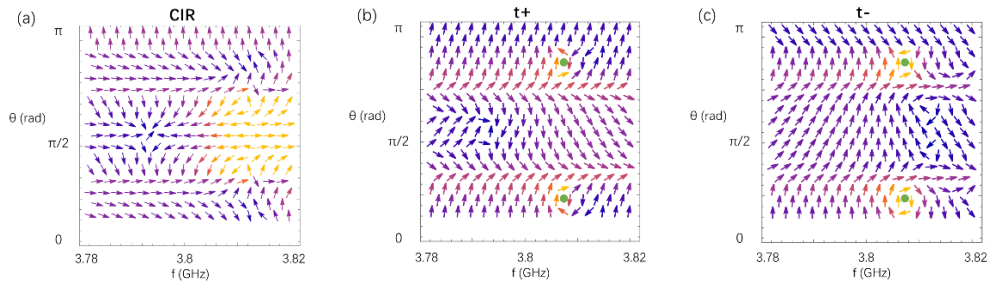

Figure 3.4. The vector field of (a) CIR, (b) t^+, (c) t^-, in parameter space $f-\theta$ at $\epsilon_{Im} = 12$. $S_+^{\theta 1}$ and $S_-^{\theta 1}$ are plotted as green dots.

3.3 Analytical solution of scattering amplitudes and transmission coefficients after dominant harmonic approximation

Section 3.2 numerically illustrates the singularities of transmission coefficients and their evolutions. This section will further investigate how the vortex fields are induced in transmission isolation ratios, and why the singularities are robust against variation of parameters. In this section, the effect of parameters will be studied based on the analytical solution of scattered fields of cylinder-array structure given in Chapter 2.

For the model of dimer unit cells as introduced in Section 3.1, assigning YIG cylinder as the 1st cylinder and dielectric cylinder as the 2nd cylinder in unit cell, then the solution of scattering amplitudes in Section 2.2 reduce to:

$$\begin{bmatrix} \overleftrightarrow{I} - \overleftrightarrow{T^Y} \cdot \overleftrightarrow{LS} & -\overleftrightarrow{T^Y} \cdot \overleftrightarrow{\xi^{Yd}} \\ -\overleftrightarrow{T^d} \cdot \overleftrightarrow{\xi^{dY}} & \overleftrightarrow{I} - \overleftrightarrow{T^d} \cdot \overleftrightarrow{LS} \end{bmatrix} \cdot \begin{bmatrix} \overrightarrow{a^Y} \\ \overrightarrow{a^d} \end{bmatrix} = \begin{bmatrix} \left[b_n^Y \cdot e^{in\left(\frac{\pi}{2}-\theta\right)} e^{i\overrightarrow{k^i}\cdot\overrightarrow{r_{0Y}}} \right]_n \\ \left[b_n^d \cdot e^{in\left(\frac{\pi}{2}-\theta\right)} e^{i\overrightarrow{k^i}\cdot\overrightarrow{r_{0d}}} \right]_n \end{bmatrix},$$

where $\overrightarrow{a^Y}$ and $\overrightarrow{a^d}$ are the scattering amplitudes, $\overleftrightarrow{T^Y}$ and $\overleftrightarrow{T^d}$ are the transition matrixes of YIG cylinders and dielectric cylinders, $\overleftrightarrow{\xi^{Yd}}$ and $\overleftrightarrow{\xi^{dY}}$ are the relative lattice sums. The detailed expressions of every physical quantity in the above equation can be found in Chapter 2. For $\overrightarrow{r_{0Y}}$ and $\overrightarrow{r_{0d}}$, the 0th point (origin) is set at the midpoint of the segment from YIG center to dielectric center. The position of origin in 0th unit cell should not influence the solution of scattered field.

Correspondingly, the 0th order transmission and reflection coefficients under upward and downward incidences $\overrightarrow{k^i}$ with incident angle θ reduce to:

$$t_{00}^{+} = 1 + \frac{2}{hk_y}\sum_{n=-\infty}^{\infty}\left(a_n^Y \cdot e^{i\overrightarrow{k^i}\cdot\overrightarrow{r_{Y0}}} + a_n^d \cdot e^{i\overrightarrow{k^i}\cdot\overrightarrow{r_{d0}}}\right),$$

$$r_{00}^{+} = \frac{2}{hk_y}\sum_{n=-\infty}^{\infty}\left[a_n^Y \cdot e^{in(-2\theta)} \cdot e^{i\overrightarrow{k^r}\cdot\overrightarrow{r_{Y0}}} + a_n^d \cdot e^{in(-2\theta)} \cdot e^{i\overrightarrow{k^r}\cdot\overrightarrow{r_{d0}}}\right],$$

for upward incidence when $0 < \theta < \pi$; and:

$$t_{00}^{-} = 1 + \frac{2}{h(-k_y)}\sum_{n=-\infty}^{\infty}\left(a_n^Y \cdot e^{i\overrightarrow{k^i}\cdot\overrightarrow{r_{Y0}}} + a_n^d \cdot e^{i\overrightarrow{k^i}\cdot\overrightarrow{r_{d0}}}\right),$$

$$r_{00}^{-} = \frac{2}{h(-k_y)}\sum_{n=-\infty}^{\infty}\left[a_n^Y \cdot e^{in(-2\theta)} \cdot e^{i\overrightarrow{k^r}\cdot\overrightarrow{r_{Y0}}} + a_n^d \cdot e^{in(-2\theta)} \cdot e^{i\overrightarrow{k^r}\cdot\overrightarrow{r_{d0}}}\right],$$

for downward incidence when $-\pi < \theta < 0$.

To analytically explain the behaviour of scattered field, it requires the straight-forward quantitative relations among physical observables. However, the above rigorous solutions of amplitudes a_n^Y and a_n^d and coefficients t and r are infinite series of transcendental functions of Bessel's and Hankel's, which is too complicated to be analysed. Although the rigorous solutions can only be truncated to the sums of finite orders in computer software to generate numerical results, the finite series as sum of many orders of transcendental functions is still complicated. Fortunately, observing the scattering amplitudes of different cylindrical orders in Figure 3.5, it's found that for the dimer unit model, a_{-1}^Y and a_0^d are dominant scattering amplitudes at the interested frequency and cylinder radius. In addition, recall that in Chapter 2, Mie coefficients b_{-1}^Y and b_0^d are intrinsically dominant for single YIG and single dielectric cylinders. Other minor orders of b^Y, b^d, a^Y, and a^d have nearly-zero values in our interested parameter range thus have small effects on the scattered fields. Therefore, minor orders of Mie coefficients and scattering amplitudes can be regarded zero, leaving only the -1 order of YIG and 0th order of dielectric. Due to the robustness of topological singularities, this small adjustment should only perturb their positions in parameter space without threatening their existence conditions and winding numbers. This operation is called the dominant harmonic approximation [17, 65], which reduces the original infinite-dimensional nested matrix in the solution of scattering amplitudes to a 2 by 2 matrix, largely simplifying the quantitative relations and enabling the analytical explanation of singularity pairs' emergence and properties.

Figure 3.5. Dependence of scattering amplitudes on frequcney

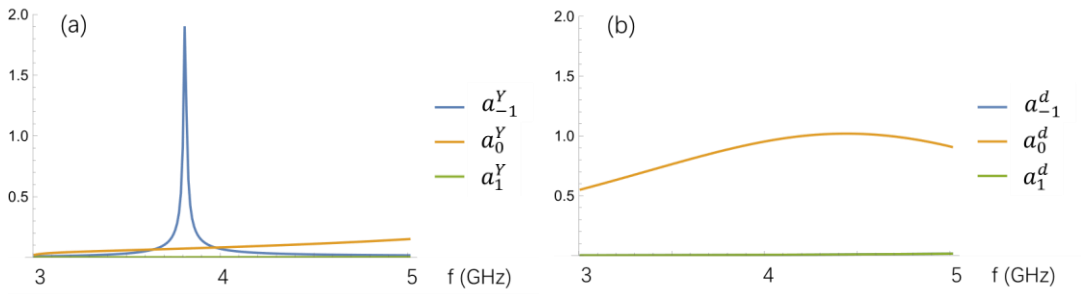

Figure 3.5. Absolute values of scattering amplitudes of (a) $a_n^Y e^{in(\frac{\pi}{2}-\theta)}$ of YIG cylinder and (b) $a_n^d e^{in(\frac{\pi}{2}-\theta)}$ of dielectric cylinder in their own arrays, under normal upward and downward incidences. Both the nonreciprocal YIG array and the reciprocal dielectric array

have reciprocal absolute value of scattering amplitudes.

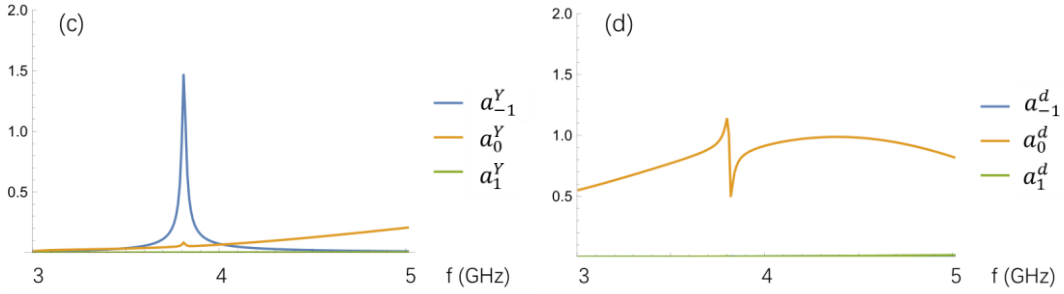

Figure 3.5. Absolute values of scattering amplitudes of (c) $a_n^Y e^{in(\frac{\pi}{2}-\theta)}$ of YIG cylinder and (d) $a_n^d e^{in(\frac{\pi}{2}-\theta)}$ of dielectric cylinder in the dimer-unit array, under normal upward incidence.

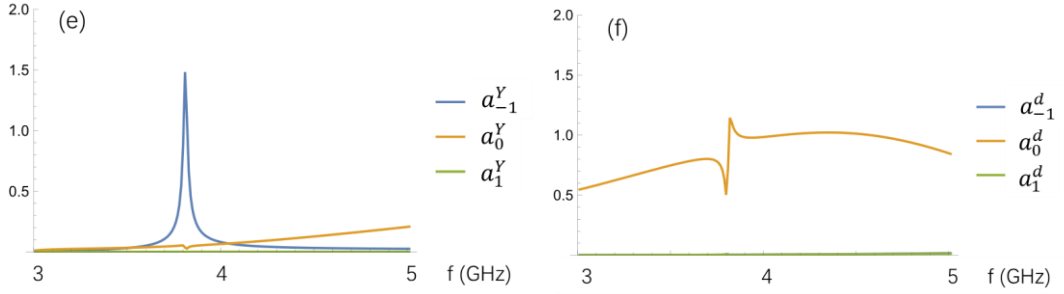

Figure 3.5. Absolute values of scattering amplitudes of (e) $a_n^Y e^{in(\frac{\pi}{2}-\theta)}$ of YIG cylinder and (f) $a_n^d e^{in(\frac{\pi}{2}-\theta)}$ of dielectric cylinder in the dimer-unit array, under normal downward incidence.

As stated, the solution of scattering amplitudes can be simplified by dominant harmonic approximation as follows:

$$\begin{bmatrix} 1-b_{-1}^{Y}\cdot LS_{-1,-1} & -b_{-1}^{Y}\cdot \xi_{-1,0}^{Yd} \\ -b_{0}^{d}\cdot \xi_{0,-1}^{dY} & 1-b_{0}^{d}\cdot LS_{0,0} \end{bmatrix}\cdot\begin{bmatrix} a_{-1}^{Y}\cdot e^{i(-1)\left(\frac{\pi}{2}-\theta\right)} \\ a_{0}^{d}\cdot e^{i\cdot 0\cdot\left(\frac{\pi}{2}-\theta\right)} \end{bmatrix}=\begin{bmatrix} b_{-1}^{Y}\cdot e^{i(-1)\left(\frac{\pi}{2}-\theta\right)}e^{i\vec{k^{i}}\cdot\vec{r_{0Y}}} \\ b_{0}^{d}\cdot e^{i\cdot 0\cdot\left(\frac{\pi}{2}-\theta\right)}e^{i\vec{k^{i}}\cdot\vec{r_{0d}}} \end{bmatrix}.$$

And the transmission and reflection coefficient are simplified to:

$$t_{00}^{+}=1+\frac{2}{hk_y}\left(a_{-1}^{Y}\cdot e^{i\vec{k^{i}}\cdot\vec{r_{Y0}}}+a_{0}^{d}\cdot e^{i\vec{k^{i}}\cdot\vec{r_{d0}}}\right),$$

$$r_{00}^{+}=\frac{2}{hk_y}\left[a_{-1}^{Y}\cdot e^{i(-1)(-2\theta)}\cdot e^{i\vec{k^{r}}\cdot\vec{r_{Y0}}}+a_{0}^{d}\cdot e^{i\cdot 0\cdot(-2\theta)}\cdot e^{i\vec{k^{r}}\cdot\vec{r_{d0}}}\right],$$

$$t_{00}^{-}=1+\frac{2}{h(-k_y)}\left(a_{-1}^{Y}\cdot e^{i\vec{k^{i}}\cdot\vec{r_{Y0}}}+a_{0}^{d}\cdot e^{i\vec{k^{i}}\cdot\vec{r_{d0}}}\right),$$

$$r_{00}^{-}=\frac{2}{h(-k_y)}\left[a_{-1}^{Y}\cdot e^{i(-1)(-2\theta)}\cdot e^{i\vec{k^{r}}\cdot\vec{r_{Y0}}}+a_{0}^{d}\cdot e^{i\cdot 0\cdot(-2\theta)}\cdot e^{i\vec{k^{r}}\cdot\vec{r_{d0}}}\right].$$

So far, the analytical solution of transmission and reflection coefficients after dominant harmonic approximation is found, according to which it's theoretically feasible to explain the behavior of topological singularities in transmission isolation ratios.

To compare the nonreciprocal performances under opposite incidences, we can define the upward incidence angle is $0 < \theta^+ < \pi$ with wave vector $\overrightarrow{k^i} = (k_x, k_y)$, and the downward incidence angle is $\theta^- = \theta^+ - \pi$ with wave vector $-\overrightarrow{k^i} = (-k_x, -k_y)$. Then the solution of scattering amplitudes becomes:

$$\begin{bmatrix} 1 - b_{-1}^{Y} \cdot LS_{-1,-1}^{\pm} & -b_{-1}^{Y} \cdot \xi_{-1,0}^{Yd\pm} \\ -b_0^d \cdot \xi_{0,-1}^{dY\pm} & 1 - b_0^d \cdot LS_{0,0}^{\pm} \end{bmatrix} \cdot \begin{bmatrix} a_{-1}^{Y\pm} \cdot e^{i(-1)\left(\frac{\pi}{2} - \theta^{\pm}\right)} \\ a_0^{d\pm} \cdot e^{i\cdot 0\cdot\left(\frac{\pi}{2} - \theta^{\pm}\right)} \end{bmatrix} = \begin{bmatrix} b_{-1}^{Y} \cdot e^{i(-1)\left(\frac{\pi}{2} - \theta^{\pm}\right)} e^{\pm i\overrightarrow{k^i}\cdot\overrightarrow{r_{0Y}}} \\ b_0^d \cdot e^{i\cdot 0\cdot\left(\frac{\pi}{2} - \theta^{\pm}\right)} e^{\pm i\overrightarrow{k^i}\cdot\overrightarrow{r_{0d}}} \end{bmatrix},$$

where the + and – superscripts stand for the quantities under upward and downward incidences. The lattice sum $LS_{-1,-1}^{+} = LS_{0,0}^{+} = \sum_{l=1}^{\infty} H_0^{(1)}(k^0 lh) \cdot \left[e^{-i(k_x \cdot lh)} + e^{i(k_x \cdot lh)}\right]$, and $LS^+ = LS^-$ when k_x becomes $-k_x$. So all lattice sums can be unified and denoted by $LS = \sum_{l=1}^{\infty} H_0^{(1)}(k^0 lh) \cdot \left[e^{-i(k_x \cdot lh)} + e^{i(k_x \cdot lh)}\right]$. For relative lattice sums, according to the addition theorem, $\xi_{-1,0}^{Yd} = \sum_{l=-\infty}^{\infty} H_1^{(1)}(k^0 |lh\hat{x} + \overrightarrow{r_{dY}}|) e^{i(k_x \cdot lh)}\, e^{i\cdot \arg(lh\hat{x} + \overrightarrow{r_{dY}})}$, and $\xi_{0,-1}^{dY} = \sum_{l=-\infty}^{\infty} H_{-1}^{(1)}(k^0 |lh\hat{x} + \overrightarrow{r_{Yd}}|) e^{i(k_x \cdot lh)}\, e^{-i\cdot \arg(lh\hat{x} + \overrightarrow{r_{Yd}})}$. Then the above solution of amplitudes can be further simplified to:

$$\begin{bmatrix} a_{-1}^{Y\pm} \cdot e^{i(-1)\left(\frac{\pi}{2} - \theta^{\pm}\right)} \\ a_0^{d\pm} \cdot e^{i\cdot 0\cdot\left(\frac{\pi}{2} - \theta^{\pm}\right)} \end{bmatrix} = \begin{bmatrix} 1 - b_{-1}^{Y} \cdot LS & -b_{-1}^{Y} \cdot \xi_{-1,0}^{Yd\pm} \\ -b_0^d \cdot \xi_{0,-1}^{dY\pm} & 1 - b_0^d \cdot LS \end{bmatrix}^{-1} \cdot \begin{bmatrix} b_{-1}^{Y} \cdot p_{-1}^{Y\pm} \\ b_0^d \cdot p_0^{d\pm} \end{bmatrix}$$

$$= \frac{\begin{bmatrix} b_{-1}^{Y}\left(1 - b_0^d \cdot LS\right) & b_0^d\left(b_{-1}^{Y} \cdot \xi_{-1,0}^{Yd\pm}\right) \\ b_{-1}^{Y}\left(b_0^d \cdot \xi_{0,-1}^{dY\pm}\right) & b_0^d\left(1 - b_{-1}^{Y} \cdot LS\right) \end{bmatrix}}{\left(1 - b_{-1}^{Y} \cdot LS\right)\left(1 - b_0^d \cdot LS\right) - \left(b_{-1}^{Y} \cdot \xi_{-1,0}^{Yd\pm}\right)\left(b_0^d \cdot \xi_{0,-1}^{dY\pm}\right)} \cdot \begin{bmatrix} p_{-1}^{Y\pm} \\ p_0^{d\pm} \end{bmatrix},$$

where $p_{-1}^{Y\pm} = e^{i(-1)\left(\frac{\pi}{2} - \theta^{\pm}\right)} e^{\pm i\overrightarrow{k^i}\cdot\overrightarrow{r_{0Y}}}$ and $p_0^{d\pm} = e^{i\cdot 0\cdot\left(\frac{\pi}{2} - \theta^{\pm}\right)} e^{\pm i\overrightarrow{k^i}\cdot\overrightarrow{r_{0d}}}$. And the coefficients under opposite incidences become:

$$t^{\pm} = 1 + \frac{2}{hk_y}\left(a_{-1}^{Y\pm} \cdot e^{\pm i\overrightarrow{k^i}\cdot\overrightarrow{r_{Y0}}} + a_0^{d\pm} \cdot e^{\pm i\overrightarrow{k^i}\cdot\overrightarrow{r_{d0}}}\right),$$

$$r^{\pm} = \frac{2}{hk_y}\left[a_{-1}^{Y\pm} \cdot e^{i(-1)(-2\theta^{\pm})} \cdot e^{\pm i\overrightarrow{k^r}\cdot\overrightarrow{r_{Y0}}} + a_0^{d\pm} \cdot e^{i\cdot 0\cdot(-2\theta^{\pm})} \cdot e^{\pm i\overrightarrow{k^r}\cdot\overrightarrow{r_{d0}}}\right],$$

where $\overrightarrow{k^r} = (k_x, -k_y)$. With the expression of $r^{\pm}$, it can also be deduced that $r^+ = r^-$ for

the model illustrated in Section 3.1 [61, 65], thus, reflection isn't discussed in the topic of nonreciprocity.

As mentioned in Chapter 2, the -1 order of magnetic cylinder represents the scattered field from the magnetic dipole in $\hat{x}-\hat{y}$ plane, and the 0^{th} order of dielectric cylinder represents the scattering field from the electric dipole along $\pm\hat{z}$ polarized by periodic wave. Therefore, physical interpretation (Figure 3.6) of the dominant harmonic approximation is to simplifying the model of two equal-spacing cylinder arrays to a model of two equal-spacing dipole arrays.

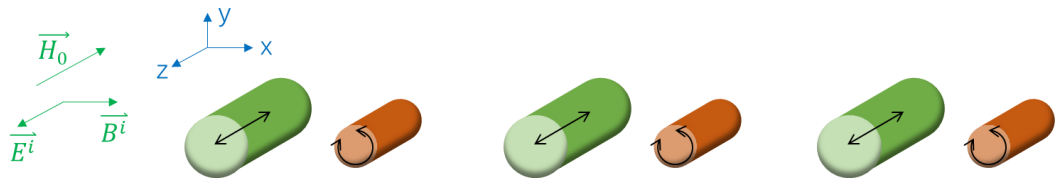

Figure 3.6. Three neighboring dimer units of metasurface model after dominant harmonic approximation.

3.4 Effect of parameters

So far we have obtained full space-time information about the field after dominant harmonic approximation, now we can do analytical explanation of the nontrivial topological singularities according to the approximated solution. All the parameters affecting the values of $a_{-1}^{Y\pm}$, $a_0^{d\pm}$, and $t^{\pm}$ are encoded in the solutions provided in last section, according to which the parameters influencing the amplitudes and coefficients by affecting the variables b_{-1}^{Y}, b_0^{d}, LS, ξ, $p_{-1}^{Y\pm}$, and $p_0^{d\pm}$.

All the relevant parameters are considered as follows: Firstly, for a single dielectric cylinder, b_0^d is determined by permittivity, permeability, and radius. For gyromagnetic YIG cylinder, external magnetic field has additional control on b_{-1}^{Y}. Secondly, for a single array, the distance between neighbouring cylinders h determines LS. Thirdly, for dimer-unit model regarded as hybrid of two arrays, the relative position of two cylinders in the same unit cell $\overrightarrow{r_{Yd}}$ determines ξ. Finally, the output of the dynamic system is influenced by plane wave incidence, not only apparently $p_{-1}^{Y\pm}$, $p_0^{d\pm}$, and $t^{\pm}$ are determined by $\overrightarrow{r_{Yd}}$ and incident wave vector $\overrightarrow{k^i}$; but LS and ξ are also influenced by k^0 and k_x.

Therefore, the model's total degrees of freedom include: r_Y and r_d, ndi, magnetic field H_0, h, $\overrightarrow{r_{Yd}}$ (including dx and dy, or equivalently r_{Yd} and ϕ_{Yd}), $\overrightarrow{k^i}$ (including k_x and k_y, or equivalently k^0, frequency f, and θ). Among all the factors, f, θ, ndi, and r_d will be studied in this section to explain the numerical results in Section 3.2.

3.4.1 Effect of frequency – at normal incidence

Recall that in Section 3.2, robust transmission singularity pair $S^{\pm}$ is found under normal incidence in $f-\epsilon_{Im}$ parameter space. We expect that the analytical solution could explain the following questions: 1. Why singularities appear in this range of frequency and loss? 2. Why singularities appear in pair? 3. Why singularities are robust against the change of r_d? 4. Why singularities are hard to merge? Here I will firstly investigate the effect of f on $a_{-1}^{Y\pm}$ and $a_0^{d\pm}$, then the effect of f on $t^{\pm}$.

3.4.1.1 The dependence of scattering amplitudes on frequency

According to the numerical results of absolute values of $a_{-1}^{Y\pm}\cdot e^{i(-1)\left(\frac{\pi}{2}-\theta^{\pm}\right)}$ and $a_0^{d\pm}\cdot e^{i\cdot 0\cdot\left(\frac{\pi}{2}-\theta^{\pm}\right)}$ as functions of frequency (Figure 3.5), it can be observed that: the resonance peaks of $\left|a_{-1}^{Y\pm}\right|$ in the dimer-unit array (Figure 3.5(c)(e)) are reduced compared to that in the single YIG array (Figure 3.5(a)); and $\left|a_0^{d\pm}\right|$ in the dimer-unit array (Figure 3.5(d)(f))are triggered to generate upward and downward peaks compared to that in the single dielectric array (Figure 3.5(b)), where the triggered peaks of $\left|a_0^{d\pm}\right|$ are antisymmetric under opposite incidence directions. The argument of $a_{-1}^{Y\pm}\cdot e^{i(-1)\left(\frac{\pi}{2}-\theta^{\pm}\right)}$ in the dimer-unit array (Figure 3.7) is also shifted compared to that in the single YIG array.

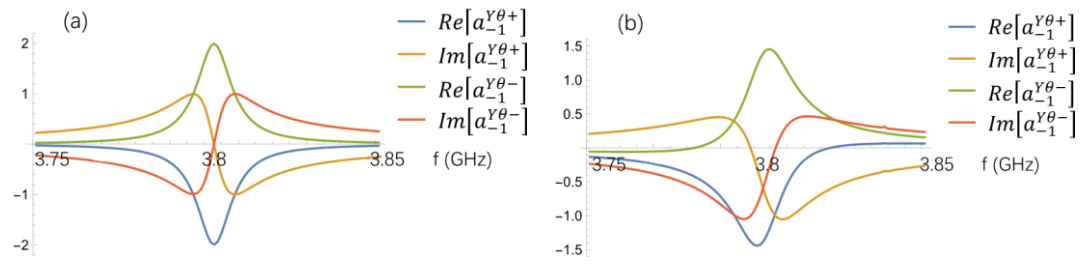

Figure 3.7. Real and imaginary parts of $a_{-1}^{Y\theta\pm}=a_{-1}^{Y\pm}\cdot e^{i(-1)\left(\frac{\pi}{2}-\theta^{\pm}\right)}$ under normal incidences on (a) single YIG array and (b) YIG in hybrid array, where $r_d=2.5\,mm$, $ndi=\sqrt{23.04+12i}$.

To explain these phenomena, the analytical solutions of scattering amplitudes are needed because they reveal the dependences on frequency. For the structure illustrated in Section 3.1, under normal upward incidence $\theta^{+}=\frac{\pi}{2}$, there are $p_{-1}^{Y+}=1$ and $p_0^{d+}=1$; under normal downward incidence $\theta^{-}=-\frac{\pi}{2}$, there are $p_{-1}^{Y-}=-1$ and $p_0^{d-}=1$. Then the matrix solution of scattering amplitudes further reduces to:

$$\begin{bmatrix} a_{-1}^{Y\pm}\cdot e^{i(-1)\left(\frac{\pi}{2}-\theta^{\pm}\right)} \\ a_0^{d\pm}\cdot e^{i\cdot 0\cdot\left(\frac{\pi}{2}-\theta^{\pm}\right)} \end{bmatrix}=\frac{\begin{bmatrix} b_{-1}^{Y}\left(1-b_0^{d}\cdot LS\right) & b_0^{d}\left(b_{-1}^{Y}\cdot\xi_{-1,0}^{Yd\pm}\right) \\ b_{-1}^{Y}\left(b_0^{d}\cdot\xi_{0,-1}^{dY\pm}\right) & b_0^{d}\left(1-b_{-1}^{Y}\cdot LS\right) \end{bmatrix}}{\left(1-b_{-1}^{Y}\cdot LS\right)\left(1-b_0^{d}\cdot LS\right)-\left(b_{-1}^{Y}\cdot\xi_{-1,0}^{Yd\pm}\right)\left(b_0^{d}\cdot\xi_{0,-1}^{dY\pm}\right)}\cdot\begin{bmatrix}\pm 1\\ 1\end{bmatrix},$$

where under normal incidences there is $k_x=0$, so $LS=2\sum_{l=1}^{\infty}H_0^{(1)}(k^0lh)$; the relative lattice sums are $\xi_{-1,0}^{Yd\pm}=\sum_{l=-\infty}^{\infty}H_1^{(1)}(k^0|lh\hat{x}+\overrightarrow{r_{dY}}|)\,e^{i\cdot\arg(lh\hat{x}+\overrightarrow{r_{dY}})}$, and $\xi_{0,-1}^{dY\pm}=$

$\sum_{l=-\infty}^{\infty} H_{-1}^{(1)}(k^0|lh\hat{x}+\overrightarrow{r_{Yd}}|)\, e^{-i\cdot\arg(lh\hat{x}+\overrightarrow{r_{Yd}})}$ according to the equivalent form of ξ based on the addition theorem as discussed in Chapter 2, so relative lattice sums can be unified as $\xi_{-1,0}^{Yd\pm} = \xi_{0,-1}^{dY\pm} = \xi$. Therefore, the analytical solution of $a_{-1}^{Y\pm}$ under dominant harmonic approximation is:

$$a_{-1}^{Y\pm}\cdot\pm1 = \frac{\pm b_{-1}^{Y}(1-b_0^d\cdot LS)+b_0^d(b_{-1}^{Y}\cdot\xi)}{(1-b_{-1}^{Y}\cdot LS)(1-b_0^d\cdot LS)-b_{-1}^{Y}b_0^d\cdot\xi^2}.$$

And the analytical solution of $a_0^{d\pm}$ under dominant harmonic approximation is:

$$a_0^{d\pm} = \frac{\pm b_{-1}^{Y}(b_0^d\cdot\xi)+b_0^d(1-b_{-1}^{Y}\cdot LS)}{(1-b_{-1}^{Y}\cdot LS)(1-b_0^d\cdot LS)-b_{-1}^{Y}b_0^d\cdot\xi^2}.$$

Since $a_{-1}^{Y\pm}$ and $a_0^{d\pm}$ are only determined by b_{-1}^{Y}, b_0^d, LS, and ξ, the dependences of $a_{-1}^{Y\pm}$ and $a_0^{d\pm}$ on frequency f are only determined by the dependences of b_{-1}^{Y}, b_0^d, LS, and ξ on f. Comparing these dependences, it can be observed that around 3.8 GHz where $S^{\pm}$ appears, only b_{-1}^{Y} changes rapidly with frequency (Figure 2.2(c)) due to its resonance, while other 3 variables are nearly constant within the small frequency range (Figure 3.8).

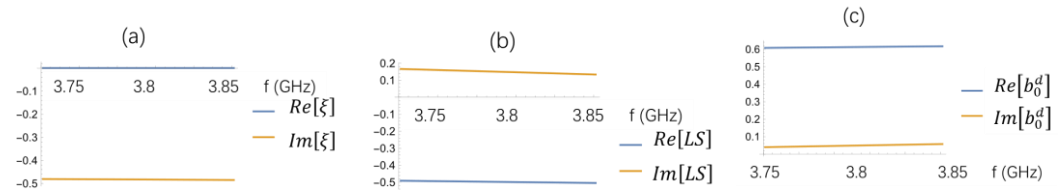

Figure 3.8. The change of (a) ξ, (b) LS, and (c) b_0^d with frequency.

Therefore, other variables have ignorable changes and can be regarded as constants, and b_{-1}^{Y} is the variable dominating the change of $a_{-1}^{Y\pm}$, $a_0^{d\pm}$, and $t^{\pm}$ as frequency changes. To better illustrate the effect of b_{-1}^{Y}, $a_{-1}^{Y\pm}$ and $a_0^{d\pm}$ can be rewritten as the form where b_{-1}^{Y} is separated from other variables:

$$a_{-1}^{Y\pm}(f)\cdot\pm1 = \frac{b_{-1}^{Y}\frac{\left(\mp b_0^d\cdot LS+b_0^d\cdot\xi\pm1\right)}{\left(b_0^d\cdot LS^2-b_0^d\cdot\xi^2-LS\right)}}{b_{-1}^{Y}+\frac{1-b_0^d\cdot LS}{\left(b_0^d\cdot LS^2-b_0^d\cdot\xi^2-LS\right)}} = \frac{b_{-1}^{Y}(f)\cdot B^{\pm}}{b_{-1}^{Y}(f)+A},$$

$$a_0^{d\pm}(f) = \frac{b_{-1}^{Y}\frac{\left(\pm b_0^d\cdot\xi-b_0^d\cdot LS\right)}{\left(b_0^d\cdot LS^2-b_0^d\cdot\xi^2-LS\right)}+\frac{b_0^d}{\left(b_0^d\cdot LS^2-b_0^d\cdot\xi^2-LS\right)}}{b_{-1}^{Y}+\frac{1-b_0^d\cdot LS}{\left(b_0^d\cdot LS^2-b_0^d\cdot\xi^2-LS\right)}} = \frac{b_{-1}^{Y}(f)\cdot C^{\pm}+D}{b_{-1}^{Y}(f)+A},$$

where A, B, C, D can be regarded as dimensionless constants.

The coupling effect

Recall that the response matrix of the non-Hermitian system relating input and output is:

$$\begin{bmatrix} a_{-1}^{Y\pm}\cdot\pm1 \\ a_0^{d\pm} \end{bmatrix} = \frac{\begin{bmatrix} b_{-1}^{Y}(1-b_0^d\cdot LS) & b_0^d(b_{-1}^{Y}\cdot\xi) \\ b_{-1}^{Y}(b_0^d\cdot\xi) & b_0^d(1-b_{-1}^{Y}\cdot LS) \end{bmatrix}}{(1-b_{-1}^{Y}\cdot LS)(1-b_0^d\cdot LS)-b_{-1}^{Y}b_0^d\cdot\xi^2}\begin{bmatrix}\pm1\\1\end{bmatrix}.$$

For the 2-by-2 matrix, there are two eigenmodes, one is loss-dominant, another is transmission dominant (because $r^{\pm}$ is reciprocal) [65], relating the scattering amplitudes of single dielectric array and YIG array. When two arrays merge, these two modes are linearly superposed and the scattering behaviours of two arrays mutually affect each other [65], resulting in the change of $a_{-1}^{Y\pm}$ and $a_0^{d\pm}$ (Figure 3.5 and 3.7). As a qualitative understanding, the response matrix is symmetric, which means the effect of incidence faced by YIG on a_0^d is equal to the effect of incidence faced by dielectric on a_{-1}^{Y}. When the coupling is strong (or weak), the excitation of the absorption loss in dielectric cylinder is strong (or weak), resulting in the loss-dominant mode (or transmission-dominant mode) and the downward peak (or upward peak) in a_0^d.

The coupling effect can be quantified by the difference between the scattering amplitudes in single array and the scattering amplitudes in hybrid array. In matrix multiplication, $a_{-1}^{Y\pm}$ of single YIG array and $a_0^{d\pm}$ of single dielectric array can be obtained by setting $b_0^d=0$ and $b_{-1}^{Y}=0$ respectively:

$$a_{-1}^{Y\pm}(Y\ array)\cdot\pm1 = \frac{\pm b_{-1}^{Y}}{1-b_{-1}^{Y}\cdot LS},$$

$$a_0^d(d\ array) = \frac{b_0^d}{1-b_0^d\cdot LS}.$$

So the changes of scattering amplitudes due to coupling are:

$$\Delta\left(a_{-1}^{Y\pm}\cdot\pm1\right) = a_{-1}^{Y\pm}\cdot\pm1 - a_{-1}^{Y\pm}(Y\ array)\cdot\pm1$$

$$= \frac{(b_{-1}^{Y})^2[\pm b_0^d\cdot\xi^2-b_0^d\xi\cdot LS]+b_{-1}^{Y}b_0^d\cdot\xi}{(b_{-1}^{Y})^2[LS^2+b_0^d\cdot LS(\xi^2-LS^2)]-b_{-1}^{Y}[2LS+b_0^d\cdot(\xi^2-2LS^2)]+(1-b_0^d\cdot LS)},$$

$$\Delta a_0^{d\pm} = a_0^{d\pm} - a_0^d(d\ array)$$

$$= \frac{b_{-1}^{Y}(f)\cdot\frac{\left[\pm b_0^d\cdot\xi\left(1-b_0^d\cdot LS\right)+{b_0^d}^2\cdot\xi^2\right]}{\left(b_0^d\cdot LS^2-b_0^d\cdot\xi^2-LS\right)\left(1-b_0^d\cdot LS\right)}}{b_{-1}^{Y}(f)+\frac{\left(1-b_0^d\cdot LS\right)^2}{\left(b_0^d\cdot LS^2-b_0^d\cdot\xi^2-LS\right)\left(1-b_0^d\cdot LS\right)}} = \frac{{B'}^{\pm}\cdot b_{-1}^{Y}(f)}{b_{-1}^{Y}(f)+A'},$$

where A' and B' can be regarded as dimensionless constants. $\Delta a_0^{d\pm}$ shares a similar form to $a_{-1}^{Y\pm}$. Recall that $b_{-1}^{Y}=\frac{-1}{1+\Omega_{-1}^{Y}}$, then $\Delta a_0^{d\pm}$ can be also written in form of Ω_{-1}^{Y} as:

$$\Delta a_0^{d\pm} = \frac{-B'^{\pm}}{(A'-1)+i\cdot\Omega_{-1}^{Y}},$$

which shares the similar form to b_{-1}^{Y}, where the difference is A' and B' are in general complex. This explains the emergence of triggered peaks in Figure 3.5 (d) and (f).

Recall that Ω_{-1}^{Y} is real (Figure 2.2(d)), we can consider the difference between absolute values of $a_0^{d\pm}$ and $a_0^{d}(d\ array)$ and its derivative to f, to explain the antisymmetric pattern of triggered peaks in Figure 3.5 (d) and (f):

$$\Delta\left|a_0^{d\pm}\right| = \left|a_0^{d\pm}\right| - \left|a_0^{d}(d\ array)\right| = \sqrt{\frac{\left(-C_R^{\pm}+D_R-\Omega_{-1}^{Y}\cdot D_I\right)^2+\left(-C_I^{\pm}+D_I+\Omega_{-1}^{Y}\cdot D_R\right)^2}{\left(-1+A_R-\Omega_{-1}^{Y}\cdot A_I\right)^2+\left(A_I+\Omega_{-1}^{Y}\cdot A_R\right)^2}} - \left|\frac{b_0^{d}}{1-b_0^{d}\cdot LS}\right|,$$

where the subscript R and I represent the real part and the imaginary part. Since other variables except for Ω_{-1}^{Y} can be regarded as constants, the derivative of $\Delta\left|a_0^{d\pm}\right|$ to f can be written as:

$$\frac{\partial}{\partial f}\Delta\left|a_0^{d\pm}\right| = \frac{\partial}{\partial\Omega_{-1}^{Y}}\sqrt{\frac{\left(-C_R^{\pm}+D_R-\Omega_{-1}^{Y}\cdot D_I\right)^2+\left(-C_I^{\pm}+D_I+\Omega_{-1}^{Y}\cdot D_R\right)^2}{\left(-1+A_R-\Omega_{-1}^{Y}\cdot A_I\right)^2+\left(A_I+\Omega_{-1}^{Y}\cdot A_R\right)^2}}\cdot\frac{d\Omega_{-1}^{Y}}{df},$$

where the second multiplier $\frac{d\Omega_{-1}^{Y}}{df}$ is nearly a negative constant (Figure 2.2(d)), and the first multiplier takes zero value before and after the frequency 3.8 GHz where $\Omega_{-1}^{Y}=0$. This explains that the triggered peaks in $a_0^{d\pm}$ are antisymmetric before and after the YIG resonant frequency. The $C_R^{\pm}$ and $C_I^{\pm}$ result in opposite values of derivative, which leads to the upside-down inversed pattern of triggered peaks in $a_0^{d\pm}$ under opposite incidences.

We could also consider the derivative of $\Delta a_0^{d\pm}(f)$ to f:

$$\frac{\partial}{\partial f}\Delta a_0^{d\pm}(f) = \frac{A'\cdot B'^{\pm}}{[b_{-1}^{Y}(f)+A']^2}\cdot\frac{db_{-1}^{Y}(f)}{df},$$

where the operation requires the analyticity of complex function $\Delta a_0^{d\pm}$ with respect to variable b_{-1}^{Y}. The nearly antisymmetric pattern of peaks and valleys of $a_0^{d\pm}$ is a consequence of the symmetric norm but antisymmetric argument of $b_{-1}^{Y}(f)$ before and after 3.8 GHz (Figure 2.2(c)).

3.4.1.2 The dependence of transmission coefficients on frequency

Under normal incidence, $\overrightarrow{k^i}$ is perpendicular to $\overrightarrow{r_{Yd}}$, so the transmission coefficients $t^{\pm}$ reduce to a simple form:

$$t^{\pm} = 1 + \frac{2}{hk_y}\left(a_{-1}^{Y\pm} + a_0^{d\pm}\right).$$

Therefore, $t^{\pm} = 0$ requires $\left(a_{-1}^{Y\pm} + a_0^{d\pm}\right) = -\frac{hk_y}{2}$, where $k_y = k^0 = 2\pi f\sqrt{\mu_0\varepsilon_0} \times 10^9$. For a qualitative understanding, the $t^{\pm} = 0$ cases correspond to the destructive interference between the incident field, scattering from YIG, and scattering from dielectric. The criteria of $t^{\pm} = 0$ can be understood as the match of coupled $a_{-1}^{Y\pm}$ and $a_0^{d\pm}$. Since the value of coupled $a_{-1}^{Y\pm}$ has a continuous coverage from -1.5 to 1.5 (Figure 3.7), and the coupled $a_0^{d\pm}$ (Figure 3.5 (d)(f)) has a larger range compared to $a_0^d(d\ array)$ due to the triggered peaks, the destructive interference $\left(a_{-1}^{Y\pm} + a_0^{d\pm}\right) = -\frac{hk_y}{2}$ is more likely to happen around the triggered peaks of $a_0^{d\pm}$ where the coupling effect on dielectric is extreme enough. The coexistence of zero norm and singular phase and the surrounding vortex field of $S^{\pm}$ can be easily understood by the match of continuous real and imaginary parts of a_{-1}^{Y} and a_0^d at $\left(a_{-1}^{Y\pm} + a_0^{d\pm}\right) = -\frac{hk_y}{2}$. The coupling effect partially provides the condition of $t^{\pm} = 0$, and the rest condition is completed by another parameter ϵ_{Im}, which will be discussed later.

In the form of Mie coefficients and lattice sums, $t^{\pm}$ can be written as:

$$t^{\pm} = 1 + \frac{2}{hk_y}\frac{b_{-1}^{Y} + b_0^d - 2b_{-1}^{Y}b_0^d\cdot(LS\mp\xi)}{(1-b_{-1}^{Y}\cdot LS)(1-b_0^d\cdot LS) - b_{-1}^{Y}b_0^d\cdot\xi^2},$$

where b_{-1}^{Y} and b_0^d are exchangeable. The coupling effect from YIG to dielectric partially cancels the coupling effect from dielectric to YIG in the summation of $a_{-1}^{Y\pm}$ and $a_0^{d\pm}$. To better illustrate the effect of frequency, transmission coefficients can be rewritten as the form where b_{-1}^{Y} is separated from other variables:

$$t^{\pm} = 1 + \frac{2}{hk_y}\frac{b_{-1}^{Y}\left[1-2b_0^d\cdot(LS\mp\xi)\right] + b_0^d}{b_{-1}^{Y}(b_0^d\cdot LS^2 - b_0^d\cdot\xi^2 - LS) + 1 - b_0^d\cdot LS},$$

from which $t^{\pm} = 0$ requires $b_{-1}^{Y} = \frac{-hk_y(1-b_0^d\cdot LS) - 2b_0^d}{hk_y(b_0^d\cdot LS^2 - b_0^d\cdot\xi^2 - LS) + 2\left[1-2b_0^d\cdot(LS\mp\xi)\right]}$. $t^{\pm}$ can also be written in the form of Ω_{-1}^{Y} as:

$$t^{\pm} = 1 + \frac{2}{hk_y}\frac{i\cdot\Omega_{-1}^{Y}b_0^d + b_0^d - \left[1-2b_0^d\cdot(LS\mp\xi)\right]}{i\cdot\Omega_{-1}^{Y}(1-b_0^d\cdot LS) + (1-b_0^d\cdot LS) - (b_0^d\cdot LS^2 - b_0^d\cdot\xi^2 - LS)},$$

from which $t^{\pm} = 0$ requires:

$$\Omega_{-1}^{Y} = i\frac{k_y\frac{\left[(1-b_0^d\cdot LS) - (b_0^d\cdot LS^2 - b_0^d\cdot\xi^2 - LS)\right]}{(1-b_0^d\cdot LS)} + \frac{2b_0^d - 2\left[1-2b_0^d\cdot(LS\mp\xi)\right]}{h(1-b_0^d\cdot LS)}}{k_y + \frac{2b_0^d}{h(1-b_0^d\cdot LS)}} = i\frac{B''\cdot k_y(f) + C''^{\pm}}{k_y(f) + A''},$$

where A'', B'', and $C''^{\pm}$ are constants. Two real quantities $k_y = 2\pi f\sqrt{\mu_0\varepsilon_0} \times 10^9$ and Ω_{-1}^Y apparently changes with frequency. Their gradients are $\frac{dk_y}{df} \approx 20$ and $\frac{d\Omega_{-1}^Y}{df}$ is nearly a negative constant. With other quantities nearly invariant to f, the event of $t^{\pm} = 0$ happens at intersection of the monotonically decreasing curve of $\Omega_{-1}^Y(f)$ and the curve of $i\frac{B''\cdot k_y(f)+C''^{\pm}}{k_y(f)+A''}$, which shares a similar form to $\left|a_0^{d\pm}\right|(\Omega_{-1}^Y)$. According to Figure 3.2(b), under upward incidence, one intersection happens at $\Omega_{-1}^Y > 0$ before 3.8 GHz; under downward incidence, one intersection happens at $\Omega_{-1}^Y < 0$ after 3.8 GHz. This results in a pair of opposite singularities S^- and S^+ before and after b_{-1}^Y's resonance peak. And the opposite winding numbers of S^- and S^+ are mainly determined by the derivatives of the real and imaginary parts of $t^{\pm}$ to f, which are $\frac{\partial Re[t^{\pm}]}{\partial f} = \frac{\partial Re[t^{\pm}]}{\partial \Omega_{-1}^Y} \cdot \frac{d\Omega_{-1}^Y}{df}$ and $\frac{\partial Im[t^{\pm}]}{\partial f} = \frac{\partial Im[t^{\pm}]}{\partial \Omega_{-1}^Y} \cdot \frac{d\Omega_{-1}^Y}{df}$. The effect of ϵ_{Im} on the real and imaginary parts of $t^{\pm}$ is relatively negligible, which will be discussed soon.

3.4.2 Effect of loss and radius of dielectric cylinder

Since the transmission singularity pair $S^{\pm}$ appears in $f - \epsilon_{Im}$ parameter space and is robust against the fluctuation of r_d, it's necessary to investigate the effect of dielectric absorption ϵ_{Im} and dielectric cylinder radius r_d on transmission coefficients. The adjustment of r_d and ϵ_{Im} have effect only on b_0^d, therefore, b_{-1}^Y, ξ, and LS are constants. To reveal the effect of ϵ_{Im} and r_d on $t^{\pm}$ through b_0^d, $t^{\pm}$ can be written in the form where b_0^d is separated from other variables:

$$t^{\pm} = 1 + \frac{2}{hk_y}\frac{b_0^d[1-2\cdot b_{-1}^Y(LS\mp\xi)]+b_{-1}^Y}{b_0^d[b_{-1}^Y(LS^2-\xi^2)-LS]+1-b_{-1}^Y\cdot LS},$$

from which $t^{\pm} = 0$ requires $b_0^d = \frac{-hk_y(1-b_{-1}^Y\cdot LS)-2b_{-1}^Y}{hk_y(b_{-1}^Y\cdot LS^2-b_{-1}^Y\cdot\xi^2-LS)+2[1-2b_{-1}^Y\cdot(LS\mp\xi)]}$. According to Figure 2.2(a)(b), the loss ϵ_{Im} will decrease the norm and alter the argument of b_0^d. A more comprehensive illustration of b_0^d's dependence on r_d and ϵ_{Im} is in Figure 3.9(a), which is not as rapid as b_{-1}^Y's change with frequency.

At the same time, Figure 3.9(b) shows that the dependence of $\left(a_{-1}^{Y\pm} + a_0^{d\pm}\right)$ on ϵ_{Im} is monotonically increasing or decreasing. This monotonicity guarantees the generation of singularities, where $\left(a_{-1}^{Y\pm} + a_0^{d\pm}\right)$ can always find an intersection with $-\frac{hk_y}{2}$ within a range

of ϵ_{Im}, despite the value of $\left(a_{-1}^{Y\pm}+a_0^{d\pm}\right)$ varies with frequency. This intersection results in $t^{\pm}=0$. Therefore, the emergence of singularity pair in $f-\epsilon_{Im}$ plane results from a combination of coupling effect and monotonicity. Moreover, the monotonicity of the real and imaginary parts of $\left(a_{-1}^{Y\pm}+a_0^{d\pm}\right)$ guarantees the flat change of $t^{\pm}$'s argument around singularities, resulting in the topological robustness and well-defined winding numbers of $S^{\pm}$.

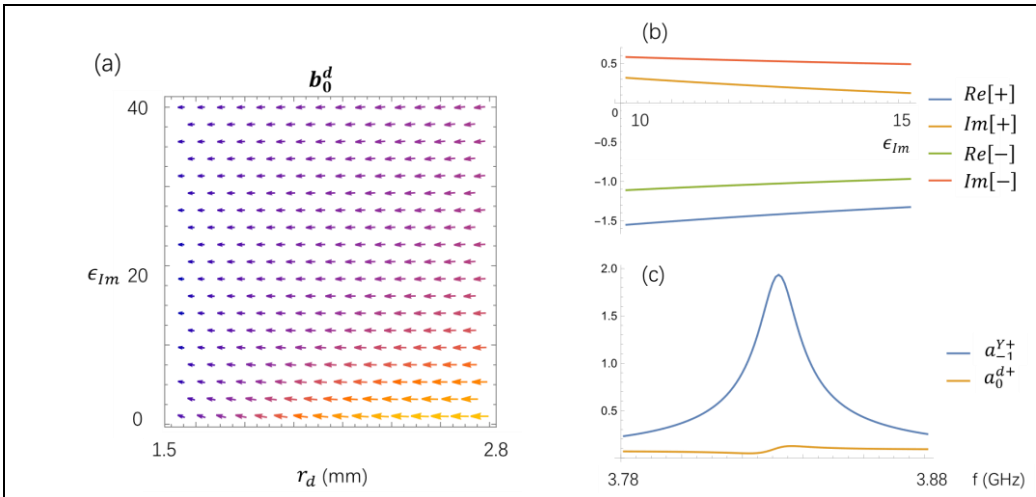

Figure 3.9. (a) The dependence of b_0^d on r_d and ϵ_{Im}. $ndi=(23.04+\epsilon_{Im}\times i)^{\frac{1}{2}}$, $f=3.8\,GHz$, $H_0=500\,Oe$. (b) The changes of real and imaginary parts of $\left(a_{-1}^{Y\pm}+a_0^{d\pm}\right)$ or equivalently $\frac{b_0^d[1-2\cdot b_{-1}^Y(LS\mp\xi)]+b_{-1}^Y}{b_0^d[b_{-1}^Y(LS^2-\xi^2)-LS]+1-b_{-1}^Y\cdot LS}$, as ϵ_{Im} changes. (c) Absolute values of a_{-1}^{Y+} and a_0^{d+}, frequency 3.78 to 3.88 GHz, at extremely large loss and small r_d.

According to Figure 3.3(a), as r_d decreases, S^- and S^+ get closer at larger loss. The merge of two singularities requires $a_0^{d\pm}$ to coincide with $a_{-1}^{Y\pm}$ at the resonance peak, otherwise the singularities are separated by resonance peak and have opposite winding numbers. However, increase of loss results in decrease of $a_0^{d\pm}$ (Figure 2.2(a)(b)), thus the weakening of the coupling effect and the reduction of a_0^d's triggered peaks (Figure 3.9(c)); at the same time, the resonance peak of a_{-1}^Y is stronger due to the reduced coupling. The sharp resonance peak can effectively separate S^- and S^+ even when they are very close at small $a_0^{d\pm}$. Therefore, merge of $S^{\pm}$ is almost impossible at normal incidence. The adjustment of h, $\overrightarrow{r_{Yd}}$, or θ may enable the merge, where the geometric symmetry is broken and the number of degrees of freedom increases.

3.4.3 Effect of incidence angle

Since the transmission singularity pair $S^{\pm}$ also vaguely appears in $f-\theta$ parameter space, and new pairs of $S_{\pm}^{\theta 1}$ and $S_{\pm}^{\theta 2}$ emerge at oblique incidence, it's worth investigating the effect of incidence angle θ, despite the analysis under oblique incidence is more complicated. Since b_{-1}^{Y} and b_0^d are independent of θ, the effect of θ on scattering amplitudes is only included in $\overrightarrow{p^{in}}$, LS, and ξ. The phase of $\overrightarrow{k^{i}}$ changes with θ; LS and ξ changes with k_x. Under oblique incidence $\xi_{-1,0}^{Yd}=\xi_{0,-1}^{dY}$, but $\xi^{+}\neq\xi^{-}$ due to the dependence of relative lattice sums on k_x. Relative lattice sums can be written as $\xi_{-1,0}^{Yd\pm}=\xi_{0,-1}^{dY\pm}=\xi e^{i(\pm k_x\cdot Con)}$, where Con is a constant with respect to θ. The scattering amplitudes are:

$$\begin{bmatrix} a_{-1}^{Y\pm}\cdot e^{i\left(\theta^{\pm}-\frac{\pi}{2}\right)} \\ a_0^{d\pm} \end{bmatrix}=\frac{\begin{bmatrix} b_{-1}^{Y}(1-b_0^d\cdot LS) & b_0^d\left(b_{-1}^{Y}\cdot\xi_{-1,0}^{Yd\pm}\right) \\ b_{-1}^{Y}\left(b_0^d\cdot\xi_{0,-1}^{dY\pm}\right) & b_0^d(1-b_{-1}^{Y}\cdot LS) \end{bmatrix}}{(1-b_{-1}^{Y}\cdot LS)(1-b_0^d\cdot LS)-b_{-1}^{Y}b_0^d\cdot\xi_{-1,0}^{Yd\pm}\xi_{0,-1}^{dY\pm}}\cdot\begin{bmatrix} p_{-1}^{Y\pm} \\ p_0^{d\pm} \end{bmatrix},$$

where $p_{-1}^{Y\pm}=e^{i\left(\theta^{\pm}-\frac{\pi}{2}\right)}\cdot e^{ik^0\cdot\frac{dx}{2}\cos\theta^{\pm}}$ and $p_0^{d\pm}=e^{ik^0\cdot\frac{dx}{2}\cos(\theta^{\pm}-\pi)}$, $\theta^{-}=\theta^{+}-\pi$. And $t^{\pm}$ is:

$$t^{\pm}=1+\frac{2}{hk^0\cdot\sin\theta^{+}}\left[a_{-1}^{Y\pm}\cdot e^{ik^0\cdot\frac{dx}{2}\cos(\theta^{\pm}-\pi)}+a_0^{d\pm}\cdot e^{ik^0\cdot\frac{dx}{2}\cos\theta^{\pm}}\right].$$

According to the matrix solution of scattering amplitudes, there is:

$$a_{-1}^{Y\pm}\cdot e^{ik^0\cdot\frac{dx}{2}\cos(\theta^{\pm}-\pi)}=\frac{b_{-1}^{Y}(1-b_0^d\cdot LS)+b_0^d\left(b_{-1}^{Y}\cdot\xi_{-1,0}^{Yd\pm}\right)e^{i\left(\frac{\pi}{2}-\theta^{\pm}\right)}e^{ik^0\cdot dx\cdot\cos\left(\theta^{\pm}-\pi\right)}}{(1-b_{-1}^{Y}\cdot LS)(1-b_0^d\cdot LS)-b_{-1}^{Y}b_0^d\cdot\xi_{-1,0}^{Yd\pm}\xi_{0,-1}^{dY\pm}},$$

$$a_0^{d\pm}\cdot e^{ik^0\cdot\frac{dx}{2}\cos\theta^{\pm}}=\frac{b_{-1}^{Y}\left(b_0^d\cdot\xi_{0,-1}^{dY\pm}\right)e^{i\left(\theta^{\pm}-\frac{\pi}{2}+k^0\cdot dx\cdot\cos\theta^{\pm}\right)}+b_0^d(1-b_{-1}^{Y}\cdot LS)}{(1-b_{-1}^{Y}\cdot LS)(1-b_0^d\cdot LS)-b_{-1}^{Y}b_0^d\cdot\xi_{-1,0}^{Yd\pm}\xi_{0,-1}^{dY\pm}},$$

of which the summation $sa^{\pm}$ is:

$$sa^{\pm}=a_{-1}^{Y\pm}\cdot e^{ik^0\cdot\frac{dx}{2}\cos(\theta^{\pm}-\pi)}+a_0^{d\pm}\cdot e^{ik^0\cdot\frac{dx}{2}\cos\theta^{\pm}}=$$

$$\frac{b_{-1}^{Y}(1-b_0^d\cdot LS)+b_0^d(1-b_{-1}^{Y}\cdot LS)+b_0^d b_{-1}^{Y}\cdot\xi_{-1,0}^{Yd\pm}e^{i\left(\frac{\pi}{2}-\theta^{\pm}\right)}e^{-i\alpha^{\pm}}+b_{-1}^{Y}b_0^d\cdot\xi_{0,-1}^{dY\pm}e^{i\left(\theta^{\pm}-\frac{\pi}{2}\right)}e^{i\alpha^{\pm}}}{(1-b_{-1}^{Y}\cdot LS)(1-b_0^d\cdot LS)-b_{-1}^{Y}b_0^d\cdot\xi_{-1,0}^{Yd\pm}\xi_{0,-1}^{dY\pm}},$$

where $\alpha^{\pm}=k^0\cdot dx\cdot\cos\theta^{\pm}$. Since $\theta^{-}=\theta^{+}-\pi$, there is $\alpha^{\pm}=\pm k^0\cdot dx\cdot\cos\theta^{+}$ and $\alpha^{-}=-\alpha^{+}$. Then $sa^{\pm}$ can be rewritten as:

$$sa^{\pm}=\frac{b_{-1}^{Y}(1-b_0^d\cdot LS)+b_0^d(1-b_{-1}^{Y}\cdot LS)+b_0^d b_{-1}^{Y}\cdot\xi\left[e^{i\left(\pm k_x\cdot Con\pm\frac{\pi}{2}-\theta^{+}\mp\alpha^{+}\right)}+e^{i\left(\pm k_x\cdot Con+\theta^{+}\mp\frac{\pi}{2}\pm\alpha^{+}\right)}\right]}{(1-b_{-1}^{Y}\cdot LS)(1-b_0^d\cdot LS)-b_{-1}^{Y}b_0^d\cdot\xi e^{i(\pm 2k_x\cdot Con)}}.$$

The transmission coefficient is $t^{\pm}=1+\frac{2sa^{\pm}}{hk^0\cdot\sin\theta^{+}}$. For two angles θ_1 and θ_2 satisfying $\frac{\pi}{2}-$

$\theta_1 = \theta_2 - \frac{\pi}{2}$, the dependence of k_x and α^+ on angle θ^+ ensures the equivalence that $sa^{\pm}(when\ \theta^+ = \theta_1) = sa^{\pm}(when\ \theta^+ = \theta_2)$. Combing with the fact that $\sin\theta_1 = \sin\theta_2$, it explains that $t^{\pm}(when\ \theta^+ = \theta_1) = t^{\pm}(when\ \theta^+ = \theta_2)$, which is the parity symmetry of transmission coefficient. This explains the simultaneous emergence of $S^{\theta 1}$ and $S^{\theta 2}$.

$t^{\pm} = 0$ requires $sa^{\pm} = -\frac{hk^0 \cdot \sin\theta^+}{2}$. The combination of the expression of $sa^{\pm}$ and the dependence of $t^{\pm}$ on f theoretically could explain: 1. why opposite singularities S_+^{θ} and S_-^{θ} in one pair in t^+ and t^- functions emerge at the same position in $f - \theta$ parameter space; 2. Why the winding numbers of S_+^{θ} and S_-^{θ} are the same. The mechanism could explain the emergence of $S_{\pm}^{\theta 1}$ and $S_{\pm}^{\theta 2}$ in Figure 3.4 and their annihilation in CIR.

The numerical results in Figure 3.10 show the dependence of $t^{\pm}$ on θ, which satisfies the parity symmetry deduced from the above expression. Within the range where only 0th transmission channel opens, the effect of θ is not as strong as the dependence on frequency. Due to the symmetric pattern with respect to $\theta = 0$, the effect of θ on $t^{\pm}$ isn't monotonic at around normal incidence, therefore, the existence of S^+ in Figure 3.4(c) is vague and the robustness of $S^{\pm}$ in $f - \theta$ parameter space isn't strong. In Figure 3.10 at around $cos\theta = \pm\frac{11}{19}$, the $t^{\pm}$ abruptly change with θ, which may result from the opening of ± 1 transmission and reflection channels when $-1 < cos\theta < -\frac{11}{19}$ and $\frac{11}{19} < cos\theta < 1$ at around 3.8GHz, according to Section 2.2.2.

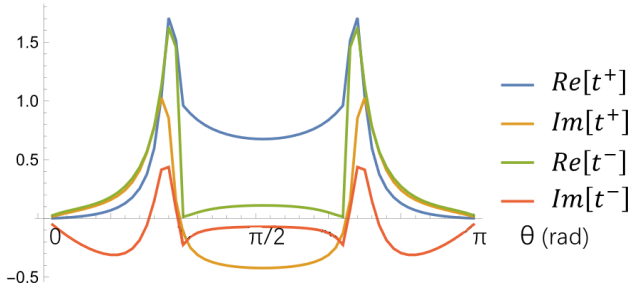

Figure 3.10. Real and imaginary parts of $t^{\pm}$, at $r_d = 2.5\,mm, ndi = (23.04 + 12 \times i)^{\frac{1}{2}}, f = 3.815\,GHz$. This is a cross-sectional view of Figure 3.4(b) and (c) at $f = 3.815\,GHz$.

3.4.4 The robustness of singularity pair

As discussed in Section 3.4.1 and 3.4.2, the robustness of $S^{\pm}$ in the frequency spectrum is protected by the strong resonance of YIG and the coupling effect between YIG array and dielectric array. As the b_{-1}^{Y} continuously covers a large range of value within narrow frequency range, which triggers a large continuous range of $a_{-1}^{Y\pm}$, $a_{0}^{d\pm}$, and $t^{\pm}$, one special value satisfying the zero transmission criteria can always be found within the range. The effect of f through b_{-1}^{Y} can be equivalently replaced by the effect of f through Ω_{-1}^{Y}. In addition, b_{-1}^{Y} has almost identical zero values far-before and far-after the resonant frequency (Figure 2.2(c)), so the f-axis can be regarded to have an approximately closed boundary condition, which provides the rigorous condition for topological robustness. Moreover, compared to b_{-1}^{Y} (Figure 2.1(b)) and b_{0}^{d} (Figure 2.1(a)) of single cylinder, the scattering amplitudes $a_{-1}^{Y\pm}$ (Figure 3.5(a)) and $a_{0}^{d\pm}$ (Figure 3.5(b)) in cylinder arrays are strengthened due to the collective response from infinite cylinders. This collective response in quasi-continuous continuum is intrinsically topologic [68]. and strengthens the topological robustness of $S^{\pm}$.

Other variables such as loss, r_d, and θ have relatively small effects, thus can be regarded as small perturbations which don't determine the existence of singularities but only affect the position of singularities in parameter space. These variables within certain range of values enable the $t^{\pm}=0$ condition, which strengthens the robustness of $S^{\pm}$. The monotonicity of ϵ_{Im}-dependence is the cause of robustness in $f-\epsilon_{Im}$ plane and during evolution of r_d.

Chapter 4. Conclusion and outlook

This thesis starts from the introduction of optical control systems, topological optics, and overview of the research project in Chapter 1. In Chapter 2, the methodology of the first-principle calculation is introduced, including the Mie scattering theory of gyromagnetic and dielectric infinite-length circular cylinders (derivations in Appendix A) and multiple scattering theory which computes the scattering field of 1D-periodic array, from which the transmission and reflection coefficients are defined as functions of scattering amplitudes. Chapter 3 is about the results and discussion: Firstly, the dimer-unit model configuration is introduced; Secondly, the transmission singularity pairs and their evolution are numerically displayed; Thirdly, the dominant harmonic approximation is applied on the solution of scattering amplitudes obtained in Chapter 2, then the effects of parameters f, ϵ_{Im}, r_d, and θ on scattering amplitudes and transmission coefficients under opposite incidences are studied according to the approximated solution. The effect of parameters explains the mechanism of emergence of singularity pairs and their topological robustness, where the nonreciprocity and non-Hermiticity are necessary conditions.

The topological singularity pair $S^{\pm}$ is generated by the combination of strong magnetic response of nonreciprocal gyromagnetic medium and unequal excitation of loss in dielectric under nonreciprocal coupling [65]. This mechanism can be generalized to any periodic nonreciprocal non-Hermitian system where the control of nonreciprocity and gain/loss are separated.

There are limitations of this work. So far, the effect of geometric parameters dx, dy and h are not studied, which determine the value of LS and ξ. The study can explore new dimension in parameter space where $t^{+} = t^{-} = 0$ may be observed. Recall the research aims in Chapter 1, the first and second aims are achieved, while the third aim of combining the classical electromagnetic theory and the non-Hermitian topological optics isn't thoroughly discussed in the thesis.

To further study the non-Hermitian topological optics, I plan to test other models where the solution of scattered field obtained in Chapter 2 is applicable. Firstly, I plan to study a 1D-periodic nonreciprocal non-Hermitian PT-symmetric system, where each unit cell contains one

gyromagnetic cylinder and two dielectric cylinders with optical gain and loss (Figure 4.1). Some non-Hermitian topological phenomena such as exceptional points and non-Hermitian point gaps may be observed from its photonic band.

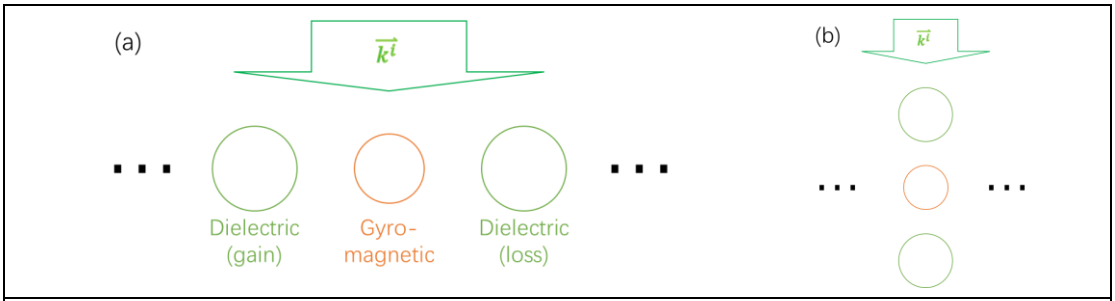

Figure 4.1. One unit cell of 1D PT-symmetric system, where the symmetry is with respect to (a) y axis and (b) x axis.

Secondly, the staking of monolayer constitutes a 2D periodic system, where it's possible to construct square lattice or honey-comb structures depending on the lattice vectors and relative location of cylinders in dimer-unit cell (Figure 4.2). For 2D periodic system, the rigorous solution obtained in Chapter 2 need to be modified, where Bloch's theorem is applicable to both x and y direction. The scattered field satisfies: $E_z^s(\vec{s}+\overrightarrow{ds}) = e^{i(\boldsymbol{k}\cdot\overrightarrow{ds})}E_z^s(\vec{s})$ with $\overrightarrow{ds} = m\overrightarrow{dx} + n\overrightarrow{dy}$, where $\overrightarrow{dx}$ and $\overrightarrow{dy}$ are lattice vectors along +x and +y directions, m and n are integers.

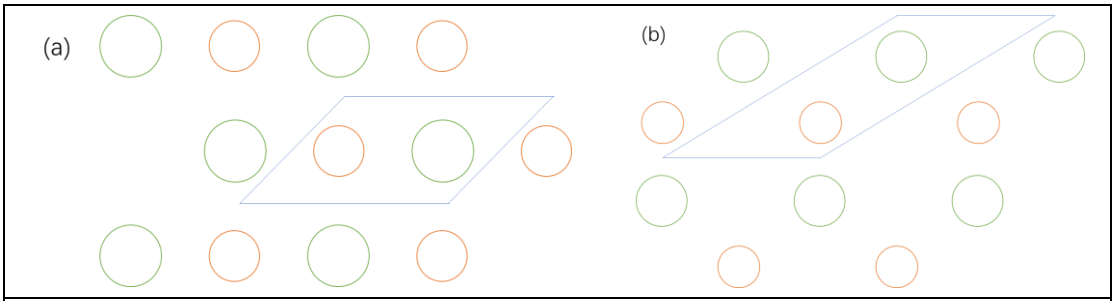

Figure 4.2. 2D (a) square lattice and (b) honey-comb structure of dimer-unit cells.

Appendix A. Derivation of Mie scattering coefficients

In this appendix, I will derive the equations of Mie scattering coefficients of infinite-length circular cylinders of dielectric and gyromagnetic materials. The Mie coefficients describe the scattering amplitudes of cylinders under normal-to-axis plane wave incidences. In the 2D scattering problem, the incident waves, scattered waves, and internal waves will be expressed in cylindrical harmonics, where the radial dependence and angular dependence of electromagnetic fields are separated. By matching boundary conditions, the ratio of scattered fields to incident fields in each harmonic order can be solved, which is defined as the Mie coefficient of each order.

A1. Wave equation in cylindrical coordinate

In vacuum devoid of charge and current source, Maxwell's equations reduce to:

$$\begin{cases} \nabla \cdot \vec{E} = 0 & \nabla \times \vec{E} = -\frac{\partial \vec{B}}{\partial t} \\ \nabla \cdot \vec{B} = 0 & \nabla \times \vec{B} = \mu_0 \varepsilon_0 \frac{\partial \vec{E}}{\partial t} \end{cases}.$$

Take the curl of the Faraday equation, and substitute into the equation of Ampere's law:

$$\nabla \times \left(\nabla \times \vec{E}\right) = \nabla \times \left(-\frac{\partial \vec{B}}{\partial t}\right) = -\frac{\partial}{\partial t}\left(\nabla \times \vec{B}\right) = -\mu_0 \varepsilon_0 \frac{\partial^2 \vec{E}}{\partial t^2}.$$

At the same time, apply the vector identity for the curl-of-curl operator [69]:

$$\nabla \times \left(\nabla \times \vec{E}\right) = \nabla\left(\nabla \cdot \vec{E}\right) - \nabla^2 \vec{E} = -\nabla^2 \vec{E}.$$

Recall that $\nabla \cdot \vec{E} = 0$ in source-free regions, the wave equation of $\vec{E}$ can be obtained from above two equations:

$$\nabla^2 \vec{E} = \mu_0 \varepsilon_0 \frac{\partial^2 \vec{E}}{\partial t^2}.$$

An analogous procedure gives the wave equation of $\vec{B}$:

$$\nabla^2 \vec{B} = \mu_0 \varepsilon_0 \frac{\partial^2 \vec{B}}{\partial t^2}.$$

Component-wise wave equation can be obtained by expressing the Laplacian operator, where for any vector field $\vec{A}$ in 3D cylindrical coordinates (s, ϕ, z) (Figure A.1(a)), the set of 3 scalar components along (s, ϕ, z) can be regarded as the set of components along (x, y, z) after a rotation around z-axis. Since 3 cylindrical components still form an orthonormal basis, the action of Laplacian operator on vector field $\vec{A}$ expands to $\nabla^2 \vec{A} = \nabla^2 A_s \cdot \hat{s} + \nabla^2 A_\phi \cdot \hat{\phi} +$

$\nabla^2 A_z \cdot \hat{z}$, which is the same as the expansion in Cartesian coordinates. Therefore, each component of $\vec{E}$ and $\vec{B}$ satisfies a scalar wave equation:

$$\begin{cases} \nabla^2 E_s = \mu_0 \varepsilon_0 \frac{\partial^2 E_s}{\partial t^2} \\ \nabla^2 E_\phi = \mu_0 \varepsilon_0 \frac{\partial^2 E_\phi}{\partial t^2} \\ \nabla^2 E_z = \mu_0 \varepsilon_0 \frac{\partial^2 E_z}{\partial t^2} \end{cases}, \quad \begin{cases} \nabla^2 B_s = \mu_0 \varepsilon_0 \frac{\partial^2 B_s}{\partial t^2} \\ \nabla^2 B_\phi = \mu_0 \varepsilon_0 \frac{\partial^2 B_\phi}{\partial t^2} \\ \nabla^2 B_z = \mu_0 \varepsilon_0 \frac{\partial^2 B_z}{\partial t^2} \end{cases},$$

where the wave velocity $c = \frac{1}{\sqrt{\mu_0 \varepsilon_0}}$ in vacuum.

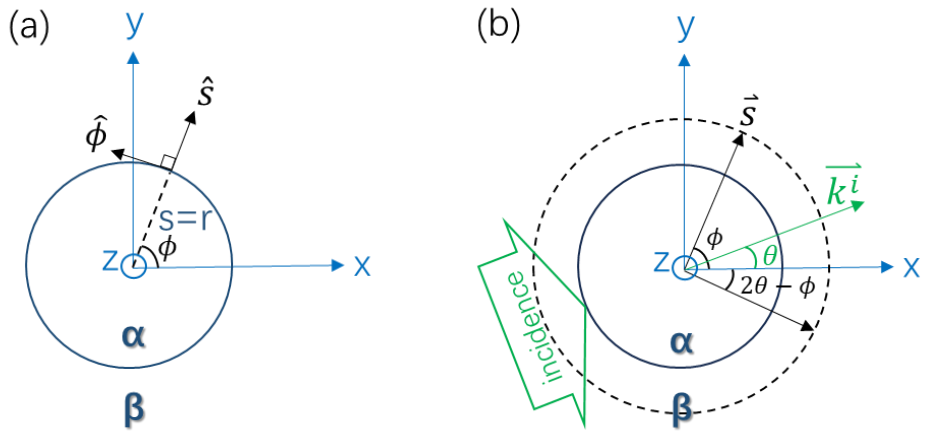

Figure A.1. (a) The cross section of cylinder in Cartesian coordinate (x, y, z) and cylindrical coordinate (s, ϕ, z). (x, y, z) coordinate is in blue, and (s, ϕ, z) coordinate is in black. Directions of $\hat{s}$ and $\hat{\phi}$ depend on ϕ. The space is divided into region α and region β by the cylinder surface at s = r, the region labels and boundary are in dark blue. (b) The plane wave incidence on the cylinder is illustrated in green. According to the parity symmetry with respect to $\vec{k^i}$, for the same s, the field at ϕ is the same as the field at θ-(ϕ-θ) = 2θ-ϕ.

Any cylindrical component f of $\vec{E}$ or $\vec{B}$ satisfies the scalar wave equation: $\nabla^2 f = \mu_0 \varepsilon_0 \frac{\partial^2 f}{\partial t^2}$. Resulting from the mutual influence of s- and ϕ- dependences of f, the divergence of gradient of the scalar field f in cylindrical coordinate yields: $\nabla^2 f = \frac{1}{s}\frac{\partial}{\partial s}(s\frac{\partial f}{\partial s}) + \frac{1}{s^2}\frac{\partial^2 f}{\partial \phi^2} + \frac{\partial^2 f}{\partial z^2}$, then the cylindrical scalar wave equation becomes:

$$\mu_0 \varepsilon_0 \frac{\partial^2 f}{\partial t^2} = \frac{1}{s}\frac{\partial}{\partial s}(s\frac{\partial f}{\partial s}) + \frac{1}{s^2}\frac{\partial^2 f}{\partial \phi^2} + \frac{\partial^2 f}{\partial z^2}.$$

A2. Separation of variables

f is a function of variables s, ϕ, z, and t. The method of separation of variables can be employed: assume f can be decomposed into a product of functions dependent on individual space and time variables: $f = \mathrm{P}(s) \cdot \Phi(\phi) \cdot \mathrm{Z}(z) \cdot T(t)$, substituting which into the wave equation gives:

$$\mu_0 \varepsilon_0 \mathrm{P}\Phi\mathrm{Z}\frac{d^2T}{dt^2} = \frac{1}{s}\frac{\partial}{\partial s}\left(s\Phi\mathrm{Z}T\frac{d\mathrm{P}}{ds}\right) + \frac{1}{s^2}\mathrm{P}\mathrm{Z}T\frac{d^2\Phi}{d\phi^2} + \mathrm{P}\Phi\mathrm{T}\frac{d^2\mathrm{Z}}{dz^2}.$$

Divide both sides by $\mathrm{P}\Phi\mathrm{Z}T$:

$$\mu_0 \varepsilon_0 \frac{1}{T}\frac{d^2T}{dt^2} = \frac{1}{s}\frac{1}{\mathrm{P}}\frac{d}{ds}\left(s\frac{d\mathrm{P}}{ds}\right) + \frac{1}{s^2}\frac{1}{\Phi}\frac{d^2\Phi}{d\phi^2} + \frac{1}{\mathrm{Z}}\frac{d^2\mathrm{Z}}{dz^2}.$$

For a z-invariant cylinder under plane wave incidence normal to axial z-axis, the incident field, scattered field, and total field are z-independent ($\mathrm{Z}(z) = 1$) [56, 64]. With the time-harmonic convention $T(t) = e^{-i\omega t}$, the above equation reduces to:

$$-\omega^2\mu_0\varepsilon_0 = \frac{1}{s}\frac{1}{\mathrm{P}}\frac{d\mathrm{P}}{ds} + \frac{1}{\mathrm{P}}\frac{d^2\mathrm{P}}{ds^2} + \frac{1}{s^2}\frac{1}{\Phi}\frac{d^2\Phi}{d\phi^2}.$$

Introducing the angular wave number $k \equiv \frac{\omega}{v} = \omega\sqrt{\mu_0\varepsilon_0}$, the above equation becomes:

$$s\frac{1}{\mathrm{P}}\frac{d\mathrm{P}}{ds} + s^2\frac{1}{\mathrm{P}}\frac{d^2\mathrm{P}}{ds^2} + \frac{1}{\Phi}\frac{d^2\Phi}{d\phi^2} + s^2k^2 = 0.$$

As the azimuthal function Φ(ϕ) must satisfy 2π-periodicity, it can be represented as a Fourier series in exponential form: $\Phi(\phi) = \sum_{n=-\infty}^{\infty}\Phi_n = \sum_{n=-\infty}^{\infty}c_n e^{in\phi}$ for integer n, where c_n is a complex constant. Taking the second derivatives of both sides gives: $\frac{d^2\Phi}{d\phi^2} = -\sum_{n=-\infty}^{\infty}n^2c_n e^{in\phi}$. Therefore, $\frac{d^2\Phi_n}{d\phi^2} = -n^2\Phi_n$ for each n. Substituting this into above wave equation gives the radial equation of each mode n:

$$s^2\frac{d^2\mathrm{P}}{ds^2} + s\frac{d\mathrm{P}}{ds} + (k^2s^2 - n^2)\mathrm{P} = 0.$$

Defining $x = ks$, there are $\frac{d\mathrm{P}}{dx} = \frac{1}{k}\frac{d\mathrm{P}}{ds}$ and $\frac{d^2\mathrm{P}}{dx^2} = \frac{1}{k^2}\frac{d^2\mathrm{P}}{ds^2}$. Replacing ks by x in the above equation gives a second-order linear differential equation, which is the standard Bessel differential equation:

$$x^2\frac{d^2\mathrm{P}}{dx^2} + x\frac{d\mathrm{P}}{dx} + (x^2 - n^2)\mathrm{P} = 0.$$

The solution is a superposition of n-th order Bessel functions [70]. Bessel functions of first kind $J_n(x)$ and second kind $Y_n(x)$ are two linearly independent eigen-solutions of Bessel equation. Bessel functions of third kind are defined as: $H_n^{(1)}(x) = J_n(x) + iY_n(x)$ and $H_n^{(2)}(x) =$

$J_n(x) - iY_n(x)$, and named as Hankel function of first kind and of second kind respectively. As $J_n(x), Y_n(x), H_n^{(1)}(x)$ and $H_n^{(2)}(x)$ are mutually linearly independent, the complete solution is the superposition of any two of them. Although all 6 combinations are mutually exchangeable, for simplicity of equation and physical intuitive understanding, the solution of the cylinder scattering problem is expressed by $J_n(x)$ and $H_n^{(1)}(x)$: $J_n(x)$ is the only Bessel function with non-singular value at $x = 0$, thus can solely represent the field at origin; $H_n^{(1)}(x)$ represents outgoing scattered wave under the time-harmonic convention $e^{-i\omega t}$. Therefore, the n-th order s-dependence of any scalar field component f is:

$$\mathrm{P}_n = a_n J_n(ks) + b_n H_n^{(1)}(ks),$$

where a_n and b_n are arbitrary coefficients, which vary among different orders and different scalar field components, and can be confirmed by sufficient boundary conditions. The complete solution of P is a superposition of different orders. Combining the dependances of 4 dimensions s, ϕ, z, t, the general solution of f in cylindrical coordinate is (absorbing coefficient c_n into a_n and b_n):

$$f = \mathrm{P}(s) \cdot \Phi(\phi) \cdot \mathrm{Z}(z) \cdot T(t) = \sum_{n=-\infty}^{\infty} [a_n J_n(ks) + b_n H_n^{(1)}(ks)] e^{in\phi}\, e^{-i\omega t}.$$

The above expression is called the cylindrical harmonics.

A3. Expand the incident field in region β into cylindrical harmonics

For the scattering problem of infinite cylinder, the space can be separated into region α (filled with the cylindrical material) and region β (surrounding vacuum), where the boundary is at the surface $s = r$ (Figure A.1(a)). In this section, I will transform the expression of plane wave incidence into cylindrical harmonics.

The followings are the known conditions. Firstly, the incident wave vector $\overrightarrow{k^i}$ is normal to $\hat{z}$. Secondly, the incident electric field $\overrightarrow{E^i}$ in region β is confined to be in the transverse electric (TE) mode, because no nonreciprocity is observed under transverse magnetic (TM) incidence [17] for the models concerned. In TE mode, $\overrightarrow{E^i}$ is perpendicular to $\overrightarrow{k^i}$. Thirdly, the confinement of E_z^i polarization yields: $E_s^i = E_\phi^i = 0$.

Since the linearity of Maxwell's equations ensures that scattering coefficients (ratios of scattered to incident wave amplitudes) are independent of the incident wave amplitude, E_z^i can be normalized to unity without loss of generality: $E_z^i = e^{i\left(\overrightarrow{k^i}\cdot\vec{s}-\omega t\right)}$, where $\vec{s} = s\cdot\hat{s} = x\cdot\hat{x} + y\cdot\hat{y}$ is the position vector of the field point. Given incident angle θ (Figure A.1(b)), there is $\overrightarrow{k^i} = k^\beta\cdot\cos\theta\cdot\hat{x} + k^\beta\cdot\sin\theta\cdot\hat{y}$, where $k^\beta = \omega\sqrt{\mu_0\varepsilon_0}$ is the wave number in vacuum region β. Then the space dependence of E_z^i component is expressed in cylindrical coordinate as: $e^{i\overrightarrow{k^i}\cdot\vec{s}} = e^{i[k^\beta(\cos\theta)x + k^\beta(\sin\theta)y]} = e^{isk^\beta\cdot\cos(\phi-\theta)}$.

According to the generating function identity of $J_n(x)$: $e^{\frac{1}{2}x\left(\gamma-\frac{1}{\gamma}\right)} = \sum_{n=-\infty}^{\infty} J_n(x)\gamma^n$, if we let $x = k^\beta s$ and $\gamma = e^{i\left(\frac{\pi}{2}+\phi-\theta\right)}$, then E_z^i can be rewritten in the form of cylindrical harmonics: $E_z^i = e^{-i\omega t}e^{isk^\beta\cdot\cos(\phi-\theta)} = e^{-i\omega t}e^{isk^\beta\cdot\sin\left(\frac{\pi}{2}+\phi-\theta\right)} = e^{-i\omega t}\sum_{n=-\infty}^{\infty} J_n\left(k^\beta s\right)e^{in\left(\frac{\pi}{2}+\phi-\theta\right)}$.

According to the equivalence that $\cos(\phi-\theta) = \sin\left(\frac{\pi}{2}+\phi-\theta\right) = \sin\left(\frac{\pi}{2}-\phi+\theta\right)$, if we let $\gamma = e^{i\left(\frac{\pi}{2}-\phi+\theta\right)}$ instead, the incident electric field can also be $E_z^i = e^{-i\omega t}\sum_{n=-\infty}^{\infty} J_n\left(k^\beta s\right)\cdot e^{in\left(\frac{\pi}{2}-\phi+\theta\right)}$. This equivalence of two angular dependences is also in accordance to the parity symmetry with respect to $\overrightarrow{k^i}$, where ϕ can be replaced by 2θ-ϕ (Figure A.1(b)). In this thesis, I follow the first definition of ϕ-dependence:

$$E_z^i = e^{-i\omega t}\sum_{n=-\infty}^{\infty} J_n\left(k^\beta s\right)e^{in\left(\frac{\pi}{2}+\phi-\theta\right)}.$$

A4. Expand fields in region β into cylindrical harmonics

According to Section A2, the z-component of the total electric field in region β – E_z^β – is the sum of incident field E_z^i and scattered wave E_z^s – and can be expressed in cylindrical harmonics as: $E_z^\beta = e^{-i\omega t}\sum_{n=-\infty}^{\infty}\left[a_{zn}^\beta J_n\left(k^\beta s\right) + b_{zn}^\beta H_n^{(1)}\left(k^\beta s\right)\right]e^{in\phi}$, where J_n terms represent the normalized incident wave and $H_n^{(1)}$ terms represent the scattered wave. To be consistent with the equation of E_z^i at the end of Section A3, constant $e^{in\left(\frac{\pi}{2}-\theta\right)}$ is separated from coefficients a_{zn}^β and b_{zn}^β: $a_{zn}^\beta = e^{in\left(\frac{\pi}{2}-\theta\right)}$ so correspondingly $b_{zn}^\beta = b_n\cdot e^{in\left(\frac{\pi}{2}-\theta\right)}$,

which yields $E_z^\beta = e^{-i\omega t}\sum_{n=-\infty}^{\infty}\left[J_n(k^\beta s) + b_n H_n^{(1)}(k^\beta s)\right]e^{in(\frac{\pi}{2}+\phi-\theta)}$, where b_n is the ratio of scattered amplitude to incident amplitude.

As mentioned above, the TE incidence with E_z polarization has $E_s^i = E_\phi^i = 0$. Next, we need to find out other scalar components of electric and magnetic fields in region β. In 2D field, the two eigen-solutions of vector wave equation in both region α and β are TE mode and TM mode, which are mutually independent under normal-to-axis incidence [56]. Therefore, no E_ϕ and B_z components will be generated in the scattered wave and internal field in cylinder in TE mode. $E_\phi = 0$ and $B_z = 0$ for all waves, where $B_z = 0$ can also be obtained by Faraday's law which will be discussed later. This can also be proven by the first uniqueness theorem [69] of electric field, given TE mode, $E_s^i = E_\phi^i = 0$ at the boundary between region α and β, and plane wave at far-field: We could firstly assume $E_\phi = 0$ and $B_z = 0$, if the field components satisfy all Maxwell's equations and boundary conditions, this solution of components is correct and is the only solution. Thus, the scattering problem reduces to a 2D problem [56, 64] independent of z, and the cylinder boundary reduces to a 2D circle.

So far, E_z^β and E_ϕ^β are confirmed, then E_s^β can be obtained by $\nabla\cdot\overrightarrow{E^\beta} = 0$ in vacuum. Firstly, since $E_s^i = 0$, the E_s^β can be expressed in cylindrical harmonics as $E_s^\beta = E_s^s = e^{-i\omega t}\cdot\sum_{n=-\infty}^{\infty}[b_{sn}^\beta H_n^{(1)}(k^\beta s)]e^{in(\frac{\pi}{2}+\phi-\theta)}$, where b_{sn}^β is the unknown coefficient. Secondly, as system is z-independent and $E_\phi^\beta = 0$, $\nabla\cdot\overrightarrow{E^\beta} = \frac{\partial E_s^\beta}{\partial s} + \frac{1}{s}E_s^\beta = 0$. With the derivative formula $H_n^{(1)\prime}(x) = \frac{H_{n-1}^{(1)}(x) - H_{n+1}^{(1)}(x)}{2}$, $\frac{\partial E_s^\beta}{\partial s} + \frac{1}{s}E_s^\beta = 0$ gives $\sum_{n=-\infty}^{\infty} b_{sn}^\beta[\frac{k^\beta}{2}H_{n-1}^{(1)}(k^\beta s) - \frac{k^\beta}{2}H_{n+1}^{(1)}(k^\beta s) + \frac{1}{s}H_n^{(1)}(k^\beta s)] = 0$. Since $H_n^{(1)}$ of integer orders are linearly independent, the only possibility is $b_{sn}^\beta = 0$ for all n, so $E_s^\beta = 0$.

The magnetic field in region β can be obtained by Faraday's law:

$$\nabla\times\overrightarrow{E^\beta} = -\frac{\partial\overrightarrow{B^\beta}}{\partial t} = \frac{1}{s}\frac{\partial E_z^\beta}{\partial\phi}\hat{s} - \frac{\partial E_z^\beta}{\partial s}\hat{\phi},$$

from which $B_z^\beta = 0$. So far, all the electric and magnetic field components in vacuum region β are well-defined and summarized in Table A1.

Table A1. Field components in vacuum region β		
$\overrightarrow{E^{\beta}}$		
$E_z^i = e^{-i\omega t}\sum_{n=-\infty}^{\infty} J_n(k^{\beta}s)e^{in\left(\frac{\pi}{2}+\phi-\theta\right)}$	$E_s^i = 0$	$E_{\phi}^i = 0$
$E_z^s = e^{-i\omega t}\sum_{n=-\infty}^{\infty} b_n H_n^{(1)}(k^{\beta}s)e^{in\left(\frac{\pi}{2}+\phi-\theta\right)}$	$E_s^s = 0$	$E_{\phi}^s = 0$
$E_z^{\beta} = E_z^i + E_z^s$	$E_s^{\beta} = E_s^i + E_s^s = 0$	$E_{\phi}^{\beta} = E_{\phi}^i + E_{\phi}^s = 0$
$\overrightarrow{B^{\beta}}$		
$B_z^{\beta} = 0$	$\frac{\partial B_s^{\beta}}{\partial t} = -\frac{1}{s}\frac{\partial E_z^{\beta}}{\partial \phi}$	$\frac{\partial B_{\phi}^{\beta}}{\partial t} = \frac{\partial E_z^{\beta}}{\partial s}$

We can further check if $\overrightarrow{E^{\beta}}$ and $\overrightarrow{B^{\beta}}$ satisfies all Maxwell's equations: For $\overrightarrow{E^{\beta}}$, $\nabla\cdot\overrightarrow{E^{\beta}} = \frac{\partial E_z^{\beta}}{\partial z} = 0$; and $\nabla\times\overrightarrow{E^{\beta}} = -\frac{\partial\overrightarrow{B^{\beta}}}{\partial t}$ is satisfied because $\overrightarrow{B^{\beta}}$ is obtained from this equation. For $\overrightarrow{B^{\beta}}$, its divergence is $\nabla\cdot\overrightarrow{B^{\beta}} = 0$ as a divergence of a curl; and $\nabla\times\overrightarrow{B^{\beta}} = \mu_0\varepsilon_0\frac{\partial\overrightarrow{E^{\beta}}}{\partial t}$ is equivalent to $\nabla^2\overrightarrow{B^{\beta}} = \mu_0\varepsilon_0\frac{\partial^2\overrightarrow{B^{\beta}}}{\partial t^2}$ if the divergence and curl of $\overrightarrow{E^{\beta}}$ satisfy Maxwell's equations. The vectorial Helmholtz equation is satisfied because all components of $\overrightarrow{B^{\beta}}$ are in cylindrical harmonics.

A5. Expand fields in region α into cylindrical harmonics

In this section, I will discuss two conditions where region α is filled with dielectrics or gyromagnets under external magnetic field $\overrightarrow{H_0}$ along $-\hat{z}$. As the dielectric material is homogenous and isotropic, the permittivity and permeability are constants and the fields are trivial. However, the gyromagnetic material is anisotropic under external magnetization, resulting in its anisotropic permeability. Therefore, I will use $\overrightarrow{H^{\alpha}}$ and $\overrightarrow{B^{\alpha}}$ together to represent the induced harmonic magnetic field in gyromagnets for conveniency.

A5.1. For dielectric material

The scalar components of electric field in dielectrics can be deduced from Maxwell's equations following the similar procedure to the derivation in region β in Section A4. There is $E_s^{\alpha} =$

$E_\phi^\alpha = 0$ as mentioned. According to Section A2, Hankel function has infinite value at $s = 0$, so any field component in region α doesn't include Hankel term thus E_z^α can be written as $E_z^\alpha = e^{-i\omega t}\sum_{n=-\infty}^{\infty}[d_n J_n(k^\alpha s)]\cdot e^{in(\frac{\pi}{2}+\phi-\theta)}$ under normalized incident amplitude, where d_n is the unknown amplitude of n-th order internal wave to be confirmed, and $k^\alpha = \omega\sqrt{\mu^\alpha \varepsilon^\alpha}$ is the wave number in region α according to the definition in Section A1. For ideal nonconductive dielectric of negligible magnetic response [56], its permittivity ε^α can be denoted by ε^d and its permeability is $\mu^\alpha = \mu_0$, so its refractive index is $ndi = \sqrt{\frac{\varepsilon^d}{\varepsilon_0}}$ and the wave number in dielectric is $k^\alpha = ndi \cdot k^0$. Similar to the derivation of E_s^β, $\nabla\cdot\overrightarrow{E^\alpha} = 0$ and $E_\phi^\alpha = 0$ yield $E_s^\alpha = 0$.

The magnetic field in region α can also be obtained by Faraday's law:

$$\nabla\times\overrightarrow{E^\alpha} = -\frac{\partial\overrightarrow{B^\alpha}}{\partial t} = \frac{1}{s}\frac{\partial E_z^\alpha}{\partial\phi}\hat{s} - \frac{\partial E_z^\alpha}{\partial s}\hat{\phi}.$$

Similar to fields in region β, $\overrightarrow{E^\alpha}$ and $\overrightarrow{B^\alpha}$ also satisfy all Maxwell's equations.

Table A2. Field components in dielectric region α		
$\overrightarrow{E^\alpha}$		
$E_z^\alpha = e^{-i\omega t}\sum_{n=-\infty}^{\infty}[d_n J_n(k^\alpha s)]\cdot e^{in(\frac{\pi}{2}+\phi-\theta)}$	$E_s^\alpha = 0$	$E_\phi^\alpha = 0$
$\overrightarrow{B^\alpha}$		
$B_z^\alpha = 0$	$\frac{\partial B_s^\alpha}{\partial t} = -\frac{1}{s}\frac{\partial E_z^\alpha}{\partial\phi}$	$\frac{\partial B_\phi^\alpha}{\partial t} = \frac{\partial E_z^\alpha}{\partial s}$

A5.2. For gyromagnetic material

Now assume the medium in region α is gyromagnetic material under an external magnetic field $\overrightarrow{H_0}$ along $-\hat{z}$. Its permeability $\overleftrightarrow{\mu^\alpha}$ is a tensor instead of a scalar: $\overleftrightarrow{\mu^\alpha} = \begin{pmatrix}\mu_a & i\mu_p & 0\\ -i\mu_p & \mu_a & 0\\ 0 & 0 & 1\end{pmatrix}\mu_0$ in (x, y, z) coordinate, where the diagonal element $\mu_a = 1 + \frac{\omega_m\omega_0}{{\omega_0}^2-\omega^2}$, non-diagonal element $\mu_p = \frac{\omega_m\omega}{{\omega_0}^2-\omega^2}$, with $\omega_m = \gamma M_s$ and $\omega_0 = \gamma H_0$, where γ is the gyromagnetic ratio, and M_s is the saturation magnetization [58].

Since $\overleftrightarrow{\mu^\alpha}$ is z-irrelevant, the scattering problem is still 2D under normal-to-axis E_z-polarized TE wave incidence. Following the same procedure in Section A5.1, with the normalized

incident amplitude $E_z^i = e^{-i\omega t} \cdot \sum_{n=-\infty}^{\infty} J_n(k^\beta s) e^{in\left(\frac{\pi}{2}+\phi-\theta\right)}$, the scattered wave and internal wave can be written as $E_z^s = e^{-i\omega t} \sum_{n=-\infty}^{\infty} b_n H_n^{(1)}(k^\beta s) \cdot e^{in\left(\frac{\pi}{2}+\phi-\theta\right)}$ and $E_z^\alpha = e^{-i\omega t} \sum_{n=-\infty}^{\infty} d_n J_n(k^\alpha s) e^{in\left(\frac{\pi}{2}+\phi-\theta\right)}$.

The magnetic field $\overrightarrow{B^\alpha}$ can be obtained by Faraday's law; and the $\vec{H}$ fields in both regions can be obtained by the constitutive relation $\overrightarrow{\vec{B}} = \overrightarrow{\vec{\mu}} \cdot \vec{H}$, with $E_\phi^\beta = 0$ and $E_s^\beta = 0$:

$$\nabla \times \overrightarrow{E^\beta} = -\frac{\partial \overrightarrow{B^\beta}}{\partial t} = \frac{1}{s}\frac{\partial E_z^\beta}{\partial \phi}\hat{s} - \frac{\partial E_z^\beta}{\partial s}\hat{\phi} = -\frac{\partial\left(\mu_0 \cdot \overrightarrow{H^\beta}\right)}{\partial t},$$

$$\nabla \times \overrightarrow{E^\alpha} = -\frac{\partial \overrightarrow{B^\alpha}}{\partial t} = \frac{1}{s}\frac{\partial E_z^\alpha}{\partial \phi}\hat{s} - \frac{\partial E_z^\alpha}{\partial s}\hat{\phi} = -\frac{\partial\left(\overrightarrow{\mu^\alpha} \cdot \overrightarrow{H^\alpha}\right)}{\partial t}.$$

According to Faraday's law, $\overrightarrow{B^\alpha} = \frac{1}{i\omega}\left(\frac{1}{s}\frac{\partial E_z^\alpha}{\partial \phi}\hat{s} - \frac{\partial E_z^\alpha}{\partial s}\hat{\phi}\right)$ in (s, ϕ, z) coordinate, transferring to (x, y, z) coordinate, it becomes $\overrightarrow{B^\alpha} = \frac{1}{i\omega}\begin{pmatrix} \frac{1}{s}\frac{\partial E_z^\alpha}{\partial \phi}\cos\phi + \frac{\partial E_z^\alpha}{\partial s}\sin\phi \\ \frac{1}{s}\frac{\partial E_z^\alpha}{\partial \phi}\sin\phi - \frac{\partial E_z^\alpha}{\partial s}\cos\phi \\ 0 \end{pmatrix}$. Combined with $\overrightarrow{B^\alpha} = \overrightarrow{\mu^\alpha} \cdot \overrightarrow{H^\alpha} = \mu_0 \begin{pmatrix} \mu_a H_x^\alpha + i\mu_p H_y^\alpha \\ -i\mu_p H_x^\alpha + \mu_a H_y^\alpha \\ H_z^\alpha \end{pmatrix}$, H_x^α, H_y^α, and H_z^α can be obtained. Transferring $\overrightarrow{H^\alpha}$ to (s, ϕ, z) coordinate gives $H_\phi^\alpha = \frac{1}{i\omega\mu_0}\frac{\frac{i\partial E_z^\alpha}{s\,\partial\phi}\mu_p - \frac{\partial E_z^\alpha}{\partial s}\mu_a}{{\mu_a}^2 - {\mu_p}^2}$.

Table A3. Field components in gyromagnetic region α

$\overrightarrow{E^\alpha}$		
$E_z^\alpha = e^{-i\omega t}\sum_{n=-\infty}^{\infty} d_n J_n(k^\alpha s) e^{in\left(\frac{\pi}{2}+\phi-\theta\right)}$	$E_s^\alpha = 0$	$E_\phi^\alpha = 0$
$\overrightarrow{H^\alpha}$		
$H_z^\alpha = 0$	H_s^α	$H_\phi^\alpha = \frac{1}{i\omega\mu_0}\frac{\frac{i}{s}\frac{\partial E_z^\alpha}{\partial \phi}\mu_p - \frac{\partial E_z^\alpha}{\partial s}\mu_a}{{\mu_a}^2 - {\mu_p}^2}$

A6. Match boundary conditions to solve Mie scattering coefficients

The confirmation of cylindrical Mie scattering coefficients is by matching boundary values of the electromagnetic field. According to equation (7.64) of [69], at boundaries of linear mediums the fields satisfy:

$$\begin{cases} \vec{E}_{\parallel}^{\alpha} = \vec{E}_{\parallel}^{\beta} \quad (1) & \varepsilon^{\alpha}\vec{E}_{\perp}^{\alpha} - \varepsilon^{\beta}\vec{E}_{\perp}^{\beta} = \sigma_f \ (2) \\ \vec{B}_{\perp}^{\alpha} = \vec{B}_{\perp}^{\beta} \quad (3) & \frac{1}{\mu^{\alpha}}\vec{B}_{\parallel}^{\alpha} - \frac{1}{\mu^{\beta}}\vec{B}_{\parallel}^{\beta} = \vec{K}_f \times \hat{n} \ (4) \end{cases}.$$

The boundary is at cylinder surface $s = r$, therefore, the $\perp$ (normal) direction is along the $\hat{s}$ direction, the $\parallel$ (tangential) direction is in the $\hat{\phi} - \hat{z}$ plane.

A6.1. For dielectric material

For dielectric material, approximately $\mu^{\alpha} = \mu^{\beta} = \mu_0$, and there is no free surface current $\vec{K}_f$ and no free surface charge σ_f. Therefore, boundary conditions at $s = r$ reduce to:

$$\begin{cases} E_{\phi}^{\alpha} = E_{\phi}^{\beta}, E_z^{\alpha} = E_z^{\beta} \quad (1) & \varepsilon^{\alpha}E_s^{\alpha} = \varepsilon^{\beta}E_s^{\beta} \quad (2) \\ B_s^{\alpha} = B_s^{\beta} \quad (3) & B_{\phi}^{\alpha} = B_{\phi}^{\beta}, B_z^{\alpha} = B_z^{\beta} \ (4) \end{cases}.$$

According to Section A5.1, they are equivalent to:

$$\begin{cases} E_{\phi}^{\alpha} = E_{\phi}^{\beta} = 0, E_z^{\alpha} = E_z^{\beta} \quad (1) & \varepsilon^{\alpha}E_s^{\alpha} = \varepsilon^{\beta}E_s^{\beta} = 0 \quad (2) \\ \frac{\partial E_z^{\alpha}}{\partial \phi} = \frac{\partial E_z^{\beta}}{\partial \phi} \quad (3) & \frac{\partial E_z^{\alpha}}{\partial s} = \frac{\partial E_z^{\beta}}{\partial s}, B_z^{\alpha} = B_z^{\beta} = 0 \quad (4) \end{cases}.$$

Boundary conditions (1), (3) and (4) give two equations satisfied by the n-th order fields:

$E_z^{\alpha}(r) = E_z^{\beta}(r)$ and $\frac{\partial E_z^{\alpha}}{\partial \phi}(r) = \frac{\partial E_z^{\beta}}{\partial \phi}(r)$ give: $d_n J_n(k^{\alpha}r) = J_n\left(k^{\beta}r\right) + b_n H_n^{(1)}\left(k^{\beta}r\right)$;

$\frac{\partial E_z^{\alpha}}{\partial s}(r) = \frac{\partial E_z^{\beta}}{\partial s}(r)$ gives: $k^{\alpha} d_n J_n'(k^{\alpha}r) = k^{\beta}\left[J_n'\left(k^{\beta}r\right) + b_n H_n^{(1)\prime}\left(k^{\beta}r\right)\right]$.

Based on above two 1st order equations, two unknown coefficients b_n and d_n can be solved:

$$b_n = \frac{J_n'(k^{\beta}r)\cdot J_n(k^{\alpha}r) - \frac{k^{\alpha}}{k^{\beta}} J_n(k^{\beta}r)\cdot J_n'(k^{\alpha}r)}{\frac{k^{\alpha}}{k^{\beta}} J_n'(k^{\alpha}r)\cdot H_n^{(1)}(k^{\beta}r) - H_n^{(1)\prime}(k^{\beta}r)\cdot J_n(k^{\alpha}r)},$$

$$d_n = \frac{J_n'(k^{\beta}r)\cdot H_n^{(1)}(k^{\beta}r) - J_n(k^{\beta}r)\cdot H_n^{(1)\prime}(k^{\beta}r)}{\frac{k^{\alpha}}{k^{\beta}} J_n'(k^{\alpha}r)\cdot H_n^{(1)}(k^{\beta}r) - J_n(k^{\alpha}r)\cdot H_n^{(1)\prime}(k^{\beta}r)}.$$

For vacuum in region β, $k^{\beta} = k^0$. For dielectric material in region α with radius r_d and refractive index ndi, $k^{\alpha} = ndi \cdot k^0$, and its Mie coefficient reduces to:

$$b_n^d = -\frac{ndi\cdot J_n(k^0 r_d)\cdot J_n'(ndi\cdot k^0 r_d) - J_n'(k^0 r_d)\cdot J_n(ndi\cdot k^0 r_d)}{ndi\cdot J_n'(ndi\cdot k^0 r_d)\cdot H_n^{(1)}(k^0 r_d) - H_n^{(1)\prime}(k^0 r_d)\cdot J_n(ndi\cdot k^0 r_d)}.$$

A6.2. For gyromagnetic material

For gyromagnetic material, similarly there is no free surface current $\vec{K}_f$ and no free surface charge σ_f. So boundary conditions at $s = r$ are reduced to:

$$\begin{cases} E_{\phi}^{\alpha} = E_{\phi}^{\beta} = 0, E_z^{\alpha} = E_z^{\beta} \quad (1) & \varepsilon^{\alpha}E_s^{\alpha} = \varepsilon^{\beta}E_s^{\beta} = 0 \quad (2) \\ B_s^{\alpha} = B_s^{\beta} \quad (3) & H_{\phi}^{\alpha} = H_{\phi}^{\beta}, H_z^{\alpha} = H_z^{\beta} = 0 \quad (4) \end{cases}.$$

Boundary conditions (1), (3) and (4) give two equations satisfied by the n-th order fields:

$E_z^{\alpha}(r) = E_z^{\beta}(r)$ and $B_s^{\alpha}(r) = B_s^{\beta}(r)$ give: $d_n J_n(k^{\alpha} r) = J_n\left(k^{\beta} r\right) + b_n H_n^{(1)}\left(k^{\beta} r\right)$;

$H_{\phi}^{\alpha}(r) = H_{\phi}^{\beta}(r)$ requires $\frac{\frac{\partial E_z^{\alpha}}{\partial s}\mu_a - \frac{i}{s}\frac{\partial E_z^{\alpha}}{\partial \phi}\mu_p}{{\mu_a}^2 - {\mu_p}^2} = \frac{\partial E_z^{\beta}}{\partial s}$ at $s = r$, yielding: $d_n\left[\frac{\mu_a}{{\mu_a}^2 - {\mu_p}^2} k^{\alpha} J_n'(k^{\alpha} r) + \frac{\mu_p}{{\mu_a}^2 - {\mu_p}^2}\frac{n}{r} J_n(k^{\alpha} r)\right] = k^{\beta}\left[J_n'\left(k^{\beta} r\right) + b_n H_n^{(1)\prime}\left(k^{\beta} r\right)\right]$.

Based on above two 1st order equations, b_n and d_n can be solved:

$$b_n = \frac{k^{\beta} J_n'(k^{\beta} r) J_n(k^{\alpha} r) - J_n(k^{\beta} r)\left[\frac{\mu_a}{{\mu_a}^2 - {\mu_p}^2} k^{\alpha} J_n'(k^{\alpha} r) + \frac{\mu_p}{{\mu_a}^2 - {\mu_p}^2}\frac{n}{r} J_n(k^{\alpha} r)\right]}{H_n^{(1)}(k^{\beta} r)\left[\frac{\mu_a}{{\mu_a}^2 - {\mu_p}^2} k^{\alpha} J_n'(k^{\alpha} r) + \frac{\mu_p}{{\mu_a}^2 - {\mu_p}^2}\frac{n}{r} J_n(k^{\alpha} r)\right] - k^{\beta} H_n^{(1)\prime}(k^{\beta} r) J_n(k^{\alpha} r)},$$

$$d_n = \frac{k^{\beta} J_n'(k^{\beta} r) H_n^{(1)}(k^{\beta} r) - k^{\beta} J_n(k^{\beta} r) H_n^{(1)\prime}(k^{\beta} r)}{H_n^{(1)}(k^{\beta} r)\left[\frac{\mu_a}{{\mu_a}^2 - {\mu_p}^2} k^{\alpha} J_n'(k^{\alpha} r) + \frac{\mu_p}{{\mu_a}^2 - {\mu_p}^2}\frac{n}{r} J_n(k^{\alpha} r)\right] - k^{\beta} H_n^{(1)\prime}(k^{\beta} r) J_n(k^{\alpha} r)}.$$

For vacuum in region β, $k^{\beta} = k^0$. For gyromagnetic material with radius r_m in region α, $k^{\alpha} = k^m = \sqrt{\frac{\varepsilon_r({\mu_a}^2 - {\mu_p}^2)}{\mu_a}} k^0$, where $\varepsilon_r = \frac{\varepsilon^{\alpha}}{\varepsilon_0}$ [61, 65]. Its Mie coefficient can be rewritten as:

$$b_n^m = -\frac{J_n(k^0 r_m)\left[\frac{\mu_a}{{\mu_a}^2 - {\mu_p}^2} k^m r_m J_n'(k^m r_m) + \frac{\mu_p}{{\mu_a}^2 - {\mu_p}^2} n J_n(k^m r_m)\right] - k^0 r_m J_n'(k^0 r_m) J_n(k^m r_m)}{H_n^{(1)}(k^0 r_m)\left[\frac{\mu_a}{{\mu_a}^2 - {\mu_p}^2} k^m r_m J_n'(k^m r_m) + \frac{\mu_p}{{\mu_a}^2 - {\mu_p}^2} n J_n(k^m r_m)\right] - k^0 r_m H_n^{(1)\prime}(k^0 r_m) J_n(k^m r_m)}.$$

References:

[1] S. John, "Strong localization of photons in certain disordered dielectric superlattices," *Physical Review Letters,* vol. 58, no. 23, pp. 2486-2489, 06/08/ 1987, doi: 10.1103/PhysRevLett.58.2486.

[2] E. Yablonovitch, "Inhibited Spontaneous Emission in Solid-State Physics and Electronics," *Physical Review Letters,* vol. 58, no. 20, pp. 2059-2062, 05/18/ 1987, doi: 10.1103/PhysRevLett.58.2059.

[3] E. Yablonovitch, "Photonic band-gap structures," *J. Opt. Soc. Am. B,* vol. 10, no. 2, pp. 283-295, 1993/02/01 1993, doi: 10.1364/JOSAB.10.000283.

[4] J. B. Pendry, "Calculating photonic band structure," *Journal of Physics: Condensed Matter,* vol. 8, no. 9, p. 1085, 1996/02/26 1996, doi: 10.1088/0953-8984/8/9/003.

[5] M. V. Rybin, D. S. Filonov, K. B. Samusev, P. A. Belov, Y. S. Kivshar, and M. F. Limonov, "Phase diagram for the transition from photonic crystals to dielectric metamaterials," *Nature Communications,* vol. 6, no. 1, p. 10102, 2015/12/02 2015, doi: 10.1038/ncomms10102.

[6] J. B. Pendry, A. J. Holden, D. J. Robbins, and W. J. Stewart, "Magnetism from conductors and enhanced nonlinear phenomena," *IEEE Transactions on Microwave Theory and Techniques,* vol. 47, no. 11, pp. 2075-2084, 1999, doi: 10.1109/22.798002.

[7] D. R. Smith, D. C. Vier, T. Koschny, and C. M. Soukoulis, "Electromagnetic parameter retrieval from inhomogeneous metamaterials," *Physical Review E,* vol. 71, no. 3, p. 036617, 03/22/ 2005, doi: 10.1103/PhysRevE.71.036617.

[8] J. B. Pendry, A. J. Holden, W. J. Stewart, and I. Youngs, "Extremely Low Frequency Plasmons in Metallic Mesostructures," *Physical Review Letters,* vol. 76, no. 25, pp. 4773-4776, 06/17/ 1996, doi: 10.1103/PhysRevLett.76.4773.

[9] R. A. Shelby, D. R. Smith, and S. Schultz, "Experimental Verification of a Negative Index of Refraction," *Science,* vol. 292, no. 5514, pp. 77-79, 2001, doi: doi:10.1126/science.1058847.

[10] J. B. Pendry, D. Schurig, and D. R. Smith, "Controlling Electromagnetic Fields," *Science,* vol. 312, no. 5781, pp. 1780-1782, 2006, doi: doi:10.1126/science.1125907.

[11] U. Leonhardt, "Optical Conformal Mapping," *Science,* vol. 312, no. 5781, pp. 1777-1780, 2006, doi: doi:10.1126/science.1126493.

[12] W. Tang, J. Chen, and T. J. Cui, "Metamaterial Lenses and Their Applications at Microwave Frequencies," *Advanced Photonics Research,* vol. 2, no. 10, p. 2100001, 2021, doi: https://doi.org/10.1002/adpr.202100001.

[13] N. Yu *et al.*, "Light Propagation with Phase Discontinuities: Generalized Laws of Reflection and Refraction," *Science,* vol. 334, no. 6054, pp. 333-337, 2011, doi: doi:10.1126/science.1210713.

[14] S. Zahra *et al.*, "Electromagnetic Metasurfaces and Reconfigurable Metasurfaces: A Review," (in English), *Frontiers in Physics,* Review vol. Volume 8 - 2020, 2021-January-14 2021, doi: 10.3389/fphy.2020.593411.

[15] S. Sun, Q. He, J. Hao, S. Xiao, and L. Zhou, "Electromagnetic metasurfaces: physics and applications," *Advances in Optics and Photonics,* vol. 11, pp. 380-479, 06/19 2019, doi: 10.1364/AOP.11.000380.

[16] J. W. You *et al.*, "Topological metasurface: from passive toward active and beyond," *Photon. Res.,* vol. 11, no. 3, pp. B65-B102, 2023/03/01 2023, doi: 10.1364/PRJ.471905.

[17] W. C. Wong, W. Wang, W. T. Yau, and K. H. Fung, "Topological theory for perfect metasurface isolators," *Physical Review B,* vol. 101, no. 12, p. 121405, 03/26/ 2020, doi: 10.1103/PhysRevB.101.121405.

[18] Q. Song, M. Odeh, J. Zúñiga-Pérez, B. Kanté, and P. Genevet, "Plasmonic topological metasurface by encircling an exceptional point," *Science,* vol. 373, no. 6559, pp. 1133-1137, 2021, doi: doi:10.1126/science.abj3179.

[19] K. v. Klitzing, G. Dorda, and M. Pepper, "New Method for High-Accuracy Determination of the Fine-Structure Constant Based on Quantized Hall Resistance," *Physical Review Letters,* vol. 45, no. 6, pp. 494-497, 08/11/ 1980, doi: 10.1103/PhysRevLett.45.494.

[20] K. von Klitzing, "The quantized Hall effect," *Reviews of Modern Physics,* vol. 58, no. 3, pp. 519-531, 07/01/ 1986, doi: 10.1103/RevModPhys.58.519.

[21] D. J. Thouless, M. Kohmoto, M. P. Nightingale, and M. den Nijs, "Quantized Hall Conductance in a Two-Dimensional Periodic Potential," *Physical Review Letters,* vol.

49, no. 6, pp. 405-408, 08/09/ 1982, doi: 10.1103/PhysRevLett.49.405.

[22] X.-L. Qi and S.-C. Zhang, "Topological insulators and superconductors," *Reviews of Modern Physics,* vol. 83, no. 4, pp. 1057-1110, 10/14/ 2011, doi: 10.1103/RevModPhys.83.1057.

[23] T. Wu, M. Menarini, Z. Gao, and L. Feng, "Lithography-free reconfigurable integrated photonic processor," *Nature Photonics,* vol. 17, no. 8, pp. 710-716, 2023/08/01 2023, doi: 10.1038/s41566-023-01205-0.

[24] S. Raghu and F. D. M. Haldane, "Analogs of quantum-Hall-effect edge states in photonic crystals," *Physical Review A,* vol. 78, no. 3, p. 033834, 09/23/ 2008, doi: 10.1103/PhysRevA.78.033834.

[25] F. D. M. Haldane and S. Raghu, "Possible Realization of Directional Optical Waveguides in Photonic Crystals with Broken Time-Reversal Symmetry," *Physical Review Letters,* vol. 100, no. 1, p. 013904, 01/10/ 2008, doi: 10.1103/PhysRevLett.100.013904.

[26] Z. Lan, M. L. N. Chen, F. Gao, S. Zhang, and W. E. I. Sha, "A brief review of topological photonics in one, two, and three dimensions," *Reviews in Physics,* vol. 9, p. 100076, 2022/12/01/ 2022, doi: https://doi.org/10.1016/j.revip.2022.100076.

[27] Z. Wang, Y. Chong, J. D. Joannopoulos, and M. Soljačić, "Observation of unidirectional backscattering-immune topological electromagnetic states," *Nature,* vol. 461, no. 7265, pp. 772-775, 2009/10/01 2009, doi: 10.1038/nature08293.

[28] L. Lu, J. D. Joannopoulos, and M. Soljačić, "Topological photonics," *Nature Photonics,* vol. 8, no. 11, pp. 821-829, 2014/11/01 2014, doi: 10.1038/nphoton.2014.248.

[29] Y. Poo, R.-x. Wu, Z. Lin, Y. Yang, and C. T. Chan, "Experimental Realization of Self-Guiding Unidirectional Electromagnetic Edge States," *Physical Review Letters,* vol. 106, no. 9, p. 093903, 03/02/ 2011, doi: 10.1103/PhysRevLett.106.093903.

[30] Y. Long, J. Ren, H.-T. Jiang, Y. Sun, and H. Chen, "Quantum spin Hall effect in metamaterials," *Acta Physica Sinica,* vol. 66, no. 22, pp. 227803-227803, 2017, doi: 10.7498/aps.66.227803.

[31] A. B. Khanikaev and G. Shvets, "Two-dimensional topological photonics," *Nature Photonics,* vol. 11, no. 12, pp. 763-773, 2017/12/01 2017, doi: 10.1038/s41566-017-

0048-5.

[32] S. Yao, F. Song, and Z. Wang, "Non-Hermitian Chern Bands," *Physical Review Letters,* vol. 121, no. 13, p. 136802, 09/24/ 2018, doi: 10.1103/PhysRevLett.121.136802.

[33] H. Wang, X. Zhang, J. Hua, D. Lei, M. Lu, and Y. Chen, "Topological physics of non-Hermitian optics and photonics: a review," *Journal of Optics,* vol. 23, no. 12, p. 123001, 2021/10/25 2021, doi: 10.1088/2040-8986/ac2e15.

[34] S. Yao and Z. Wang, "Edge States and Topological Invariants of Non-Hermitian Systems," *Physical Review Letters,* vol. 121, no. 8, p. 086803, 08/21/ 2018, doi: 10.1103/PhysRevLett.121.086803.

[35] H. Shen, B. Zhen, and L. Fu, "Topological Band Theory for Non-Hermitian Hamiltonians," *Physical Review Letters,* vol. 120, no. 14, p. 146402, 04/06/ 2018, doi: 10.1103/PhysRevLett.120.146402.

[36] K. Ding, C. Fang, and G. Ma, "Non-Hermitian topology and exceptional-point geometries," *Nature Reviews Physics,* vol. 4, no. 12, pp. 745-760, 2022/12/01 2022, doi: 10.1038/s42254-022-00516-5.

[37] R. El-Ganainy, K. G. Makris, M. Khajavikhan, Z. H. Musslimani, S. Rotter, and D. N. Christodoulides, "Non-Hermitian physics and PT symmetry," *Nature Physics,* vol. 14, no. 1, pp. 11-19, 2018/01/01 2018, doi: 10.1038/nphys4323.

[38] J. Doppler *et al.*, "Dynamically encircling an exceptional point for asymmetric mode switching," *Nature,* vol. 537, no. 7618, pp. 76-79, 2016/09/01 2016, doi: 10.1038/nature18605.

[39] Y. Ashida, Z. Gong, and M. Ueda, "Non-Hermitian physics," *Advances in Physics,* vol. 69, no. 3, pp. 249-435, 2020/07/02 2020, doi: 10.1080/00018732.2021.1876991.

[40] H. Nasari, G. G. Pyrialakos, D. N. Christodoulides, and M. Khajavikhan, "Non-Hermitian topological photonics," *Opt. Mater. Express,* vol. 13, no. 4, pp. 870-885, 2023/04/01 2023, doi: 10.1364/OME.483361.

[41] A. Altland and M. R. Zirnbauer, "Nonstandard symmetry classes in mesoscopic normal-superconducting hybrid structures," *Physical Review B,* vol. 55, no. 2, pp. 1142-1161, 01/01/ 1997, doi: 10.1103/PhysRevB.55.1142.

[42] X. Zhang, F. Zangeneh-Nejad, Z.-G. Chen, M.-H. Lu, and J. Christensen, "A second

wave of topological phenomena in photonics and acoustics," *Nature,* vol. 618, no. 7966, pp. 687-697, 2023/06/01 2023, doi: 10.1038/s41586-023-06163-9.

[43] B. Bahari, A. Ndao, F. Vallini, A. El Amili, Y. Fainman, and B. Kanté, "Nonreciprocal lasing in topological cavities of arbitrary geometries," *Science,* vol. 358, no. 6363, pp. 636-640, 2017, doi: doi:10.1126/science.aao4551.

[44] Q. Wang, C.-H. Tu, Y.-N. Li, and H.-T. Wang, "Polarization singularities: Progress, fundamental physics, and prospects," *APL Photonics,* vol. 6, no. 4, 2021, doi: 10.1063/5.0045261.

[45] O. V. Angelsky, I. I. Mokhun, A. Y. Bekshaev, C. Y. Zenkova, and J. Zheng, "Polarization singularities: Topological and dynamical aspects," (in English), *Frontiers in Physics,* Review vol. Volume 11 - 2023, 2023-March-03 2023, doi: 10.3389/fphy.2023.1147788.

[46] Y. Zhang *et al.*, "Observation of Polarization Vortices in Momentum Space," *Physical Review Letters,* vol. 120, no. 18, p. 186103, 05/04/ 2018, doi: 10.1103/PhysRevLett.120.186103.

[47] W. Chen, Y. Chen, and W. Liu, "Singularities and Poincar\'e Indices of Electromagnetic Multipoles," *Physical Review Letters,* vol. 122, no. 15, p. 153907, 04/19/ 2019, doi: 10.1103/PhysRevLett.122.153907.

[48] Z. Sadrieva, K. Frizyuk, M. Petrov, Y. Kivshar, and A. Bogdanov, "Multipolar origin of bound states in the continuum," *Physical Review B,* vol. 100, no. 11, p. 115303, 09/03/ 2019, doi: 10.1103/PhysRevB.100.115303.

[49] B. Zhen, C. W. Hsu, L. Lu, A. D. Stone, and M. Soljačić, "Topological Nature of Optical Bound States in the Continuum," *Physical Review Letters,* vol. 113, no. 25, p. 257401, 12/18/ 2014, doi: 10.1103/PhysRevLett.113.257401.

[50] M. Liu, C. Zhao, Y. Zeng, Y. Chen, C. Zhao, and C.-W. Qiu, "Evolution and Nonreciprocity of Loss-Induced Topological Phase Singularity Pairs," *Physical Review Letters,* vol. 127, no. 26, p. 266101, 12/20/ 2021, doi: 10.1103/PhysRevLett.127.266101.

[51] Y. Kang and A. Z. Genack, "Transmission zeros with topological symmetry in complex systems," *Physical Review B,* vol. 103, no. 10, p. L100201, 03/01/ 2021, doi:

10.1103/PhysRevB.103.L100201.

[52] M. G. Silveirinha, "Topological theory of non-Hermitian photonic systems," *Physical Review B,* vol. 99, no. 12, p. 125155, 03/29/ 2019, doi: 10.1103/PhysRevB.99.125155.

[53] D. M. Pozar, *Microwave Engineering*. Wiley, 1997.

[54] J. Asbóth, L. Oroszlány, and A. Pályi, *A Short Course on Topological Insulators*. 2016.

[55] W. P. Su, J. R. Schrieffer, and A. J. Heeger, "Solitons in Polyacetylene," *Physical Review Letters,* vol. 42, no. 25, pp. 1698-1701, 06/18/ 1979, doi: 10.1103/PhysRevLett.42.1698.

[56] H. C. Hulst and H. C. van de Hulst, *Light Scattering by Small Particles*. Dover Publications, 1981.

[57] C. F. Bohren and D. R. Huffman, "Appendix B: Coated Sphere," in *Absorption and Scattering of Light by Small Particles*, 1998, pp. 483-489.

[58] J. Jin, S. Liu, Z. Lin, and S. T. Chui, "Effective-medium theory for anisotropic magnetic metamaterials," *Physical Review B,* vol. 80, no. 11, p. 115101, 09/01/ 2009, doi: 10.1103/PhysRevB.80.115101.

[59] W. Liu, "Generalized Magnetic Mirrors," *Physical Review Letters,* vol. 119, no. 12, p. 123902, 09/21/ 2017, doi: 10.1103/PhysRevLett.119.123902.

[60] C. Caloz, A. Alù, S. Tretyakov, D. Sounas, K. Achouri, and Z.-L. Deck-Léger, "Electromagnetic Nonreciprocity," *Physical Review Applied,* vol. 10, no. 4, p. 047001, 10/01/ 2018, doi: 10.1103/PhysRevApplied.10.047001.

[61] W. C. Wong, "Theoretical study of Lorentz non-reciprocal cylinder gratings," M.Phil., Department of Applied Physics, Hong Kong Polytechnic University, 2020. [Online]. Available: https://theses.lib.polyu.edu.hk/handle/200/10574

[62] B. Peterson and S. Ström, "T Matrix for Electromagnetic Scattering from an Arbitrary Number of Scatterers and Representations of E(3)," *Physical Review D,* vol. 8, no. 10, pp. 3661-3678, 11/15/ 1973, doi: 10.1103/PhysRevD.8.3661.

[63] W. C. Chew, *Waves and Fields in Inhomogeneous Media*. IEEE Press, 1995.

[64] K. Yasumoto, "Electromagnetic Theory and Applications for Photonic Crystals," 2005, ch. 3.

[65] W. Wang, W. T. Yau, Y. Cui, J. Wang, and K. H. Fung, "Maxwell's demon-like

nonreciprocity by non-Hermitian gyrotropic metasurfaces," *Physical Review Research,* vol. 3, no. 2, p. L022006, 04/19/ 2021, doi: 10.1103/PhysRevResearch.3.L022006.

[66] L. C. Botten, N.-A. P. Nicorovici, A. A. Asatryan, R. C. McPhedran, C. M. de Sterke, and P. A. Robinson, "Formulation for electromagnetic scattering and propagation through grating stacks of metallic and dielectric cylinders for photonic crystal calculations. Part I. Method," *J. Opt. Soc. Am. A,* vol. 17, no. 12, pp. 2165-2176, 2000/12/01 2000, doi: 10.1364/JOSAA.17.002165.

[67] M. S. Rudner, N. H. Lindner, E. Berg, and M. Levin, "Anomalous Edge States and the Bulk-Edge Correspondence for Periodically Driven Two-Dimensional Systems," *Physical Review X,* vol. 3, no. 3, p. 031005, 07/23/ 2013, doi: 10.1103/PhysRevX.3.031005.

[68] Y. Guo, M. Xiao, and S. Fan, "Topologically Protected Complete Polarization Conversion," *Physical Review Letters,* vol. 119, no. 16, p. 167401, 10/18/ 2017, doi: 10.1103/PhysRevLett.119.167401.

[69] D. J. Griffiths, *Introduction to electrodynamics*. Fourth edition. Boston : Pearson, [2013] ©2013, 2013.

[70] J. D. Jackson, *Classical electrodynamics*. Third edition. New York : Wiley, [1999] ©1999, 1999.